MODELING AND OPTIMIZATION OF A THERMOSIPHON FOR PASSIVE THERMAL MANAGEMENT SYSTEMS

A Thesis
Presented to
The Academic Faculty

by

Benjamin Haile Loeffler

In Partial Fulfillment
of the Requirements for the Degree
Master of Science in the
G. W. Woodruff School of Mechanical Engineering

Georgia Institute of Technology
December 2012

MODELING AND OPTIMIZATION OF A THERMOSIPHON FOR PASSIVE THERMAL MANAGEMENT SYSTEMS

Approved by:

Dr. J. Rhett Mayor, Advisor G. W. Woodruff School of Mechanical Engineering *Georgia Institute of Technology*	Dr. Sheldon Jeter G. W. Woodruff School of Mechanical Engineering *Georgia Institute of Technology*
Dr. Srinivas Garimella G. W. Woodruff School of Mechanical Engineering *Georgia Institute of Technology*	Date Approved: 11/12/2012

ACKNOWLEDGEMENTS

I would like to first thank my committee members, Dr. Jeter and Dr. Garimella, for their time and consideration in evaluating this work. Their edits and feedback are much appreciated.

I would also like to acknowledge my lab mates for the free exchange and discussion of ideas that has challenged all of us to solve problems in new and better ways. In particular, I am grateful to Sam Glauber, Chad Bednar, and David Judah for their hard work on the pragmatic tasks essential to this project.

Andrew Semidey has been a patient and insightful mentor since my final terms as an undergrad. I thank him for his tutelage and advice over the years. Without him I would have remained a mediocre heat transfer student at best. Andrew was truly indispensable to my graduate education.

I must also thank Dr. Mayor for his guidance, insight, and enthusiasm over the course of this work. He has been rigorous in his teaching and steadfast in holding us to high standards. I am grateful for the engineering student he has helped me become.

I thank Steven Sheffield for his expert machining and instruction. Georgia Tech is lucky to have him. I also thank Craig Wooden for his welding work and instruction.

This project was funded by ARPA-E Agile Delivery of Electrical Power Technology (ADEPT) program, managed by Rajeev Ram.

I also thank Hussam Al-Amin at Midel® for arranging a generous donation of their Midel® 7131 synthetic ester heat transfer fluid for our full scale testing.

TABLE OF CONTENTS

LIST OF TABLES

LIST OF FIGURES

SUMMARY

An optimally designed thermosiphon for power electronics cooling is developed. There exists a need for augmented grid assets to facilitate power routing and decrease line losses. Power converter augmented transformers (PCATs) are critically limited thermally. Conventional active cooling system pumps and fans will not meet the 30 year life and 99.9% reliability required for grid scale implementation. This approach seeks to develop a single-phase closed-loop thermosiphon to remove heat from power electronics at fluxes on the order of 10 - 15 W/cm2. The passive thermosiphon is inherently a coupled thermal-fluid system. A parametric model and multi-physics design optimization code was constructed to simulate thermosiphon steady state performance. The model utilized heat transfer and fluid dynamic correlations from literature. A particle swarm optimization technique was implemented for its performance with discrete domain problems. Several thermosiphons were constructed, instrumented, and tested to verify the model and reach an optimal design.

CHAPTER 1

INTRODUCTION

1.1 Smart and controllable grid

Lack of power flow controllability is a significant concern with the current electrical grid. Total U.S. transmission losses totaled 261,660 million kW-hrs in 2010, or 6.3% of total generation [1]. These losses total over $15 billion at the 2012 U.S. average industrial electricity rate of 0.06 $/kW-hr [2]. Power routing facilitates efficient use of transmission infrastructure to minimize line losses while also providing the capability to isolate faults and minimize service disruptions [3]. As renewable energy sources increase the variability of supply, asymmetric stresses on grid assets will decrease the overall reliability of the grid [4]. The most abundant areas renewable energy in the United States are not co-located with the major regions of electricity usage, as shown in Figure 1.1. In addition to new transmission capacity, the grid must be able to adapt to new and highly variable power sources. Power flow routing facilitates even distribution of loadings on the grid, reducing acute stresses and increasing the grid's reliability. Additionally, power flow routing enables confirmable delivery of electrons from sustainable sources to specific customers [5]. While many options exist for new infrastructure designs, a more cost attractive option is one that allows further utilization of existing infrastructure investments [6]. A "smart and controllable" grid allowing reliable and efficient use of variable and renewable sources may be achieved by augmenting existing grid level transformers with high power solid state electronic convertors [7].

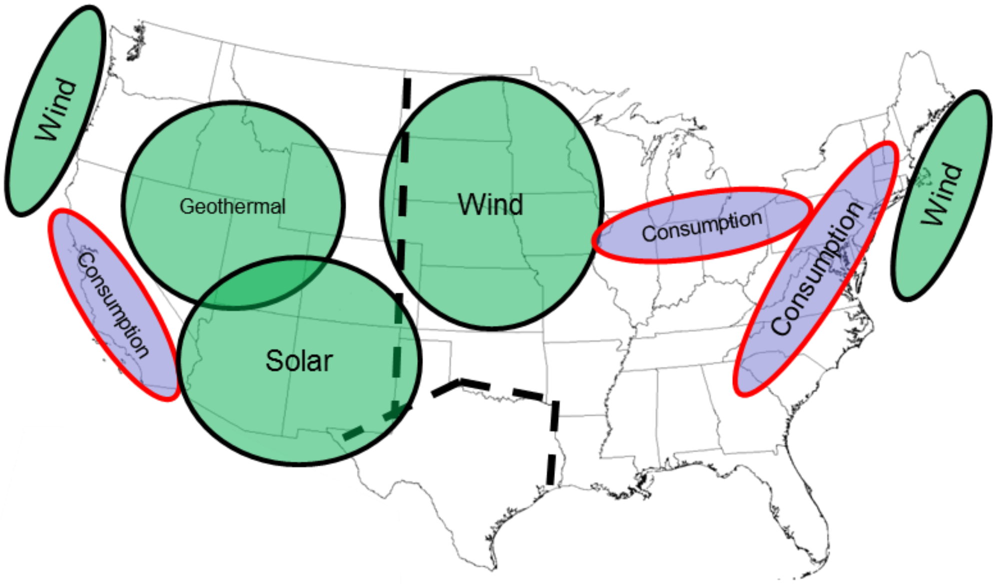

Figure 1.1 Renewable energy sources and electricity consumption regions

1.2 Power electronics for power routing

Application of solid state converters at the grid level is ultimately thermally limited. As the electrical engineering community continues to develop solid state power convertor technologies, improved thermal management may have more potential for increasing power density than the conventional electrical approach of improving device efficiency [8]. This means that larger gains may be realized by pushing existing devices harder in the presence of improved thermal management than by incremental improvements in device efficiency and loss levels.

Existing grid level power routing systems, such as Flexible Alternating Current Transmission Systems (FACTS) are large, expensive, and fail to meet grid level reliability targets [9].

Figure 1.2 Flexible alternating current transmission system (FACTS) installation in Kentucky

An effort is underway to utilize silicon carbide based direct AC/AC converter cells to augment existing power transformers to accomplish dynamic control of grid assets, depicted in Figure 1.3. These Power Convertor Augmented Transformers (PCAT) [10] will require robust thermal management to ensure the augmenting power electronics operate at grid level reliability standards. Thermal losses for these solid state devices are expected to be approximately 105 watts per device, resulting in heat fluxes on the order of 10-15 W/cm^2. These silicon carbide devices are rated for maximum internal junction temperatures of 150°C [11]. Modular cells, consisting of four devices each, are stacked in series and parallel to achieve required voltage and current capacities. A solid model of a four device module and required electrical components is illustrated with cut away section in Figure 1.4

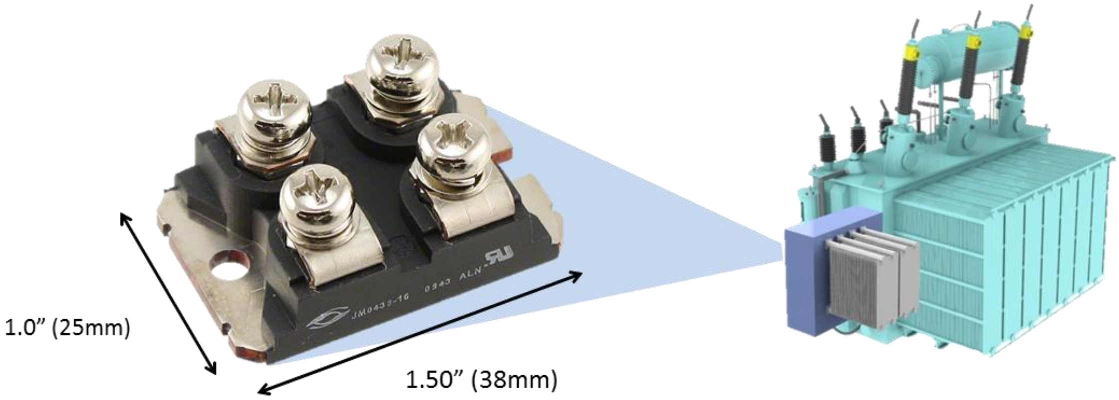

Figure 1.3 GeneSiC IGBT/SiC Diode Co-pack [11] for PCAT (right)

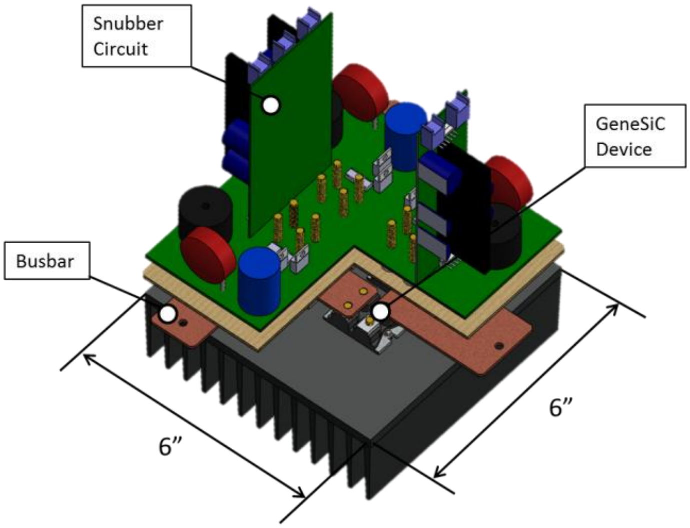

Figure 1.4 Solid model of 4x4 IDCL array and circuitry

The expected total loss from the full 12 module power converter is nominally 5000 W. The system must operate in ambient conditions up to 40 °C. The results of a 1-D thermal analysis of the selected convertor device are compiled in Table 1.1 to determine the minimum thermal management requirements. Individual diode and IGBT junction losses are not reported by the manufacturer. Conservatively assuming that all losses occur in the diode provides a maximum allowable device mounting temperature of 100 °C.

Table 1.1 Device Operation Limitations at Maximum Loss

Metrics	**Units**	**GeneSiC**	
Maximum Total Loss	[W]	5000	
# Devices	[#]	48	
Loss per Device	[W]	105	
Device Footprint	[cm^2]	8	
Max Baseplate Flux	[W/cm^2]	13	
Critical Components		**Diode**	**IGBT**
Limiting $T_{junction}$	[°C]	150	150
Max Loss/junction	[W]	105	105
$R_{juction\text{-}baseplate}$ [11]	[°C/W]	0.475	0.235
$T_{baseplate}$	[°C]	100.1	125.3

It is convention to report a thermal management system's performance in terms of total system thermal resistance. This work will reference the total thermal management system thermal resistance as per Equation (1.1). This baseplate thermal resistance refers to the ratio of the temperature gradient, as measured between the device-baseplate interface and ambient, and the thermal load, *Q*.

$$R_{thermal} = \frac{T_{baseplate} - T_{ambient}}{Q} \tag{1.1}$$

This system requires an expected minimum 30 year mean time between failures (MTBF) consistent with grid reliability requirements. Thirty years corresponds to over 265,000 hours of continuous operation. Active cooling systems offer high performance by utilizing either pumps or fans to force the flow of a heat transfer fluid. These pumps or fans would be driven by conventional electric motors. The 265,000 hour life requirement far exceeds electric machine industry longevity standards for both winding insulation and bearings. Winding insulation is typically rated for 20,000 hours [12], though motors may be operated at below rated power to reduce winding temperatures and increase insulation life. L10 bearing life is typically rated at 90,000,000 revolutions [13]. A low speed motor operating at only 60 rpm would hit this life rating after only 25,000 hours (less than 3 years) of continuous operation. Extreme reliability bearings are designed for usage up to 200,000 hours [14], but are prohibitively expensive and fall short of the full 30 year design target. Electric machines are not suited for the reliability requirements of this thermal management application, eliminating the possible use of fan or pump driven forced convection. Consequently, heat must be transferred naturally to ambient air, rather than via an actively cooled heat sink or fin array. The development of suitable grid-scale passive thermal management systems is critical to the implementation of these power electronics for grid level power flow control.

1.3 Passive thermal management

Forced convection cooling has been eliminated as a viable option for high reliability thermal management application and passive thermal management approaches must be explored. The thermal management challenges presented by the Power Convertor Augmented Transformer (PCAT) are unique. The solid state convertor cells under consideration may not be immersed in a heat transfer fluid, necessitating heat extraction via the single mounting plane. These discrete heat sources must have a low resistance path to ambient to move the required thermal load across the available device mounting area and temperature gradient. The thermal management system must have total thermal resistance below 0.012 °C/W to move the anticipated 5 kW thermal load across the maximum allowable gradient of 60 °C between the 100 °C baseplate and 40 °C ambient. The individual silicon carbide devices have 8 cm^2 mounting footprint areas. Heat extraction via the device mounting plane leads to moderate heat fluxes of 13 W/cm^2 at the device footprint. The circuitry required to utilize these devices requires each 4 device module to occupy a 230 cm^2 area as illustrated in Figure 1.4. This footprint can be used to conductively spread the heat and reduce the flux. When the devices are mounted to a thermally conductive mounting plate, heat spreading to the full base dimensions of the cell reduces the flux to approximately 2 W/cm^2. The contact resistance between the devices and this plate, as well as the conduction resistance within the plate must be considered.

The most basic method of passive cooling is through the use of an extended fin array to increase the area available to transfer heat to ambient air. The maximum array baseplate flux that can be accommodated by a naturally cooled fin array across the available 60 °C temperature differential is close to 1 W/cm^2, based on studies of the limits of pin fins in free convection in air [15]. The thermal loading of these devices exceeds the limitations of naturally cooled conductive fin arrays by a factor of two. A different mechanism for coupling the small mounting footprint of the devices to a large ambient rejection area must be developed.

Advanced passive cooling possibilities include solid state options such as magnetic heat pumps and thermoelectric heat pumps to move heat to large ambient rejection areas. More traditional fluid based heat transport methods are generally classified as either single-phase or two-phase, based on the presence of phase change in the heat transfer fluid. Two-phase options include two-phase thermosiphon loops and heat pipes. Single-phase thermosiphons may operate on buoyancy driven flow alone, or with the addition of ion or magnetic flow pumps. Any of these thermal management methods must ultimately have similar ambient rejection areas, as the heat must be transferred to ambient air through natural convection and radiation alone. Fins alone are not capable of the anticipated flux and temperature requirements as conductive spreading cannot reach the required ambient rejection areas. The passive thermal management challenge requires a method of moving heat from the small, discrete heat sources to suitably large ambient rejection areas. The power electronic requirements in Table 1.1 require the thermal management system have a thermal resistance of less than 0.012 °C/W to maintain acceptable device temperatures at the anticipated thermal load and ambient temperature.

Magnetic cooling via the magnetocaloric effect has been actively researched since the 1970s, but has not reached commercial maturity and remains in R&D due to high material costs and complexity [16]. Thermoelectric heat pumps operating on the Peltier effect offer the possibility of passive thermal management, but do not offer any inherent area multiplication. Thermoelectric devices could possibly be employed to move heat from the devices to an elevated temperature fin array. The fin array temperature must be sufficiently high to reject the 5 kW thermal load to ambient. The minimum temperature gradient from fin array to ambient required for the anticipated thermal load and mounting area can be calculated using correlations for plate fin efficiency and convection coefficients between parallel plates [17]. Extruded aluminum fin arrays are conventionally limited to fin height to fin thickness aspect ratios of less than 6. The minimum baseplate temperature required to move the anticipated flux from an optimal naturally cooled fin array to 40°C ambient is plotted in Figure 1.5 as a function of fin aspect ratio.

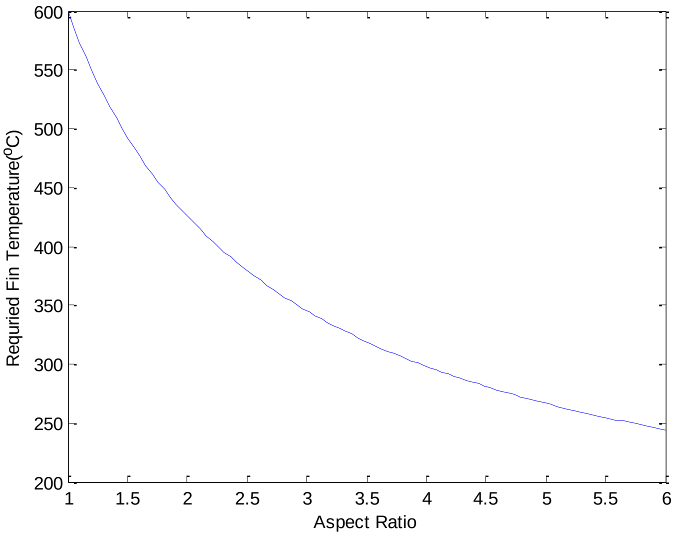

Figure 1.5 Temperature required for cooling devices with and optimal naturally cooled fin array

This analysis shows that thermal management could be accomplished by using a thermoelectric device to move heat from a 100 °C device mounting plate to a 250 °C naturally cooled fin array. Commercial development of thermoelectric devices has been focused on applications for cooling of small areas of high heat flux [18] or for waste heat recovery [19]. Commercially available Bi_2Te_3 thermoelectric devices are typically rated at hot side temperatures well below 250 °C [20]. Furthermore, the coefficient of performance for commercially available thermoelectric heat pumps are below 1 [21], meaning the thermal management system would draw more power than the thermal losses in the power electronics. Thermoelectric heat pumps do not offer an attractive method of thermal management for this application in their current commercial form.

Heat pipes have been widely adopted as thermal management solutions in electronics cooling, including high outputs LED diodes, radar power electronics, and CPU cooling in computers. These systems operate by boiling a heat transfer fluid at the heat source, and allowing the vapor to travel to a heat sink where the fluid condenses. The condensed fluid returns to the heat source either via gravity or capillary action. Combined with forced air cooling of the condenser side, these systems are capable of high heat fluxes. Two phase systems induce longevity concerns do to their pressurized operation and capillary material degradation [22, 23] and are unnecessary at the anticipated 2 W/cm^2 flux. When natural convection is limiting condenser performance, heat pipes and two-phase thermosiphons do not offer any advantages in cost, manufacturability, or size. The anticipated fluxes, temperatures, and reliability requirements indicate that a two phase thermal management system is both unnecessary and undesirable.

Single phase thermosiphons have received minimal attention in recent years. While simple compared to more exotic heat transfer technologies, single phase thermosiphons offer many advantages in cost and complexity. In 1973 Japikse identified closed-loop thermosiphons for cooling systems where noise or reliability is of primary concern and relates their use in applications with fluxes on the order of 2W/cm^2 [24]. The single phase thermosiphon’s lack of moving parts and exotic materials offers an elegant and robust solution to the thermal management requirements. An initial literature study revealed that the anticipated flux level from the PCAT power electronics can be accommodated with single phase transport using commercial engineered heat transfer fluids and area enhancement at the device-fluid interface [24]. For these reasons a single-phase closed-loop thermosiphon was chosen as the best method to address the thermal management of the PCAT power electronics.

1.4 Single phase closed loop thermosiphon

Single-phase closed-loop thermosiphons have been utilized in applications as diverse as nuclear reactor cooling, internal transformer cooling, electric and gas-fired heaters with various hot and cold side orientations, and oil-filled radiators [24]. These thermosiphons operate on the natural circulation of a fluid due to the temperature dependence of its density. The fluid loop is oriented vertically with respect to gravity. The fluid is heated on one side, reducing its density, and is cooled on the opposing side, increasing its density. The fluid rises as its density decreases through the heated section and then sinks as its density increases through the cooled section, resulting in a constant circulation of fluid. This operation is shown schematically in Figure 1.6.

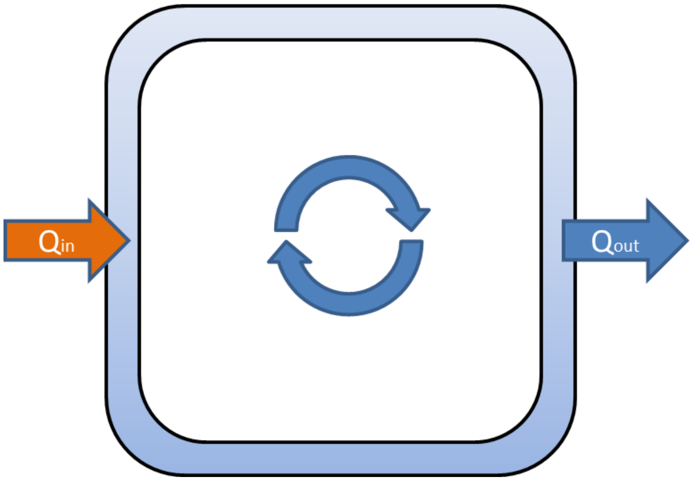

Figure 1.6 Schematic of single phase closed loop thermosiphon operation

Passive thermal management utilizing single phase thermosiphon behavior is commonplace in the existing electrical grid. Traditional transformer windings are cooled via convection to surrounding oil in oil-filled transformer tanks. Natural convection within the tank carries heat to the walls of the tank, which have sufficient area to dissipate the required thermal load to ambient. General transformer cooling and design is routine practice in industry, and standards have been developed for transformer loading and life ratings [25]. Some transformers tanks include extended surfaces to increase heat transfer area. Others incorporate arrays of oil filled plates extending out from the cabinet as illustrated in Figure 1.7. These plates facilitate circulation of oil internally allowing thermosiphon operation.

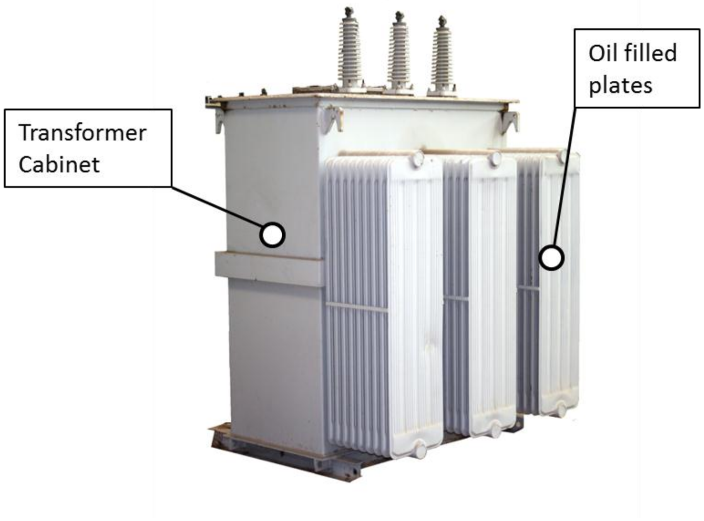

Figure 1.7 Thermosiphon cooling of transformer cabinet [26]

These plate arrays are offered in a variety of sizes by manufacturers who specialize in their production. They are not custom designed to specific applications, but rather selected from standard offerings by transformer manufacturers based on thermal load ratings.

A unique thermosiphon design is developed which is specifically suited for cooling the device mounting baseplate. The design incorporates vertical heat transfer sections connected via upper and lower manifolds. Thermosiphon operation is shown schematically in Figure 1.8. The devices heat the fluid in the vertical hot side channels and density changes in the fluid cause an upward buoyant flow. The upper manifold carries the fluid to the internal cold side channels of the ambient rejection plate array. As heat transfers to ambient, the fluid density increases, resulting in a downward fluid flow.

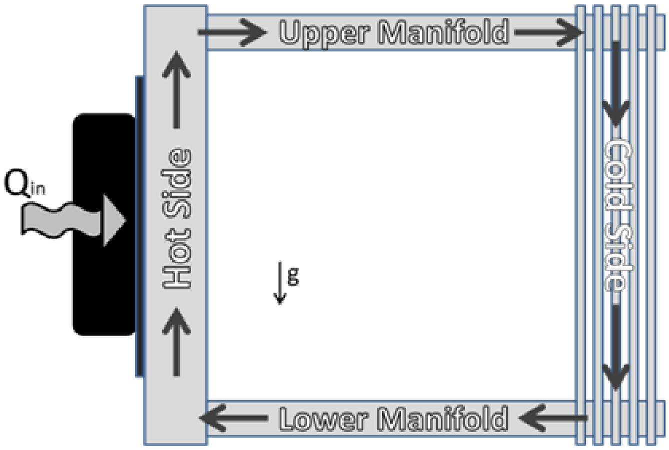

Figure 1.8 Schematic of closed-loop thermosiphon operation (side view)

The basic thermosiphon design is modified to address the specific needs of the power electronics. The area behind the devices is finned to create internal flow channels to minimize the thermal resistance between the devices and the heat transfer fluid. This allows for elevated fluid temperatures for a given device temperatures. Sufficient cold side rejection area is achieved by increasing the number of cold side rejection plates. Area enhancement of the cold side plates is not considered as preliminary calculations showed minimal volumetric performance benefits. The hollow plate array provides large surface area per unit volume while minimizing the conduction path from fluid to ambient surfaces. The elevated fluid temperature due to hot side finning increases the available temperature gradient between the cold side rejection area and ambient, reducing the necessary number of cold side plates. These unique features are shown the section view schematic in Figure 1.9.

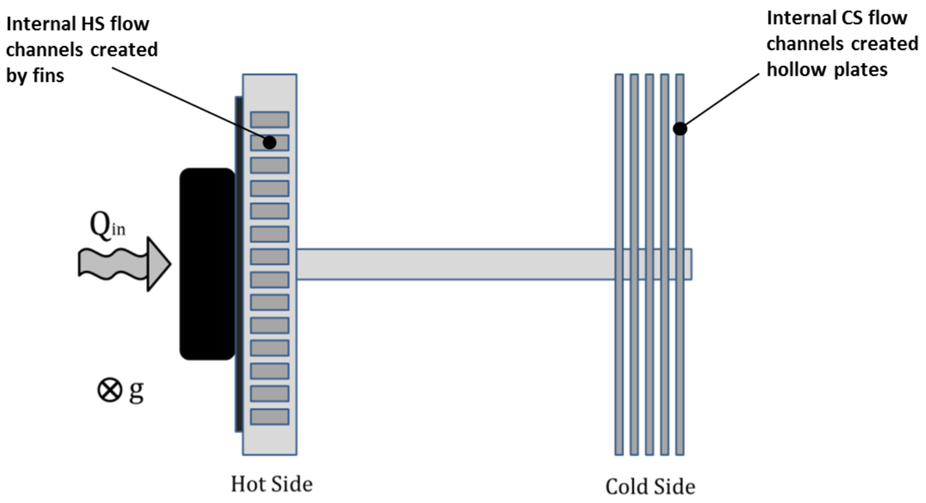

Figure 1.9 Top section view of closed-loop thermosiphon

The power electronics detailed in Section 1.2 are unique, and alternative devices and topologies exist for this and other applications. Passive thermal management will be required for a myriad of designs and applications. The slow and inefficient selection of existing radiator designs based on loading ratings and rule of thumb is not sufficient for this application because the thermal load must be transferred to the fluid through area enhancement features behind the devices. The heat transfer and fluid dynamics of this system are inherently coupled. The flow channels created by the hot side fin array behind the devices will impede the natural circulation of the fluid. Similarly, the thermal resistance of the path from device to fluid limits the maximum allowable fluid temperature. The fluid temperature ultimately dictates the ambient rejection area required to dissipate the heat to ambient air. An optimal combination of geometries exists to minimize the thermal resistance of the single phase closed loop thermosiphon. A rapid design sizing tool used in a variant design methodology would allow rapid sizing of a PTMS for any application. This tool requires a method of quickly evaluating the performance of a set of thermosiphon system geometries.

Finite element CFD analysis has the potential to predict the operation of a given thermosiphon, but the time required to set up and solve a FEA is unacceptable for use in design development. Furthermore, any numerical method that requires a detailed geometric mesh is not suitable for rapid design sizing.

An analytical model of the multi-physics behavior of the closed loop thermosiphon is needed to allow pursuit of an optimal thermosiphon design through numerical optimization. A detailed review of closed loop single phase thermosiphon literature is presented in Chapter 2 and shows that no analytical models exist to predict steady state operation of a thermosiphon with internal channels for area enhancement.

The analytical multi-physics thermosiphon model must identify critical thermosiphon geometries and couple existing fluid dynamic and heat transfer correlations to create a description of the steady state operation of a specific thermosiphon design. The model must be parametric and solve quickly and reliably to be suitable for use in numerical optimization for rapid design sizing. The geometric and thermal characteristics of the power electronics, ambient conditions the system will operate in, system size constraints, allowable cost, and electrical isolation requirements must all be factored into the design of the passive cooling system.

This work will develop a rapid design sizing tool for development of passive thermal management systems for grid level power electronics. The design sizing tool will utilize a multi-physics, single-phase closed-loop thermosiphon model suited to numerical solution. This model will be analytical, parametric, and fast solving. It will account for relevant geometries and conditions and will be used in conjunction with proven numerical optimization techniques to design a PTMS to enable the grid level implementation of the PCAT power electronics for smart grid power routing.

Chapter 2 provides a detailed literature review of thermosiphon research and application. Chapter 3 details the development of the multi-physics thermosiphon model. Chapter 4 presents the implementation of the model in a particle swarm optimization (PSO) to select the critical geometries of the PTMS. Chapter 5 presents the fabrication and testing of the PTMS and compares the results with the model in Chapter 3. A summary of the work, conclusions, contributions, and recommendations for future work is presented in Chapter 6.

CHAPTER 2

REVIEW OF SALIENT LITERATURE

2.1 Introduction

Thermal management is an integral and often limiting aspect of enabling technologies utilizing high power electronics [8]. The thermal management challenges presented by the Power Convertor Augmented Transformer (PCAT) are unique. Chapter 1 details the selection of the single phase thermosiphons based on the anticipated thermal loads and reliability requirements. Their simplicity and lack of moving parts offer cost advantages both upfront and over the life of the system. This work develops a rapid design optimization tool for use in grid-scale passive thermal management system development. This is accomplished by developing a robust parametric analytical model and integrating it into a numerical optimization.

The following sections present literature regarding both fundamental research into thermosiphon operation, and development of models for system performance prediction. Some models have been developed directly from fundamental physics, while others are experimentally derived. Thermosiphon action is induced by differential heating and cooling of a fluid in either a cavity or a closed loop. The closed cavity thermosiphon in horizontal and vertical orientations, and the open thermosiphon, are depicted schematically in Figure 2.1.

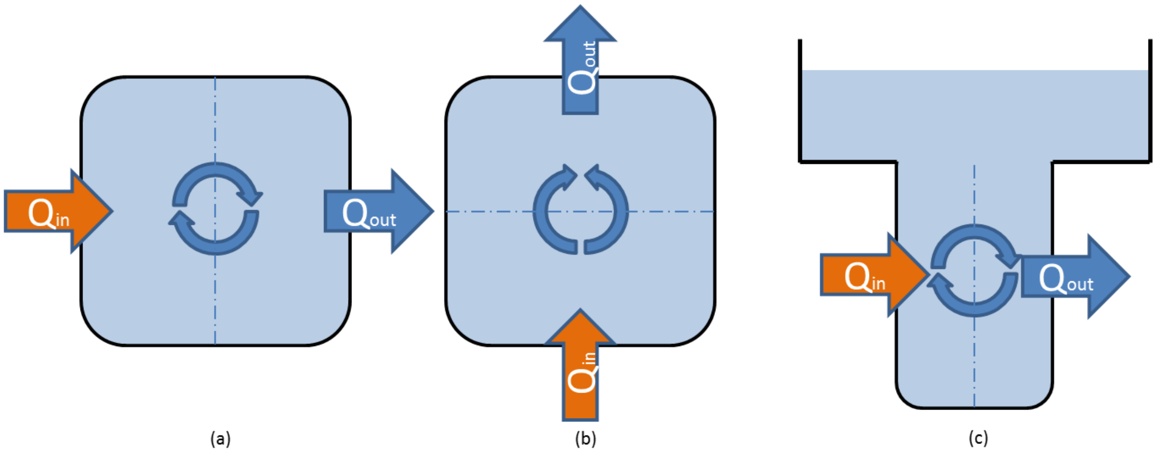

Figure 2.1 Cavity Thermosiphons (a) closed cavity with opposing vertical heat transfer sections, (b) closed cavity with opposing vertical heat transfer sections, and (c) open thermosiphon with opposing vertical heat transfer sections

Cavity based thermosiphons are applicable to very small or very large systems where isolating the heat transfer sections is not feasible. Cavity based systems also require large amounts of heat transfer fluid per unit area of heat transfer surface. The goal of this work is to develop a method for transporting heat from small, discrete heat sources to a large ambient rejection area. A closed loop thermosiphon is better suited to the efficient use of heat transfer fluid and avoids the mixing behavior of the cavity system. The single phase closed loop thermosiphon takes one of two usual forms. The opposing vertical heat source and heat sink arrangement is illustrated in Figure 2.2(a) and Figure 2.2(b) illustrates the horizontal arrangement of heat source below and heat sink above. The vertical arrangement provides for only one possible regime of fluid flow, with fluid rising through the heated section and sinking through the cooled section. The horizontal arrangement results in two equivalent operation regimes, which induces stability concerns that are the focus of extensive research and are presented below.

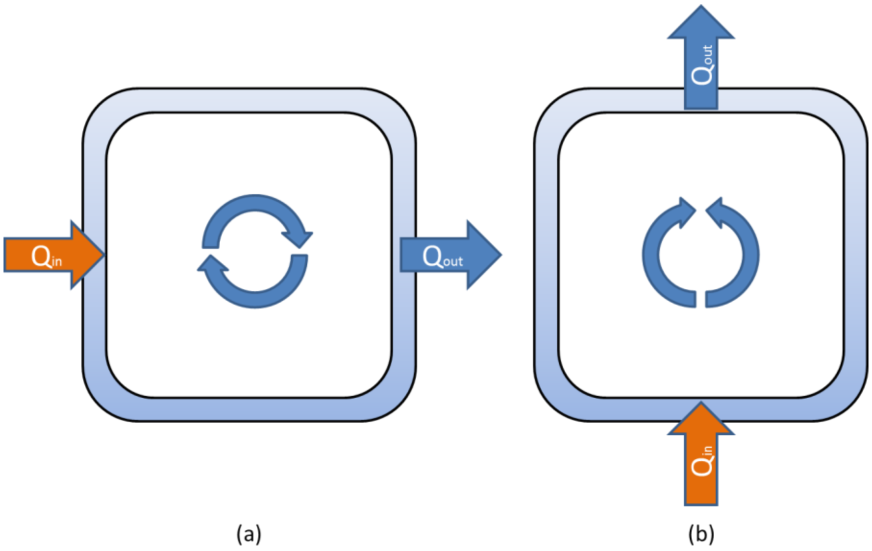

Figure 2.2 Closed Loop Thermosiphon Orientation (a) Vertical Heat Transfer Sections (b) Horizontal Heat Transfer Sections

Applied research into thermosiphons exists largely in two fields. Thermosiphons have been used extensively in electrical transformer cooling and solar water heaters. Representative works in these fields are discussed in the later sections.

2.2 Single phase closed loop thermosiphon

Single phase closed loop thermosiphon research on both the vertical and horizontal orientation is presented. The vertical orientation work has direct application to the present work. A review of research into horizontal orientations is given for perspective and to identify influential methods or assumptions.

2.2.1 Vertical heat transfer sections

Closed loop single phase thermosiphons have been studied extensively. Single phase closed loop thermosiphons have been utilized in applications as diverse as nuclear reactor cooling, internal transformer cooling, permafrost thawing, electric and gas-fired heaters with various hot and cold side orientations, and oil-filled radiators [24].

In 1954 Oak Ridge National Laboratory conducted a fundamental investigation of fluid flow and temperature profiles within a water filled “thermal convection harp”, or thermosiphon. A method for predicting the Reynolds modulus based on wall temperature measurements assuming laminar flow was developed. This work employed the method of integrating the buoyancy pressure potentials and friction terms to arrive at a flow rate and Reynolds number. Utilizing a computer to solve Reynolds and heat transfer equations iteratively, a velocity profile satisfying both was found. An experimental thermosiphon was built to verify the validity of the predicted velocity and temperature profiles. The thermosiphon was constructed of Pyrex tubing in a vertical square with the opposing vertical sections heated and cooled by water jackets. For the uniform cross section and laminar flow, this method predicted Reynolds number to within 30% [27].

In 1958, Kunes measured temperature and velocity profiles in a model thermosiphon for transformer cooling. The work identifies the effect of the vertical position of the heated coil on fluid temperatures and velocities in a single thermosiphon. It was found that positioning the transformer winding lower in the tank induced qualitatively greater oil circulation [28]. While providing experimental insight into thermosiphon behavior, this work provides no analysis for predictive use.

David Japikse completed his Ph.D. thesis [29] and published multiple papers [30-32] in the field of thermosiphon research, including a review of advances in thermosiphon technology in Volume 9 of advances in heat transfer [24]. An evaluation of the closed cavity thermosiphon was published by Japikse et al. in 1970 [30]. The closed cavity system featured heated lower walls and cooled upper walls and was evaluated for potential application to turbine blade cooling. The study included flow observations using dye traces, and extensive spatial temperature measurements to determine experimental Nusselt numbers to describe the heat transfer. Tests were performed at various cavity inclinations and it was found that inclination induced circulatory flows that improved heat-transfer in the thermosiphon.

In 1983 Hart developed a 1-D thermosiphon model for a vertical toroid loop with general heating and wall conditions based on arc length of heated section. The author reduced the previously developed 1st-order non-linear partial differential equations for circulation and energy to three coupled non-linear ordinary differential equations [33]. This analysis was strictly mathematical, with no ability to accommodate changes in cross section or deviation from toroid form, but offered simpler solution with the conversion of PDE to ODE.

In 1991 Bernier and Baliga investigated the flow velocities of a uniform cross section closed-loop thermosiphon with vertical sections as the heat transfer areas. The authors developed a 1D/2D model in that conventional 1D correlations used for the insulated sections of the loop were coupled with 2D cylindrical coordinate models for the heat transfer sections. This method avoided errors that result from assuming average temperature and velocity profiles. An experimental thermosiphon with extended heated and cooled section on opposing vertical legs was constructed. The two vertical lengths were connected via insulated pipe on the same cross section with 180 degree bends at the top and bottom. Experimental flow rates with this thermosiphon were within 5% of the model flow rate predictions [34]. This work provides insight into thermosiphon modeling, but deals only with fluid loops with constant cross section.

Polentini et al. constructed the cooling of an array of discrete heat sources in a rectangular cavity in 1993. The heat sources were in a 3x3 array on a vertical wall while the opposite surface of the cavity contained a heat sink maintained at a lower temperature. Experiments were performed with both water and an engineered dielectric as the heat transfer fluid. It was found that the aspect ratio of the cavity did not affect the heat transfer at the devices. The inclination of the cavity was varied and it was found that moving the heat sources from vertical to lower horizontal orientation resulted in unsteady flow and increased heat transfer [35].

In 2004, Dobson and Ruppersberg investigated single- and two-phase closed loop thermosiphons with vertical heat transfer sections for use in a nuclear reactor cooling system. The analysis utilizes a thermal circuit approach to solving the heat transfer into and out of the loop and determines the flow rate by performing a momentum balance around the loop [36]. The thermal circuit utilized heat transfer coefficients determined experimentally in part II of the paper [37]. These papers detail the development of an analytical thermosiphon model and the design of an experimental thermosiphon. Results of two-phase thermosiphon operation exhibit temperature and flow rate oscillations that are not characterized by the model.

2.2.2 Horizontal heat transfer sections

Several papers relate to the stability and behavior of thermosiphons with horizontal heat transfer sections. The mechanics of the power electronics at hand dictate that the heated portion of the thermosiphon be vertical. The model development and experimental setups of these works are relevant, though stability behaviors are not of concern with the vertical heating and cooling sections to be used in this design.

Welender examined the irregularity of flow in the horizontal closed loop thermosiphon in 1967 [38]. This early model of thermosiphon operation balanced the buoyancy force driving flow with the friction force retarding flow. The model assumes the Boussinesq approximation in dealing with the temperature dependence of the fluid's density. The Boussinesq approximation refers to the consideration of density changes in the fluid due to temperature with respect to gravity, while assuming the fluid otherwise incompressible with regard to inertial effects in the flow [17].

Burroughs et al performed another strictly mathematical analysis of Navier-stokes equations in the Boussinesq approximation to determine theoretical stability behavior of a thermosiphon heated from below [39]. This work establishes assumptions that may be made to evaluate thermosiphon operation, and compares the model results to a far more complex 3D FEM CFD code. The paper reports close agreement between the mathematical model and the finite element analysis.

In 2002, Vijayan described the operation of a rectangular fluid loop with heated bottom section relating the Reynolds number to the Grassof number, a non-dimensional geometric term, and two constants. Experimental work with test thermosiphon allowed for the development of correlations for fully developed laminar and turbulent loops [40].

In 2002 Ishihara et al. published an investigation of a closed rectangular cavity thermosiphon with lower heated section and upper cooled section, as opposed to a loop with heat transfer on opposing lengths. Flow visualizations were compared with finite element predictions. It was found that varying cavity geometry and temperature difference combinations resulted in different convection regimes and stability [41].

In 2003 Maiani et al developed a parametric, analytical model for the stability of a fluid loop with lower heated section, and upper cooled section. This work combined the Boussinesq approximation with the usual fluid and energy balances to describe the operation of the fluid loop [42].

Muscato and Xililia work from 2003 presents both theoretical and experimental results for a rectangular thermosiphon with lower heated section and upper cooling section. The work again focused on capturing stability behavior, but the experimental thermosiphon presentation was also of note. The experimental setup included a flow meter and thermocouples mounted at the inlet and outlet of each of the four flow sections. Thermocouple measurements were used to determine average fluid temperature and heat transfer within each section. The cooling section was created with a constant temperature water jacket and the vertical lengths were insulated. An expansion reservoir accommodated any changes in fluid volume [43].

2.3 High Power Electronic and transformer cooling

Ohmic losses in electronic devices can result in device overheating if thermal transport is not incorporated into the system design. Passive cooling is common in commercial transformers, due to electrical grid reliability requirements. General transformer cooling and design is routine practice in industry, and standards have been developed for transformer loading and life ratings [25]. Numerous resources report methods for modeling the heat transfer within transformers and predicting limiting hot spot temperatures [44-48]. These methods will be presented in detail, along with their applicability to the present work.

Oliver presented a network method for predicting transformer oil flows and temperatures in 1980 [48]. A nodal network is constructed throughout the cooling ducts within and around the windings. Laminar flow is assumed and Nusselt numbers and friction factors, including losses at flow branches, and are predicted using existing correlations. Energy conservation allows derivation of a simultaneous set of linear equations that can be solved numerically. This paper applies the method only to transformer design, though it is applicable to any network of flow paths.

Pierce developed a program to perform transformer loading calculations as an update to the IEEE Loading Guide for Mineral Oil Immersed Transformers [25] in 1994 [45]. This work included updates to the Loading Guide equations for fluid flow, thermodynamics, and heat transfer and incorporated considerations for transient loading, specifically aimed at predicting hot spots during overloads. This work represents an early implementation of analytical modeling of natural circulation fluid cooling and developed more accurate equations and code to predict liquid filled transformer loading capability based on limiting winding and oil temperatures.

Swift et al introduced a thermal circuit equivalent to Pierce's work to simplify the calculation of transformer hot spot and thermal performance. The thermal circuit was constructed consistent with heat transfer thermal circuits with the thermal load as the current, temperature gradient as the voltage, thermal resistance as the dissipative element, and thermal capacitance of the fluid as a storage element [47]. A companion paper presents a comparison of the model performance based on measured top oil temperatures during 24 hour tests on both winter and summer days. Predicted top oil temperature was found to be within 5 °C throughout the testing periods [49]. This work shows the use of a 1-D thermal circuit as a model for a thermal-fluid system.

In *Transformer Design Principles* [44], a thermal model was developed to capture the physical processes within a transformer allowing application to predict thermal operating characteristics of core form power transformers. The approach used a node network analysis of oil pressures, velocities, and temperatures to iteratively solve a non-linear system of governing equations to reach the predicted performance. Using numerical methods, it is possible to develop and solve a system of non-linear equations governing the thermal-fluid system operation.

Work at Siemens in 2004 examined internal convection coefficients based on five different transformer winding cooling duct configurations under both forced and free convection. Conduction resistance of the winding insulation was included in the calculation of maximum winding temperature. Oil entrance cross section to the windings was restricted and heat transfer coefficients were calculated for different levels of flow restriction. The Nusselt number was expressed as a function of Rayleigh number. Experimental scalar and exponential coefficients were experimentally determined [46]. Performance dependence on flow restriction was shown, though all correlations were experimental.

More recent works have sought to use finite element analysis to more accurately predict the magnitude and location of limiting thermal conditions. In 2007 Smolka and Nowak combined CFD and electromagnetic FEM to analyze a 630 kVA dry type transformer. Actual geometries were used to create solid model, which was meshed, and boundary conditions were imposed. Computer simulations were compared with thermocouple measurements and IR thermal imaging. Temperatures predicted by the finite element analysis were within 10 °C of experimental values. The authors conclude that results are satisfactory for detailed spatial temperature predictions and that the method could easily be applied to oil-filled transformers as well [50]. In 2009 Tsili et al. publish their coupling of thermal FEM and CFD tools to analyze the oil circulation within a commercial oil-immersed power transformer [51]. In 2011 Warzoha and Fleisher used CFD software to perform a design sensitivity study of heat pipe geometries for thermal management of a 15 kV/100kVA intelligent universal transformer [52]. The results allow for correlation of system performance to individual geometric parameters. This work provides insight into sensitivity, but is not applicable to selecting an optimal combination of geometries. While these computationally intensive efforts result in detailed spatial prediction of performance, they have little application to rapid design development endeavors due to their high computational overhead and long solution time.

2.4 Solar water heater thermosiphons

Many parts of the world use solar energy for hot water production. These solar water heaters utilize the buoyancy driven flow of a heat transfer fluid to move heat from a collector plate to a heat exchanger. The solar water heater was patented in 1910 by William Bailey [53]. The solar water heater shares many similarities with the proposed thermal management system design. In general, the "hot side" of the solar water heater thermosiphon is an inclined plate with internal channels. The plate is inclined and absorbs radiation to increase solar energy collection. The top of the hot plate is piped to the top of the "cold side", which consists of either a storage tank if the water is heated directly, or a parallel tube heat exchanger immersed in the hot water tank if the water is heated by a secondary working fluid. The working fluid transfers heat to the buildings hot water supply and returns to the base of the hot side via a lower manifold. Norton and Probert compile a review of commercial solar water heater history and the advancement of models to predict their operational performance [54].

A paper by Close in 1962 is one of the earlier works on thermosiphon operation in solar water heaters [55]. He sought to predict the performance of a thermosiphon consisting of a heated absorber located below and adjacent to a reservoir tank. Cold water in the tank would sink to the absorber, be heated, and travel via buoyant flow back to the tank. The insulated tank and manifolds allowed flow rate to be estimated solely based on internal energy of the water and fluid head throughout the loop with reference to the free surface in the tank. All temperature gradients were assumed linear, and flow losses were estimated using established pipe flow correlations. This simple model was applied to two real world solar water heaters and predicted mid-day tank temperatures to within 10 °C. Extension of Close’s model and assumptions could be applied to more complex thermosiphons such as proposed in this work.

In 1974 Ong presented work on a finite-difference method for predicting solar water heater performance [56]. This model was based on the model by Close, but allowed the heat transfer and fluid dynamic correlations to vary with temperature. Solving these temperature dependent equations via a finite difference approach improved the transient analysis of the system. Ong’s model included other improvements particularly in determining plate and fin efficiencies in the collector. The predictions of the improved model were compared to real world solar water heater data. Flow rate was measured by injecting dye at the flow stream at entry to a clear length of tube and measuring the time for it to travel a known length. Prediction trends of fluid temperature and flow rate were qualitatively good compared to the highly variable real world data. This work shows model improvement resulting from consideration of temperature dependent phenomena in thermosiphon operation.

In 1976 Ong published an improved computer program for predicting solar water heater performance. The main improvements to the model involved separating the thermosiphon into sections, allowing the collector, manifolds, and tank to be considered separately. This departed from previous assumptions that the system could be evaluated at an overall mean temperature. An energy balance, heat transfer analysis, and fluid flow analysis was performed for each section. Again, data were heavily influenced by irregularities in cloud cover. The author reported marked improvement in both fluid temperature and velocity predictions over the previous work [57]. This model provides a reliable method for modeling the transient operation of a given thermosiphon, but is hampered by large solution time as evidenced by the author’s choice to limit the time span over which it was applied.

In 1980 Morrison and Ranatunga published their experimental investigation into fluid velocities within the solar water heater thermosiphon. The hot side was heated with an electric resistance heater. A laser anemometer was used to measure fluid velocity in a clear section of the thermosiphon. Velocity measurements indicated laminar flow. Analysis of the data indicated that conventional analysis underestimates the flow rate at Reynolds numbers below 300 and overestimates the flow rate at higher Reynolds numbers. It was determined that the long viscous boundary layer development length in laminar flow required modifications to the friction factor calculation. Furthermore, minor losses which may be deemed negligible in turbulent flow may be significant in laminar regime. This work captures the importance of understanding the flow regime in thermosiphon operation [58].

In 1990 Lin and Lu presented a parametric study of solar water heaters. Using a fixed-node model of a solar water heater, they performed a sensitivity study on the various geometries critical to the design. From these studies, they determine a relative importance of geometries on system performance [59]. It was found that the design of the collector has the largest and most direct impact on the overall system performance. The location of the hot water inlet to the storage tank can significantly impact performance. The overall height of the system has considerably smaller effect on performance, but optimal heights exist and can be pursued.

Applied research into thermosiphon driven solar water heater operation has important relevance to the present work. The methods and assumptions involved in developing the various models serve as examples for this work. The experimental results provide insight into the phenomenon and validation of the approaches. The system requirements of solar water heaters dictate that they take a form different than the one proposed, but the key model elements of energy, pressure, and heat transfer balances hold for any modeling of this genre of thermal management.

2.5 Numerical optimization

2.5.1 Thermosiphon design optimization

Few efforts have been published on the optimization of the geometries of a closed loop thermosiphon. The investigations into thermosiphon operation presented above indicate a strong dependence of overall system performance on particular geometries and fluid properties.

A 2010 paper by Amoiralis et al. uses a previously presented FEM model [51] to compare the performance of rectangular, rounded corners, ellipse, and half-circle shaped transformer fins [60]. This paper makes no mention of rejection area changes, and simply states that the curved surfaces resulted in better simulated performance. The paper confirms that abrupt fluid flow changes are detrimental to thermosiphon performance, but offers no other insights or results.

In 2011 Gastelurrutia et al. developed and verified an algebraic zonal model for the cooling and temperature profile within a traditional oil-immersed distribution transformer. A system of non-linear equations was developed and solved in Excel. Three approaches are possible using this model. The model can be solved for a specific set of geometries by changing temperatures until the system of equations is solved. Secondly, a limiting max oil temperature can be set, and selected geometries added to the variable parameters. The result is geometry and temperature sets that satisfy both the system of equations and the imposed maximum oil temperature. Finally, an optimization can be performed by creating an objective function, fixing the maximum oil temperature, and then changing geometries and solving iteratively until the objective function is minimized. This work simply proposed the optimization study, but does not perform it [61].

2.5.2 Particle swarm optimization (PSO)

Particle swarm optimization has been identified as an optimization method well suited for solving large-scale non-linear optimization problems. Particle swarm optimization concept was introduced in 1995 by Kennedy and Eberhart [62]. This method of optimization uses an iterative approach to identify an optimal solution. Initially, a finite number of parameter sets, known as “particles”, are distributed randomly throughout the user defined solution space. Each particle is solved and evaluated using an objective function. A global best is identified, and the particles each take a finite step in all dimensions of the solution space towards the best particle. The particles are re-evaluated at their new positions, and a new best is identified. This process iterates until the particles converge to an optimal parameter set.

Del Valle et al. demonstrate the use of PSO in selecting control parameters for the vast and complex electrical utility grid [63]. PSO is considered against, and selected as a preferable alternative to, genetic algorithms for solving such complex non-linear optimization problems. The paper goes on to discuss the importance of the optimization parameters such as particle accelerations, velocities, and inertias and solution and convergence criteria. These discussions are used in calibrating the PSO implemented in Chapter 4.

This work will pursue an optimal geometric design in a fashion similar to Semidey and Mayor’s 2011 paper on parametric fin array optimization. [64] The work identified the geometries to be optimized and the upper and lower bounds of their potential values. They then performed a PSO within this solution space. The work focused on the effectiveness of the optimization and the effect of initial particle distribution on convergence. This work serves as an example of the application of PSO to parametric thermal system design.

Semidey et al. 2010 paper applied PSO to a multi-physics design process in which the thermal, electromagnetic, and mechanical design aspects of an electric machine are considered simultaneously [65]. A parametric model of an electric machine was developed and critical geometries were identified. A mesh of the geometries was generated and a finite difference method was used to solve for the spatial temperature distribution. This method allowed for a transient analysis of the system. The completed model was included in a PSO with objective function to select optimal design parameters. The authors found the approach capable of performing an optimization on a multi-disciplinary problem while offering computational advantages over FEA analysis.

2.6 Summary

This review of salient literature finds that while extensive work has been done in both fundamental thermosiphon research and applied thermosiphon development, existing published work does not provide for several requirements of the intended work. First, none of the papers surveyed included provisions for internal area enhancements or the resulting changes in flow cross section. The power electronics arrangement anticipated fluxes will require the use of fins behind the devices, creating parallel rectangular flow paths for the heat transfer fluid. Similarly, the large ambient rejection area required will require multiple parallel flow paths on the thermosiphon cold side. This work will account for multiple parallel flow paths and resolve the transitions necessary to couple the hot and cold sides via manifolds. Secondly, the experimental thermosiphon works almost exclusively utilize chilled water jackets to remove heat from the cold side of the fluid loop. While practical in a laboratory setting, this methodology ignores the necessity of ultimately transferring heat to the ambient environment. Furthermore, the works on applied transformer cooling use accepted textbook values when considering rejection to ambient and make no effort to explore the effect of cold side design on system performance. This work will integrate the geometry-dependent heat transfer behavior of the ambient rejection side of the thermosiphon into the system model. Finally, no works exist detailing the application of particle swarm optimization to advance passive thermal management system design. This work will utilize PSO to create a rapid design sizing tool suitable for grid scale system design.

CHAPTER 3

MULTIPHYSICS THERMOSIPHON MODEL

3.1 Introduction

This work seeks to develop a fast parametric design tool for the development of passive thermal management systems (PTMS) for the cooling of high power electronics. This necessitates development of an analytical model to predict device mounting baseplate temperatures based on critical system geometries, thermal load, and ambient conditions. A multi-physics model couples established heat transfer, fluid dynamic and thermodynamic phenomena and correlations to fully describe the steady state behavior of the system. The aim of this model is to provide a predictive tool for use in a numerical optimization. The coded model may be used as a rapid design sizing and development tool. The model must accurately predict device mounting temperatures for a given set of operating conditions and geometric design parameters. It must solve quickly to be suitable for use in iterative numerical optimization. The model should consider only the critical geometries and material properties to allow adaptability and accommodation of variations in design features.

3.2 General problem statement

The first step in the thermosiphon design tool development is to identify the system geometries relevant to system performance and design optimization. The proposed design utilizes a hot side fin array connected to vertical hollow cold side plates via upper and lower manifolds, shown in Figure 3.1. Buoyant forces drive fluid upward through the hot side (HS) fin array channels, through the upper manifold (UM), down the internal channels of the cold side (CS) plates, and back to the bottom of the hot side via the lower manifold (LM). Thermosiphon fluid flow direction is illustrated schematically with arrows in the figure.

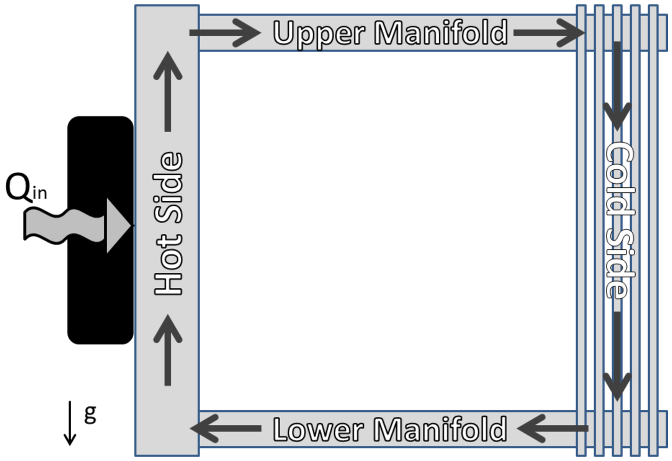

Figure 3.1 Schematic of closed-loop thermosiphon operation

The single-phase closed-loop model must be parametric, such that geometries can be changed individually, and analytical, such that it solves quickly and may be used iteratively in numerical optimization. The geometries critical to the operation and performance of the thermosiphon must be identified and coded as inputs to the model. Appropriate analytical correlations for the fluid dynamic and heat transfer phenomena present in the system must be compiled and coded such that the steady state conditions of the system may be quickly determined numerically. System performance will be evaluated based on the temperature of the device-baseplate interface. The baseplate thermal resistance will also be calculated as an additional measure of performance, as discussed in Chapter 1. This thermal resistance addresses the thermal management system as a whole, in keeping with an electrical engineering community standard, and does not refer to any particular convective or conductive heat path, or thermal resistance, within the system.

3.3 Model assumptions

The closed-loop thermosiphon is divided into four sections, as labeled in Figure 3.1, such that fundamental thermodynamic, fluid dynamic and heat transfer analysis can be applied to the uniform cross section segments independently. Throughout, fluid properties at the four junctions between sections are used to determine average fluid temperatures within each section. Temperature dependent fluid properties are predicted using textbook property tables [17] and these mean fluid temperatures. Mass flow rate is assumed to be constant throughout and mass accumulation zero.

An analytical model is sought in lieu of a finite difference approach to allow a general application without consideration of specific geometry transitions and mesh generation. Fluid density changes are considered for the fluid’s gravitational potential, but the fluid is considered dynamically incompressible as per the Boussinesq approximation. The fluid dynamic description is developed based on the Bernoulli streamline pressure equation. Two dimensional effects as captured by the Navier-Stokes equation are assumed negligible. This assumption also avoids the complications of solving differential equations numerically. A first law thermodynamic energy balance is maintained through each of the four sections. Second law irreversibilities are expected to be small due to low flow rates, incompressible fluid, and small heat transfer layer gradients and are assumed negligible.

3.4 Parametric model geometries

A parametric design tool describing the critical geometries of the thermosiphon was developed. The geometries within each of the four thermosiphon sections which are involved in the applicable heat transfer and fluid dynamic correlations were identified.

All geometries related to heat transfer surfaces are necessary to calculate total area and ultimately thermal resistances. Flow channel dimensions are necessary for calculating hydraulic diameters and Nusselt numbers. The AC/AC convertors are mounted to a spreader plate, as discussed in Chapter 1, which dictates the size of the hot side fin array. The critical geometries of the thermosiphon are illustrated in Figure 3.2 and are labeled with their respective variables. Table 3.1 compiles these critical design variable names along with descriptions.

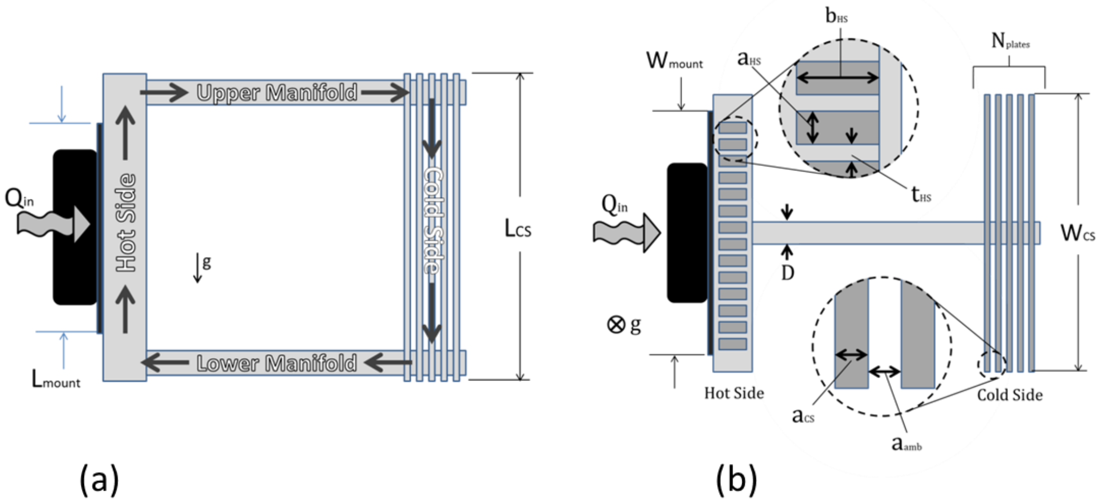

Figure 3.2 Critical geometric parameters (a) side view and (b) top section view

Table 3.1 Critical system geometries

Variable	Description
a_{HS}	Hot Side Channel Width
b_{HS}	Hot Side Channel Depth
t_{HS}	Hit Side Fin Thickness
W_{HS}	Hot Side Finned Area With
L_{HS}	Hot Side Channel Length
W_{mount}	Device Mounting Plate Width
L_{mount}	Device Mounting Plate Length
D	Manifold Diameter
a_{CS}	Cold Side Internal Channel Width
a_{amb}	Cold Side External Channel Width
W_{CS}	Cold Side Plates Width
L_{CS}	Cold Side Plates Length
N_{plates}	Number of Cold Side Plates

Some of the thermosiphon geometries are constrained by practical limits. The overall size of the hot side is dictated by the size, number, and arrangement of devices. The cold side arrays may not be allowed to extend beyond pragmatically imposed limits of width or length. Other considerations, such as material selection for specific components, may be user specified or identified as variables for manipulation.

3.5 Analytic model development

The temperature rise, ΔT, of the fluid across each section is determined via a 1st law energy balance, Equation (3.1) . Here, the specific heat, c_p, is taken at the average fluid temperature in the section and the heat flow is governed by relevant heat transfer equations to be defined below.

$$Q = \dot{m} c_p \Delta T \tag{3.1}$$

For example, the fluid temperature change across the cold side, ΔT_{CS}, is equal to T_4-T_3 and the corresponding heat flow is Q_{CS}, as illustrated in Figure 3.3.

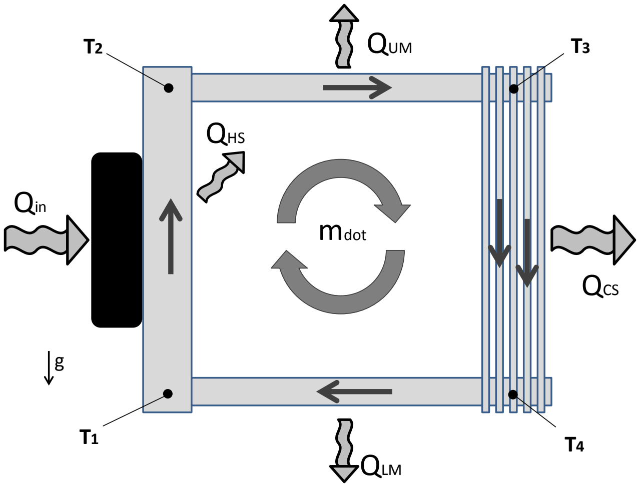

Figure 3.3. Thermosiphon nodal fluid temperatures and sectional heat flows

The heat transfer paths within each section are identified and a 1-D thermal circuit is created, shown in Figure 3.4. The cold side convection resistance represents the convective heat transfer from the fluid in the cold side channels, at temperature $T_{CS,fluid}$, to the inner cold side walls at temperature $T_{CS,inner}$. The cold side conduction term accounts for the temperature gradient resulting from heat conduction from the inner wall to the outer wall of the cold side. Finally, the ambient rejection terms describe the transfer of heat from the outer cold side surface, at $T_{CS,outer}$, to ambient via convection and radiation.

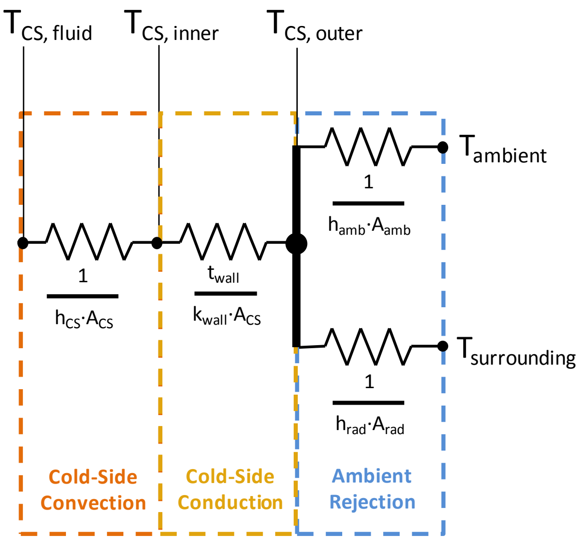

Figure 3.4. Example Cold Side (CS) 1-D Thermal Circuit

A thermal circuit is constructed for each of the four sections of the thermosiphon. For each path, the heat flow is calculated using the total path thermal resistance and temperature differential, Equation (3.2) .

$$Q = \frac{\Delta T}{R_{therm}} \tag{3.2}$$

Individual thermal resistances are calculated per Equation (3.3) for each convection, conduction, or radiation heat transfer path, respectively.

$$R_{conv} = \frac{1}{hA}, \quad R_{cond} = \frac{l}{kA}, \quad R_{rad} = \frac{1}{h_{rad}A_{rad}} \tag{3.3}$$

For each of the three heat rejection sections the total temperature differential, ΔT, is the difference between the average fluid temperature in that section, and the surrounding ambient air temperature. The various thermal resistances are calculated using the relevant application of established heat transfer correlations, presented later. From the temperature differential and total thermal resistance, the heat flow from each section can be predicted.

For convective heat transfer between a fluid and surface, the internal convection coefficient is related to the Nusselt number by Equation (3.4) .

$$h = \frac{kNu}{L^*} \tag{3.4}$$

For laminar flow, the Nusselt number for fully developed flow in circular ducts is 4.36. For the hot and cold side rectangular flow channels, the fully developed Nusselt number is taken from Equation (3.5) , fit to tabular data [17].

$$Nu_{lam,FD} = 0.5989 \ln\left(\frac{b}{a}\right) + 2.6848 \tag{3.5}$$

Many heat transfer fluids have high Prandtl numbers, indicating the entry region preceding fully developed flow may be significant. Accounting for entry region, the average Nusselt number is given by Equation (3.6) .

$$\overline{Nu} = Nu_{lam,FD} + \frac{0.0668\left(\frac{D_H}{L}\right)\mathrm{Re}\,\mathrm{Pr}}{1 + 0.04\left(\left(\frac{D_H}{L}\right)\mathrm{Re}\,\mathrm{Pr}\right)^{2/3}} \tag{3.6}$$

For Reynolds numbers greater than 2300, Nusselt correlations for internal turbulent flows, Equation (3.7) , are used.

$$Nu_{turbulent} = \frac{\left(\left(\frac{f}{8}\right)(\mathrm{Re} - 1000)\mathrm{Pr}\right)}{1 + 12.7\sqrt{\frac{f}{8}}\left(\mathrm{Pr}^{2/3} - 1\right)} \tag{3.7}$$

For the hot side flow channels created by the fin array, standard fin efficiency calculations are performed to account for increased conductive resistance in the path [17].

Heat transfer to ambient is governed by external natural free convection. For the upper and lower manifolds, the heat flows and temperature change in the fluid are expected to be small. Thus, the manifolds are modeled as isothermal horizontal cylinders with average Nusselt numbers given by Equation (3.8) [66].

$$\overline{Nu}_D = \left(0.60 + \frac{0.387 Ra_D^{1/6}}{\left(1 + \left(\frac{0.559}{\Pr} \right)^{9/16} \right)^{8/27}} \right)^2 \tag{3.8}$$

The parallel cold side rejection plates are expected to see significant fluid temperature change. As the heat transfer fluid and ambient air will flow counter to one another, an isoflux condition is assumed. For natural buoyancy driven convection between vertical isoflux parallel plates, the average Nusselt number is predicted by Equation (3.9) [67].

$$\overline{Nu}_S^* = \left(\frac{48}{Ra_S^* \frac{a_{amb}}{L}} + \frac{2.51}{\left(Ra_S^* \frac{a_{amb}}{L} \right)^{2/5}} \right)^{-1/2} \tag{3.9}$$

For radiating surfaces, the effective radiation convection coefficient, calculated using Equation (3.10) , and the effective radiative surface area, accounting for view factors, are used to determine thermal resistance for the radiation path [17]. The total radiating area of the cold plate array is taken to be the envelope area of the cube bounding the total array volume. This neglects the areas that only see adjacent plate surfaces. The internal radiation between adjacent plates is expected to balance the temperature across the parallel paths as heat will radiate from the higher temperature plate to an adjacent lower temperature plate.

$$h_{rad} = \sigma\varepsilon\left(T_s^2 + T_{sur}^2\right)\left(T_s + T_{sur}\right) \tag{3.10}$$

Fluid flow through the thermosiphon loop is driven by the balance of buoyancy pressure potentials due to thermal expansion, across the vertical sections, and pressure drops due to flow losses, throughout. The buoyancy potential across the vertical sections is given by Equation (3.11) .

$$\int_{inlet}^{outlet} \left.\frac{dP}{dx}\right|_{buoy} \cong \Delta P_{buoy} = \beta\rho g L \Delta T \tag{3.11}$$

The pressure losses across a given section are the sum of all major and minor losses incurred.

$$\int_{inlet}^{outlet} \left.\frac{dP}{dx}\right|_{loss} \cong \Delta P_{loss} = \sum \Delta P_{major} + \sum \Delta P_{\min or} \tag{3.12}$$

Pressure losses are determined via established methods [68]. Major losses in the four sections are given by Equation (3.13) .

$$\Delta P_{major} = \frac{C\mu L}{2D_H^2}\frac{\dot{m}}{\rho A} \tag{3.13}$$

Flow loss coefficients are dependent upon the nature of the velocity profile. The model assumes laminar flow below Re =2300 and turbulent above. For laminar flow in circular channels, C =64. For laminar flow in the rectangular channels found in the hot and cold sides, C is calculated using the curve fit to tabular data [68] given in Equation (3.14)

$$C = 11.889\ln\left(\frac{b}{a}\right) + 55.561 \tag{3.14}$$

For turbulent flow, C is determined via the friction factor from Colebrook's equation [68], shown in Equation (3.15) .

$$\frac{1}{\sqrt{f}} = -2\log_{10}\left(\left(\frac{r}{3.7D_H}\right)+\left(\frac{2.51}{\mathrm{Re}\sqrt{f}}\right)\right) \tag{3.15}$$

Minor losses occur whenever the fluid encounters a change if flow area or flow direction, and are calculated using Equation (3.16) . Table values [68] for the loss coefficients, K_{loss}, are specified for each such transition.

$$\Delta P_{\min or} = \frac{K_{loss}\rho}{2}\left(\frac{\dot{m}}{\rho A}\right)^2 \tag{3.16}$$

Integrating the pressure gradient along the fluid flow path must result in a net pressure change of zero as in Equation (3.17) .

$$\oint \frac{dP}{dx} \cong \sum \Delta P = \Delta P_{HS,buoy} + \Delta P_{HS,loss} + \Delta P_{UM,loss} + \Delta P_{CS,buoy} + \Delta P_{CS,loss} + \Delta P_{LM,loss} = 0 \tag{3.17}$$

The above collection of equations is applied, as appropriate, to each of the four thermosiphon sections. Conduction heat transfer between the sections is neglected as short range temperature gradients are expected to be small, and conduction paths long, compared to conduction areas. When combined, these equations provide a full description of the steady state behavior of the closed-loop thermosiphon. To solve the above equations, fluid temperatures and flow rates must be known. Heat flows into and out of the four thermosiphon are required to satisfy the thermodynamics balances. The non-linearity of the equation set requires a numerical approach to finding the steady state solution. The following section identifies the unknowns and establishes the system of equations for solution.

3.6 Inputs to the model

The multi-physics model is coded to accept the design parameters as a vector input. These variables define the basic thermal and mechanical operating requirements of the system, and the fundamental dimensions of the design. The operating conditions are listed in the upper half of Table 3.2. Q_{in} is the total thermal load resulting from losses in the power electronics. L_{mount} and W_{mount} define the outermost dimensions of the device array. T_{amb} and T_{surr} define the ambient temperatures for convection and radiation, respectively.

The critical geometries as identified in Table 3.1must also be inputs to the model. Some of these geometries must be selected from a broad range of potential values. Others, such as the width and length of the cold side plate array (W_{CS}, L_{CS}), can be selected based on real world constraints. The overall hot side finned area (W_{HS}, L_{HS}), can be calculated as a function of the device mounting areas (W_{mount}, L_{mount}). The critical geometries are list in the bottom section of Table 3.2.

Table 3.2. Multi-physics model input parameters

	Variable	Description
Operating Conditions (Problem Definition)	Q_{in}	Thermal Load [W]
	L_{mount}	Device Mounting Length [m]
	W_{mount}	Device Mounting Width [m]
	T_{amb}	Ambient Temperature [°C]
	T_{surr}	Surrounding Temperature [°C]
Geometric Parameters (Design Variables)	a_{HS}	Hot Side Channel Width [m]
	b_{HS}	Hot Side Channel Depth [m]
	t_{HS}	Hot Side Fin Thickness [m]
	a_{CS}	Cold Side Channel Width [m]
	a_{amb}	Plate Spacing [m]
	$D_{manifold}$	Manifold Diameter [m]
	W_{CS}	Cold Side Plates Width [m]
	L_{CS}	Cold Side Plates Length [m]
	N_{HX}	Number Cold Side Plates

3.7 Solution algorithm

The implementation of the multi-physics model begins with the identification of the operating requirements, design variables, and steady state solution variables. For the selected design, the geometric input variables to the model are represented schematically in Figure 3.2 above.

The multi-physics model equations account for the thermodynamic, fluid dynamic and heat transfer behavior of the individual sections. Numerical solution requires a system of equations equal to the number of unknown variables in the model. For a known thermal load, Q_{in}, assessing the thermosiphon as shown in Figure 3.5 reveals eight unknown parameters defining steady state operation.

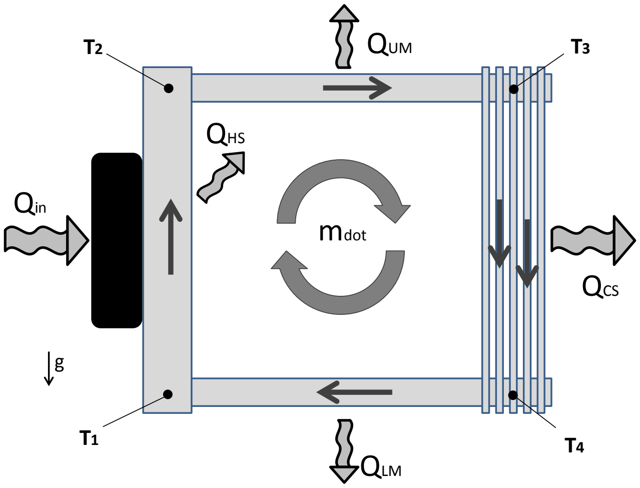

Figure 3.5. Thermosiphon Unknown Operating Parameters

The four temperatures, (T_1, T_2, T_3, T_4), at the junctions between the four sections, the mass flow rate, ($\dot{m}$), of the circulating fluid, and the heat flows, ($Q_{UM}, Q_{LM,}Q_{CS}$), out of the manifolds and cold sides are the unknown quantities governing steady state thermosiphon operation. For these eight unknowns, the model yields eight equations, shown in (3.18) , that must be satisfied for steady state operation.

$$\left\{\begin{array}{c} Q_{in} = \dot{m}c_p\left(T_2 - T_1\right) - Q_{HS,loss} \\ Q_{UM} = \dot{m}c_p\left(T_2 - T_3\right) \\ Q_{CS} = \dot{m}c_p\left(T_3 - T_4\right) \\ Q_{LM} = \dot{m}c_p\left(T_4 - T_1\right) \\ \\ \Delta P_{HS} + \Delta P_{UM} + \Delta P_{CS} + \Delta P_{LM} = 0 \\ \\ Q_{UM} = \dfrac{\left(T_{UM} - T_{amb}\right)}{R_{UM}} \\ Q_{CS} = \dfrac{\left(T_{CS} - T_{amb}\right)}{R_{CS}} \\ Q_{LM} = \dfrac{\left(T_{LM} - T_{amb}\right)}{R_{LM}} \end{array}\right\} \tag{3.18}$$

The first four equations account for the thermodynamic energy balance in each of the four sections. The fifth equation is the pressure continuity for the closed-loop. The final three equations reflect the heat transfer limitations for each section across a given temperature differential and thermal resistance.

The model solves the system of equations using a standard multivariable root finding method and determines the steady state operation of the thermosiphon. A schematic of the numerical system of equations solver is illustrated in Figure 3.6. The particular solver used is Matlab®'s built in *fzero* function. The program is supplied with initial guesses for the eight unknowns, and a function call to the model which returns the remainders of the eight simultaneous equations. The solver manipulates the values of the unknowns until the remainders of the system of equations converge to zero.

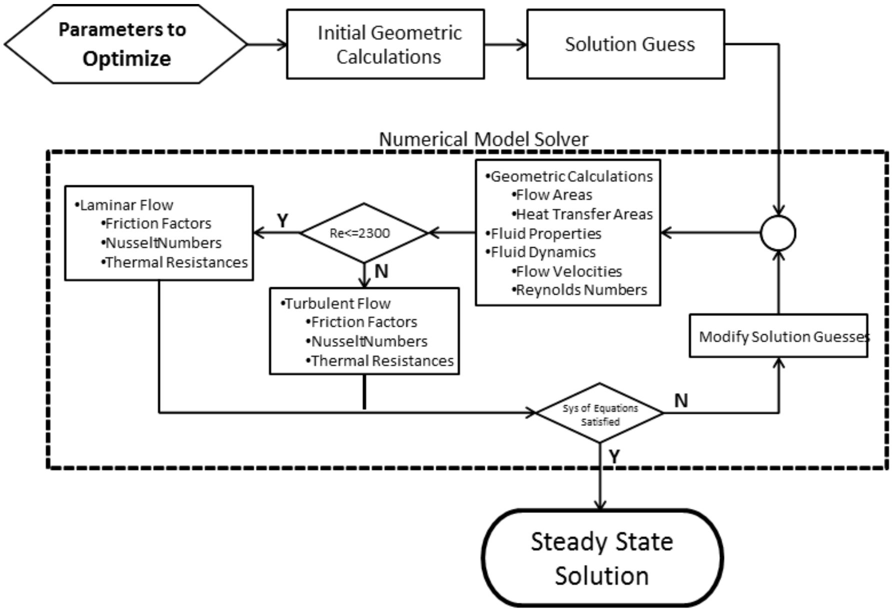

Figure 3.6 Numerical soluition of multi-physics model schematic

Once a solution has been reached, the output from the model is the values for the eight unknowns which solve the system of equations. The model also calculates additional data that may be used to further evaluate the system. Two measures of overall system performance, the device mounting temperature and total system thermal resistance are specifically examined. These outputs are given in Table 3.3.

Table 3.3. Multi-physics model output parameters

	Variable	Description
Steady State Solution Parameters (System of Equation Variables)	T_1	Hot Side Inlet Temp [°C]
	T_2	Hot Side Outlet Temp [°C]
	T_3	Cold Side Inlet Temp [°C]
	T_4	Cold Side Outlet Temp [°C]
	$\dot{m}$	Fluid Flow Rate [kg/s]
	Q_{UM}	Upper Manifold Rejection [W]
	Q_{CS}	Cold Side Rejection [W]
	Q_{LM}	Lower Manifold Rejection [W]
Steady State Performance Metrics	T_{mount}	Device Mounting Temperature [°C]
	R_{therm}	Baseplate Thermal Resistance [°C/W]

3.8 Model validation

A passive thermal management system (PTMS) was designed for a single convertor cell to facilitate initial validation of the model. The thermal load, mounting dimensions, and ambient temperatures reflect initial testing conditions. Heat transfer fluid was chosen to be ISO22 mineral oil. Geometric parameters were selected based on manufacturing considerations, prior knowledge, and iterative use of the model. The resulting inputs to the multi-physics model are compiled in Table 3.4.

Table 3.4. Selected parameters for model verification

	Parameter	**Units**	**Value**
Operating Conditions	Q_{in}	W	300
	L_{mount}	mm	152
	W_{mount}	mm	152
	T_{amb}	°C	25
	T_{surr}	°C	25
Geometric Variables	a_{HS}	mm	6.35
	b_{HS}	mm	25.4
	t_{HS}	mm	1.27
	a_{CS}	mm	6.35
	a_{amb}	mm	18.5
	$D_{manifold}$	mm	25.4
	N_{plates}	#	6

The predicted performance of the selected dimensions meets the testing target of 300W thermal load to 25 °C ambient. The operating parameters satisfying the steady state system of equations, and resulting performance metrics, are given in Table 3.5.

Table 3.5. 300W predicted operating parameters

	Parameter	Units	Value
Steady State Solution Parameters	T_1	°C	60.2
	T_2	°C	81.9
	T_3	°C	75.8
	T_4	°C	64.5
	$\dot{m}$	kg/s	0.00594
	Q_{UM}	W	76.5
	Q_{CS}	W	140.
	Q_{LM}	W	53.0
Steady State Performance Metrics	T_{mount}	°C	92.1
	R_{therm}	°C/W	.224

The selected dimensions were developed into a prototype demonstration thermosiphon, shown in Figure 3.7. Externally, the design features the silicon devices mounted to a copper spreader plate on the hot side. This plate is necessary to minimize hot spots directly behind the devices and spread heat to the larger hot side fin array. The cold side plate arrays are made from copper sheet metal and bar stock spacers, creating internal cavities for fluid flow. The plates are soldered to notched copper manifold pipes. The manifolds connect to the hot side via NPT compression fittings.

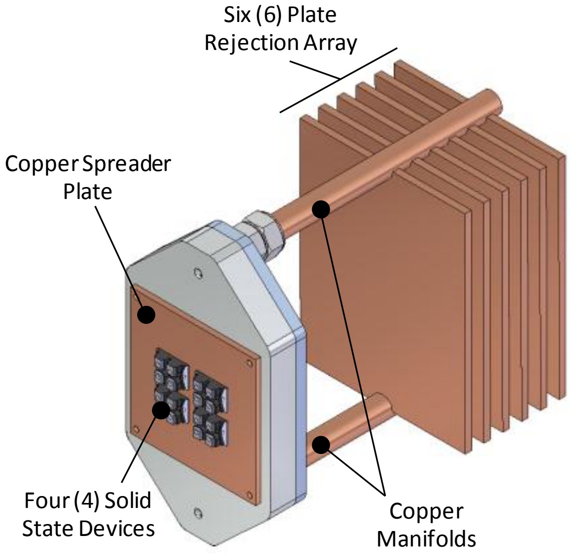

Figure 3.7. Isometric view of demonstration thermosiphon solid model

Internally, the hot side fins are machined directly into the hot side baseplate, creating twenty (20) rectangular flow channels, as illustrated in Figure 3.8 and Figure 3.9. The cold side channels internal to the cold side plates are also visible. This view demonstrates the significant area multiplication achieved by the design. The hot side area available for heat transfer to the fluid is roughly 45 times the base area of the devices. The cold side area to transfer heat to ambient is 150 times the device areas. The hot side fining reduces the thermal resistance between the devices and the fluid, decreasing the temperature gradient necessary to achieve a given heat flow. This allows the system to run with increased overall fluid temperatures for a specified baseplate temperature and thermal load. On the cold side, this increased fluid temperature is also beneficial to performance. The hollow plate design eliminates conduction losses that would be incurred with high aspect ratio fins, minimizing thermal resistance by instead separating the fluid and air by only a short conduction path. Increased fluid temperature results in a greater ΔT between the cold side and ambient air, further improving heat transfer.

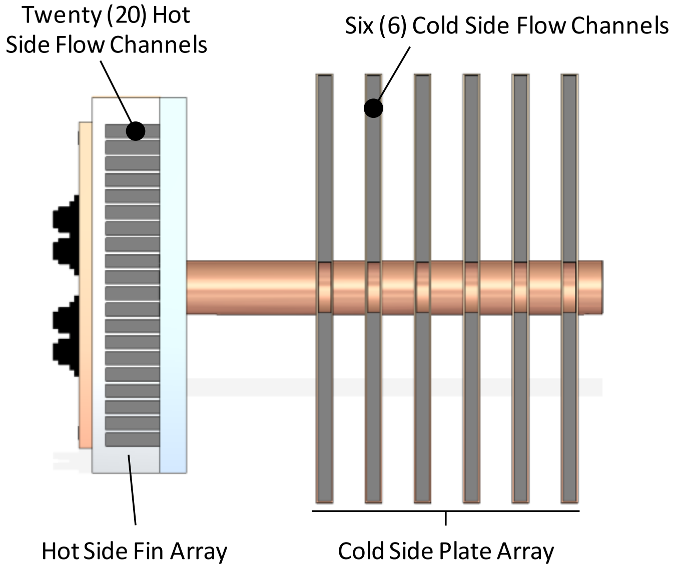

Figure 3.8. Sectional view of demonstration thermosiphon solid model

Figure 3.9 Machined hot side flow channels

The design target was to reject 300W from a single IDCL cell to 25 °C ambient while maintaining a device mounting temperature below 100 °C. Testing at multiple thermal loads allowed for evaluation of design performance against model prediction. The completed demonstration thermosiphon is pictured in Figure 3.10. Copper heater blocks are machined to match actual device mounting surfaces and cartridge heaters controlled by a variac are used to generate thermal load. A device mounting plate mates the heater to the thermosiphon hot side in a manner identical to the design for the solid state devices. The heaters are potted in thermally insulating epoxy to ensure 97% of the thermal load travels through the thermal management system.

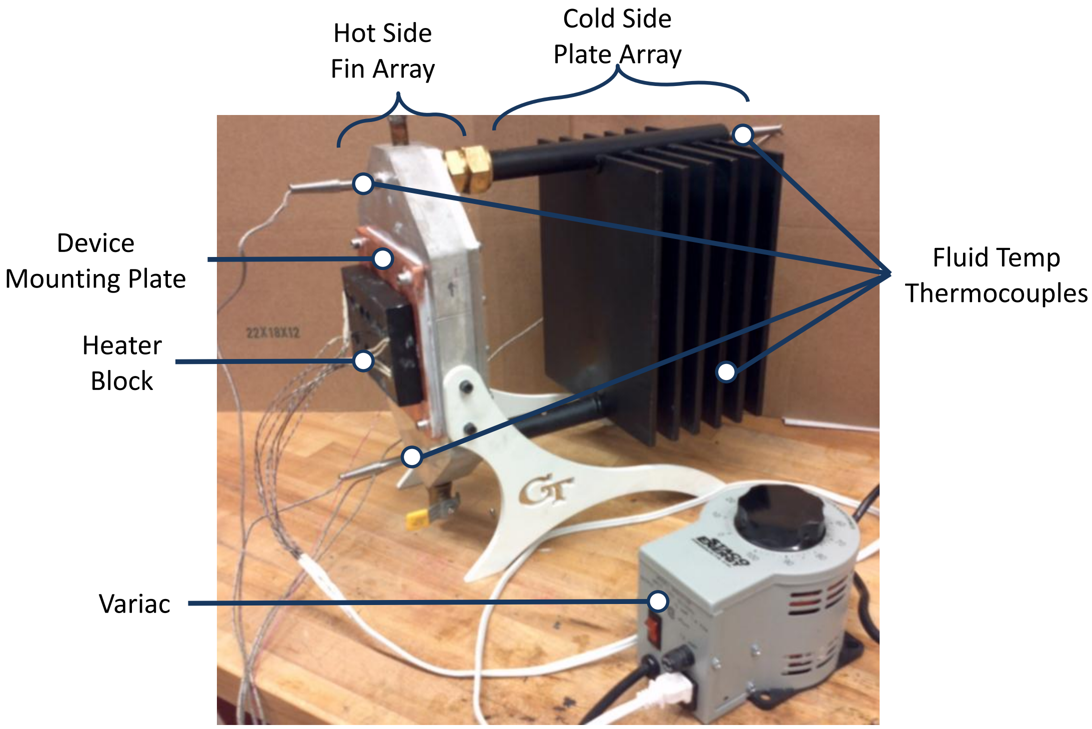

Figure 3.10 Demonstration thermosiphon for single IDCL cell

The thermosiphon is instrumented to allow collection of temperature data during operation. A surface thermocouple on the device mounting plane, between the heater block and the device mounting plate measures device mounting temperature. Fluid temperatures are measured using thermocouples placed at the ends of the upper and lower manifolds.

The demonstration thermosiphon was subjected to thermal loads of 100W, 200W, 300W, and 400W to allow comparison of performance to the multi-physics model. Each test began with the thermosiphon in equilibrium at zero thermal load. The heater circuit was stepped to the desired thermal load after data logging commenced. Figure 3.11 shows characteristic device mounting, fluid, and ambient temperatures for a full test cycle at 300W.

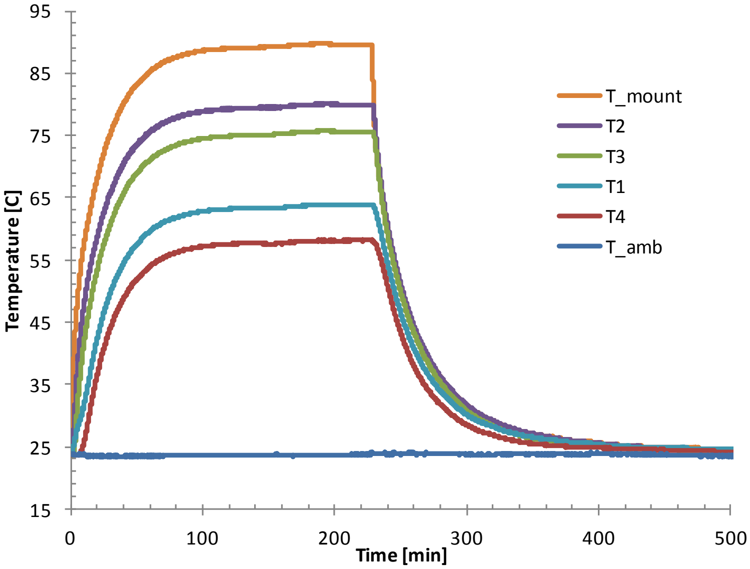

Figure 3.11. Transient and steady state performance for 300W step thermal load

Steady state operation was identified by the zero crossing of a 30 point moving average of dT/dt. During the periods identified at steady state, the standard deviation of all temperature measurements remained below 0.3 °C. Actual power input was calculated by measuring the input RMS voltage and heater circuit resistance during steady state operation. The apparatus used in the experiment are listed with their respective measurement uncertainties in Table 3.6.

Table 3.6. Apparatus and Uncertainty

Apparatus	Model	Uncertainty
Surface Thermocouple	Omega T-type	1.0 °C
Thermocouple	Omega T-type	1.0 °C
NPT Thermocouple Probe	Omega T-type	1.0 °C
Digital Voltmeter	Fluke Model 117	1.0% + 3 counts
Digital Ohmmeter	Fluke Model 117	0.9% + 2 counts
Variac	Staco 3PN1010	n/a
16 Ch. Thermocouple DAQ	NI 9213	n/a

Thermal load was determined by measuring the input voltage and heater circuit thermal resistance. Thermal load, *Q*, is equal to V^2/R. The power input and average temperatures recorded during steady state operation for each of the four power levels are given in Table 3.7. Steady state operation was identified by locating the zero crossing of a 30 point moving average of the rate of change of the mounting temperature. All temperatures increased with thermal load, as expected.

Table 3.7. Measured thermal loads and steady state temperatures

Thermal Load [W]	Mounting [°C]	Ambient [°C]	Hot Side Inlet [°C]	Hot Side Outlet [°C]	Cold Side Inlet [°C]	Cold Side Outlet [°C]
100.9	51.4	23.8	40.4	48.6	45.6	36.3
195.4	70.2	23.7	51.4	63.9	60.0	46.1
300.2	88.9	23.8	63.2	79.3	74.9	57.2
401.2	105.4	23.6	73.6	92.7	87.9	67.1

Equipment measurement uncertainties were considered to determine the total experimental uncertainty for the data. Experimental uncertainty was calculated using Kline and McClintock's method for single measurement uncertainty [69]. The individual measurements and the associated uncertainties are presented in Table 3.8.

Table 3.8. Measurement uncertainty analysis

Power [W]	σP [W]	T_{mounting} [°C]	T_{ambient} [°C]	ΔT [°C]	$\sigma \Delta T$ [°C]	R_{thermal} [°C/W]	$\sigma R_{\text{thermal}}$ [°C/W]	Uncertainty [%]
100.9	6.75	51.9	23.8	28.1	1.41	0.279	0.0233	8.37
195.4	12.10	70.2	23.7	46.5	1.41	0.238	0.0164	6.90
300.2	17.84	88.9	23.8	65.1	1.41	0.217	0.0137	6.33
401.2	23.28	105.4	23.6	81.8	1.41	0.204	0.0123	6.06

The majority of uncertainty in the system thermal resistance derived from the uncertainty of the power measurement. The power was calculated from the heater resistance and voltage across as $P=V^2/R$. In Kline McClintock, the uncertainty of the voltage measurement is amplified by its power of two in the calculation.

The model was evaluated for each experimental thermal load and average ambient temperature. The comparison of experimental device mounting temperatures and thermal resistances with those predicted by the model is given in

Table 3.9.

Table 3.9. Comparison of experimental data with model predictions

Power [W]	$T_{mount,exp}$ [°C]	$T_{mount, model}$ [°C]	$\Delta T_{mount,}$ [°C]	$R_{therm,exp}$ [°C/W]	$R_{therm,model}$ [°C/W]	R_{therm} Error [%]
100.91	51.9	49.5	-2.4	0.279	0.257	7.90
195.41	70.2	67.6	-2.6	0.238	0.225	5.44
300.22	88.9	85.7	-3.2	0.217	0.207	4.68
401.16	105.4	101.7	-3.7	0.204	0.195	4.50

The experimental device mounting temperatures and experimental error are plotted along with the model prediction curve in Figure 3.12. The measurements differ from the model by more than the measurement uncertainty, but are within 4 °C of prediction. Total system thermal resistance data are compared with the model in Figure 3.13. These measure the total thermal resistance from the device mounting plate to ambient. Here, the measurement uncertainty includes the model prediction and is within 8%.

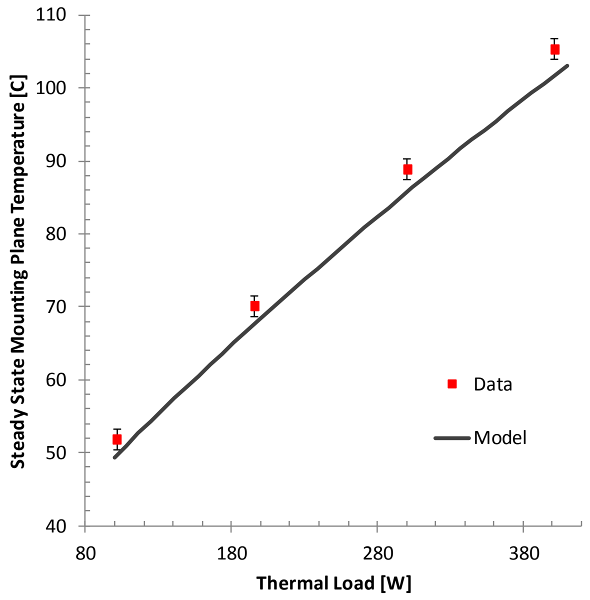

Figure 3.12. Comparison of model and experimental device mounting plane temperatures

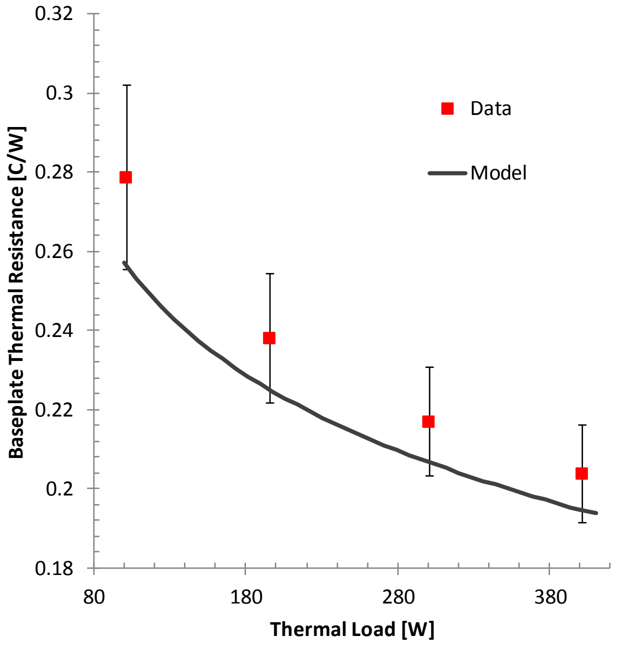

Figure 3.13. Comparison of model and experimental total baseplate to ambient thermal resistances

3.9 Discussion

Maximum disagreement between the model and experimental data was 8% for thermal resistance and 3.7 °C for device mounting temperature. At every tested load, the model predicted the baseplate thermal resistance to within the experimental uncertainty. The relatively high uncertainty in thermal resistance measurements results largely from the measurement uncertainty involved in determining the actual power input to the system via voltage and resistance measurements. The consistent over-prediction of thermosiphon performance by the model is small, but critical in system design applications. Investigations into model sensitivity revealed particular sensitivity to fluid properties. The temperature dependent properties of the common commercial mineral oil used as the heat transfer fluid are not as well defined as would be expected with a more expensive engineered fluid. Other simplifications made in the model may cause additional deviations from true operation. Conduction paths transverse to bulk heat flow are neglected, eliminating some minor spreading effects that may enhance overall heat transfer from some surfaces. Finally, conduction within the fluid is neglected, and could be non-negligible at low flow rates predicted. The demonstration thermosiphon strengthened the validity of the multi-physics model and its suitability for use in a multi-physics design optimization.

A sensitivity study was performed to assess the impact of variations in model parameters on overall system performance prediction. The internal heat transfer coefficients in the hot and cold sides were chosen specifically because they are the dominating heat transfer locations in the system. The development of hydrodynamic and thermal boundary layers is accounted for generically in the average Nusselt number correlations used to predict these heat transfer coefficients. It is of concern that the correlation used in the model may be too general for this application. The effect of percentage changes in predicted heat transfer coefficients on the overall system performance are presented in Table 3.10.

Table 3.10 System performance sensitivity to internal heat transfer coefficients

Δ h_{HS}	**-10%**	**-5%**	**-2%**	**Model**	**+2%**	**+5%**	**+10%**
T_{device} [°C]	89.1	87.9	87.3	**86.8**	86.4	85.8	85.0
$R_{Baseplate}$ [°C/W]	.2138	.2097	.2075	**.2061**	.2048	.2028	.1998
Δ $R_{baseplate}$ [%]	3.7%	1.7%	.68%	**-**	-.63%	-1.6%	-3.1%
Δ h_{CS}	**-10%**	**-5%**	**-2%**	**Model**	**+2%**	**+5%**	**+10%**
T_{device} [°C]	87.0	86.9	86.9	**86.8**	86.8	86.8	86.7
$R_{Baseplate}$ [°C/W]	.2068	.2064	.2062	**.2061**	.2060	.2058	.2056
Δ $R_{baseplate}$ [%]	.34%	.15%	.05%	**-**	-.05%	-.15%	-.24%

The sensitivity study shows that fluctuations in the internal heat transfer coefficients of the hot and cold sides have minimal impact on the predicted overall system performance. Heat transfer deviations as large as 10% will have less than 4% impact on total system thermal resistance. These same deviations affect the predicted device temperature by less than 2 °C. Still, more advanced correlations may be included to potentially bring the model into closer agreement with experimental data. Improved heat transfer correlations, as presented in [70], may also be introduced to further trim the model to a particular application. A sensitivity study was also performed on the total flow loss in the fluid loop, as presented in Table 3.11

Table 3.11 System performance sensitivity to fluid pressure flow loss

Δ P_{loss}	**-10%**	**-5%**	**-2%**	**Model**	**+2%**	**+5%**	**+10%**
T_{device} [°C]	86.4	86.6	86.8	**86.8**	86.8	87.0	87.2
$R_{Baseplate}$ [°C/W]	.2048	.2055	.2059	**.2061**	.2064	.2067	.2073
Δ $R_{baseplate}$ [%]	.63%	.29%	.10%	**-**	-.15%	-.29%	-.58%

Similarly, varying the total flow losses in the system does not significantly affect the overall predicted system performance. Fluid correlations were chosen to be general to give the design tool added flexibility. Correlations from Idelchik [65] may be included to refine the model when the geometry details are better known. This reference contains loss calculations for a wide variety of geometries and transitions that may be applied to capture the specifics of a given design.

The analytical model solves numerically in less than 0.05 seconds on a modern desktop PC with 3.20 GHz processor.

3.10 Summary

A parametric multi-physics model for a feature enhanced single-phase closed-loop thermosiphon is presented. A demonstration thermosiphon is built for evaluation of the model predictions. Maximum disagreement between the model and experimental data was 8% for thermal resistance and 3.7 °C for device mounting temperature. The model appears to accurately predict the performance of the system. The code solves the model in less than 0.05 seconds, suitable for iterative use in numerical optimization techniques.

CHAPTER 4

NUMERICAL OPTIMIZATION

4.1 Introduction

The analytical model developed in Chapter 3 was developed specifically for used in numerical optimization and will be used in a particle swarm optimization (PSO) to pursue an optimal thermosiphon design for an existing set of thermal management requirements. Particle swarm optimization has been identified as an optimization method well suited for solving large-scale non-linear optimization problems [63]. Particle swarm optimization was introduced in 1995 by Kennedy and Eberhart [62]. This method of optimization uses an iterative approach to identify an optimal solution. Initially, a finite number of parameter sets, known as “particles”, are distributed randomly throughout the user defined solution space. Each particle is solved and evaluated using an objective function. A global best is identified, and the particles each take a finite step in all dimensions of the solution space towards the best particle. The particles are re-evaluated at their new positions, and a new best is identified. This process iterates until the particles converge to an optimal parameter set. A stochastic parameter is included in each particle position and velocity change such that the particles are perturbed as they converge ensuring that particles locate the global minimum in the design space.

The geometric design parameters identified in the Chapter 3 will be manipulated within assigned bounds inside the PSO to arrive at a design that best meets performance, manufacturability, and size requirements as defined by an objective function. The objective function is used to compare the suitability of each design iteration, allowing the optimization to move towards an optimal design.

4.2 Design problem statement

This section identifies the parameters that define the design problem as well as the geometric parameters that will be manipulated to reach and thermosiphon design.

4.2.1 Problem definition

The numerical optimization seeks to use the multi-physics model to size a passive thermal management system for a prescribed combination of thermal load, baseplate dimensions, and ambient conditions. These target values are shown in Table 4.1 and, along with the power electronics temperature limitations, fully describe the most fundamental requirements of the thermal management system.

Table 4.1 Problem Definition Parameters

	Variable	Description	Target
Operating Conditions (Problem Definition)	Q_{in}	Thermal Load [W]	2500
	L_{mount}	Device Mounting Length [in]	20
	W_{mount}	Device Mounting Width [in]	13
	T_{amb}	Ambient Temperature [°C]	40
	T_{surr}	Surrounding Temperature [°C]	40

The design must be capable of rejecting 2.5kW thermal load to 40 °C ambient air. The system must accommodate the 2.5kW thermal load via 6 IDCL cells in a 3x2 array, as dictated by the system circuitry and illustrated in Figure 4.1. The cells are each 6” square, and will be spaced 1” apart, dictating baseplate dimensions of 13” wide and 20” long.

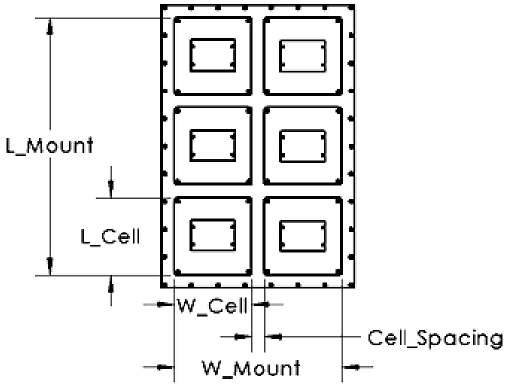

Figure 4.1 Hot side device arrangement

In addition to the problem definition parameters, additional values are defined by the user based on anticipated material selection and fabrication technique. Material properties must be specified for the thermosiphon sections and the working fluid. For the unknown geometries to be optimized, upper and lower bounds are specified as discussed below.

4.2.2 Design variables and domains

Seven critical geometries are identified for parametric design optimization. These variables have been discussed in detail in the Chapter 3 and are listed in Table 4.2 and illustrated in Figure 4.2 for reference. The PSO will seek the combination of these parameters that best satisfies the objective function.

Table 4.2 Geometric Design Variables

	Variable	Description
Geometric Parameters (Design Variables)	a_{HS}	Hot Side Channel Width [m]
	b_{HS}	Hot Side Channel Depth [m]
	t_{HS}	Hot Side Fin Thickness [m]
	a_{CS}	Cold Side Channel Width [m]
	a_{amb}	Plate Spacing [m]
	$D_{manifold}$	Manifold Diameter [m]
	N_{plates}	Number Cold Side Plates

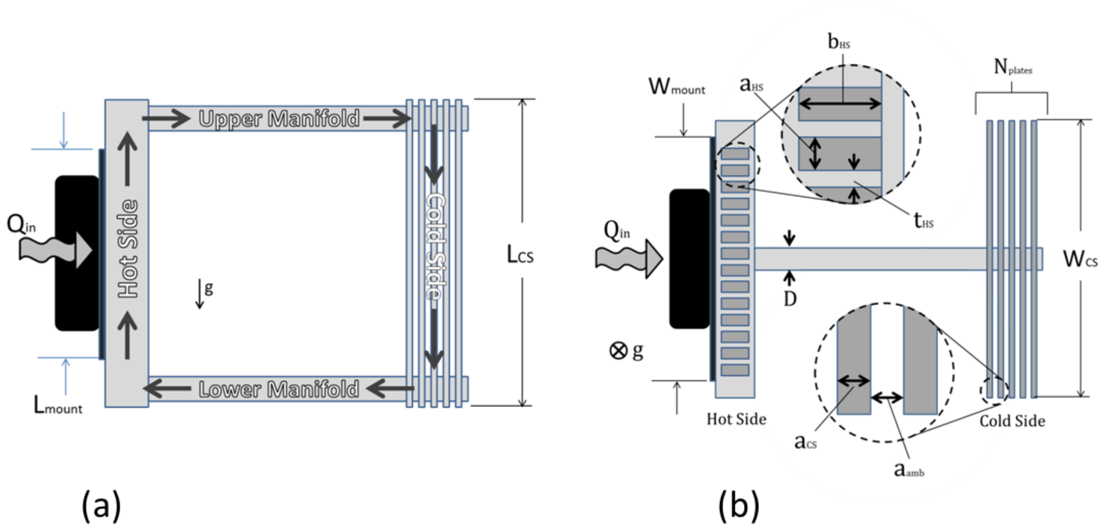

Figure 4.2 Critical geometric parameters (a) side view and (b) top section view

4.3 Implementation

The particle swarm optimization routine was implemented in Matlab® using code available on the Matlab® file exchange web page [71] with modifications. The thermosiphon model and supporting code blocks were written to create a functional multi-physics design optimization package.

4.3.1 Objective function

The objective function evaluates each particle based on three metrics. First, any design that does not result in an operational thermosiphon, as indicated by lack of convergence of the model, is penalized to the arbitrarily large value of 10^9. Particles that are successfully solved by the model are evaluated based on maximum device mounting temperature and total system volume according to Equation (4.1).

$$
\left.
\begin{aligned}
J &= 1x10^{9}; & \sum Q > 1W \ or \sum \Delta P > 1e^{-2}Pa \\
&= C_1 \times Volume + C_2 \times \theta^{4}; & T_{SS} > T_{\text{target}} \\
&= C_1 \times Volume + C_2 \times \theta^{2}; & T_{SS} < T_{\text{target}}
\end{aligned}
\right\} \qquad (4.1)
$$

$$where \ \ \theta = T_{SS} - T_{\text{target}}$$

Constants C_1 and C_2 are used to adjust the relative influence of the temperature deviation and system volume on the return of the objective function. The objective function allows for solutions above and below the target temperature, but penalizes those above the target more severely using the 4th power on temperatures above target compared to a 2nd power for temperatures below the target. The final objective function output is the sum of the penalty for deviation from target temperature and the linear penalty for total system volume.

4.3.2 PSO program structure

A schematic of the PSO code structure is illustrated in Figure 4.3. The optimization routine is initiated by defining the problem definition parameters (Table 4.1) and bounds on the geometric design optimization variables (Table 4.2) in the *PSO Main* code block.

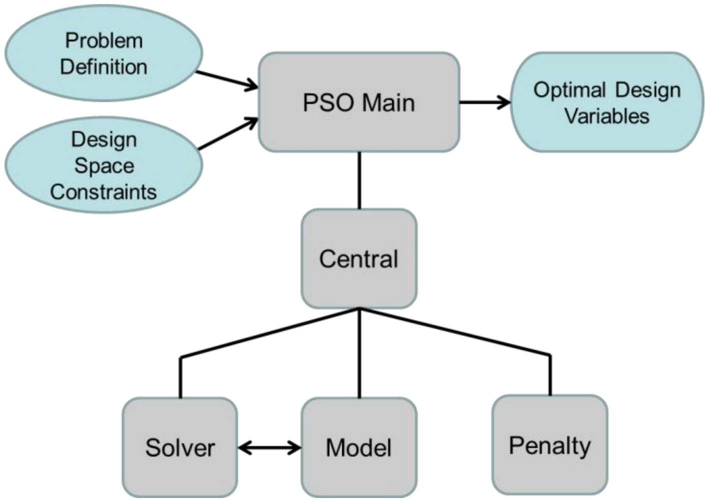

Figure 4.3 Multi-physics Design Optimization Flow Diagram

The *PSO Main* code randomly generates the first epoch of particles and appends a vector of the problem definition parameters and constants to each particle position vector. These particle vectors are sent to the *Central* code block for additional geometric calculations involving the design optimization variables. The particle vectors are then used in the *Solver* function call, which utilizes a built in non-linear system of equations solver to solve the *Model* function. *Solver* returns the steady state solution variables to *Central*. *Central* then calls *Model* directly using the solution variables. *Model* returns vectors of various operating parameters, including areas, Nusselt numbers, heat transfer coefficients, fluid velocities, Reynolds numbers, and pressures to *Central*. The predicted steady state device temperature and total system volume are sent to *Penalty*, and the result is returned to *PSO Main* via *Central*. Each particle's penalty is used by *PSO Main* to generate particle velocity gradients and the particles locations for the next epoch are calculated. This process continues until the convergence criterion is met and an optimal design is reached. The Problem Definition and Design Space Constraints are inputs to the *PSO Main* code and the Optimal Design Variables resulting from the optimization described above are the outputs. The system of equations and unknowns identified in Chapter 3 are repeated in

Table 4.3 for reference.

Table 4.3 System of equations and unknown variables

Eight Equations	Eight Unknowns
$Q_{in} = \dot{m}c_p(T_2 - T_1) - Q_{HS,loss}$	T_1
$Q_{UM} = \dot{m}c_p(T_2 - T_3)$	T_2
$Q_{CS} = \dot{m}c_p(T_3 - T_4)$	T_3
$Q_{LM} = \dot{m}c_p(T_4 - T_1)$	T_4
$\Delta P_{HS} + \Delta P_{UM} + \Delta P_{CS} + \Delta P_{LM} = 0$	$\dot{m}$
$Q_{UM} = \frac{(T_{UM} - T_{amb})}{R_{UM}}$	Q_{UM}
$Q_{CS} = \frac{(T_{CS} - T_{amb})}{R_{CS}}$	Q_{CS}
$Q_{LM} = \frac{(T_{LM} - T_{amb})}{R_{LM}}$	Q_{LM}

4.3.3 Particle weighting and convergence criteria

Particle weights were held constant at unity and no concerns with convergence were observed. The convergence criterion was set to terminate the optimization routine when the standard deviation of the particle penalties fell below 0.01.

4.4 Optimal design space investigation

In addition to the penalty function, the use of variable bounds within the PSO allows the user to impose limits on the solution space to suit manufacturability and complexity concerns. Manipulation of bounds also allows for a cursory investigation of the impact of particular dimensions on the optimal design space. The relationship between hot side fin array size and cold side rejection array size was of particular interest. A lower resistance hot side results in greater fluid temperatures. Greater fluid temperatures increase the temperature gradient between the cold side and ambient, reducing the required area.

The MDO can be used to investigate the effect of constraining one variable on the optimal solution resulting from the manipulation of the others. The relation between hot side fin height, b_{HS}, and the number of cold side plates, $N_{plates,}$ needed is explored by fixing b_{HS} when initializing the optimization. The optimization was run for several fixed hot side fin heights and the number of plates and objective function returns were recorded. The effect of increasing b_{HS} on the number of plates required is plotted in Figure 4.4. A plateau of diminishing returns is obvious, resulting from decreased fin efficiency for higher aspect ratio fins.

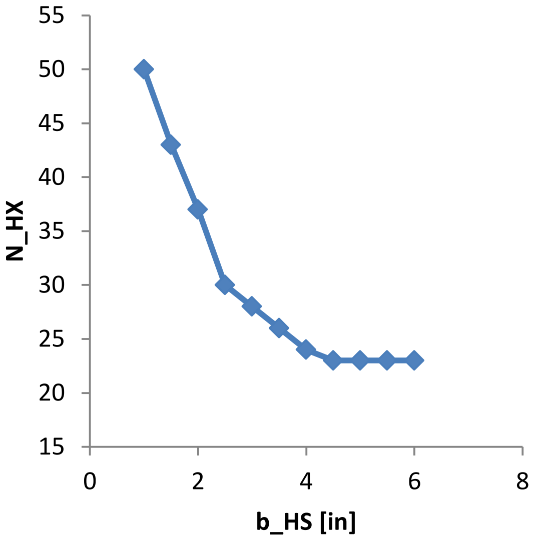

Figure 4.4 Investigation of effect of b_{HS} on N_{plates} in optimal design

4.5 Final design

The particle swarm optimization was performed as detailed in the preceding sections. Five optimizations trials converged to the same solution, indicating the global minimum was reached. The upper bound of the number of cold side plates was reduced to limit fabrication expense, and the PSO was run for 5 more trials to identify the final geometries. A solid model of the design incorporating the optimized geometries is presented and the performance of the design is predicted using the multi-physics model.

4.5.1 Design selection

A design for a 2.5kW to 40 °C passive thermal management system was developed using the multi-physics model validated by the demonstration thermosiphon and the numerical design optimization,. The system accommodates six (6) IDCL cells totaling 2.5kW thermal load at a maximum device mounting temperature of 100 °C. Midel® 7131 engineered heat transfer fluid was donated by the manufacturer and its properties were coded into the model. Copper was selected as the hot side fin array material to allow the machining and assembly of a custom high aspect ratio fin array in house. Aluminum was selected for the hot side plenum material for its light weight and machining properties. All manifolds and the cold side array were designated to be mild steel for strength, manufacturability and cost. The design parameters were bounded based on material availability and manufacturing limitations. These bounds are presented in Table 4.4.

Table 4.4 Particle swarm variables and bounds

	Variable	Description	Lower Bound	Upper Bound	Units
Geometric Parameters (Design Variables)	a_{HS}	Hot Side Channel Width	.05	1	[in]
	b_{HS}	Hot Side Channel Depth	.1	4	[in]
	t_{HS}	Hot Side Fin Thickness	.05	.25	[in]
	a_{CS}	Cold Side Channel Width	.05	.5	[in]
	a_{amb}	Plate Spacing	.1	1	[in]
	$D_{manifold}$	Manifold Diameter	2	4	[in]
	N_{plates}	Number Cold Side Plates	2	30	

The PSO was run several times to ensure convergence. These trails and their objective function values are compiled in Table 4.5. The first 5 trials were completed with the bounds presented in Table 4.4. For trials 5 through 10, the upper bound of N_{plates} was reduced to 20 to reduce the number of plates to be manufactured. The values are nearly identical to four significant digits, though differences were observed in further decimal places.

Table 4.5 PSO trial results

	Solutions Time [s]	Penalty	T_{device} [°C]	a_{HS} [in]	b_{HS} [in]	t_{HS} [in]	$D_{manifold}$ [in]	a_{CS} [in]	a_{CS} [in]	N_{plates}
1	49.30	15.02	95.00	0.250	4.00	0.132	3.00	0.282	0.66	23.99
2	52.55	15.38	95.00	0.250	4.00	0.132	3.00	0.279	0.74	22.62
3	60.76	14.79	95.00	0.250	4.00	0.132	3.00	0.264	0.62	24.78
4	58.90	14.77	95.00	0.250	4.00	0.132	3.00	0.253	0.63	24.92
5	60.61	14.78	95.00	0.250	4.00	0.132	3.00	0.261	0.62	24.59
6	50.24	27.32	95.73	0.250	4.00	0.122	3.00	0.333	1.00	19.55
7	48.66	27.46	95.76	0.250	4.00	0.132	3.00	0.340	1.00	19.69
8	58.10	27.46	95.76	0.250	4.00	0.132	3.00	0.340	1.00	19.69
9	52.87	27.46	95.76	0.250	4.00	0.132	3.00	0.340	1.00	19.84
10	55.75	27.46	95.76	0.250	4.00	0.132	3.00	0.340	1.00	19.74

Multiple runs identified similar minimums of the objective function. The values were rounded to the nearest English standard fraction for manufacturing purposes and the model was used to confirm the continued satisfactory performance of the standardized dimensions. The final design parameters resulting from the PSO are presented in Table 4.6. Solution time averaged 54.8 seconds on a quad core desktop PC running parallel processing.

Table 4.6 Final design parameters from multiphysics design optimization

Variable	Parameter	units	Value
HS Channel Width	a_{HS}	[in]	0.256
HS Channel Height	b_{HS}	[in]	4.0
HS fin thickness	t_{HS}	[in]	0.125
CS channel width	a_{CS}	[in]	0.25
Ambient channel width	a_{amb}	[in]	0.75
Manifold diameter	$D_{manifold}$	[in]	3.0
Number ambient arrays	N_{plates}	#	20

From the multi-physics design parameters, a solid model of the final design was developed, including provisions for assembly, filling, venting, draining, electrical integration, positioning and instrumentation. A solid model of the design is illustrated in Figure 4.5. This twelve (12) cell IDCL design is comprised of two 2.5kW thermal load modules. Each module accommodates six (6) IDCL cells on individual copper device mounting plates. These mounting plates bolt directly to the single copper hot side fin array, allowing cells to be replaced individually. The hot and cold side subassemblies mount to either side of the frame bulkhead. The bulkhead is designed to support each subassembly individually, simplifying assembly and maintenance. This design is described in detail in Chapter 5.

Figure 4.5. 5kW to 40 °C Design a) Front isometric b) Rear isometric c) Front view d) Side view

4.5.2 Predicted performance

The multi-physics model allows prediction of system performance at various thermal loads and ambient temperatures. The predicted device mounting temperatures and system thermal resistances for a range of thermal loads and ambient temperatures are plotted in Figure 4.6. The design is predicted to maintain device mounting temperatures under the design threshold of 100 °C for all operating conditions. These results will be compared to experimental measurements in the following chapter.

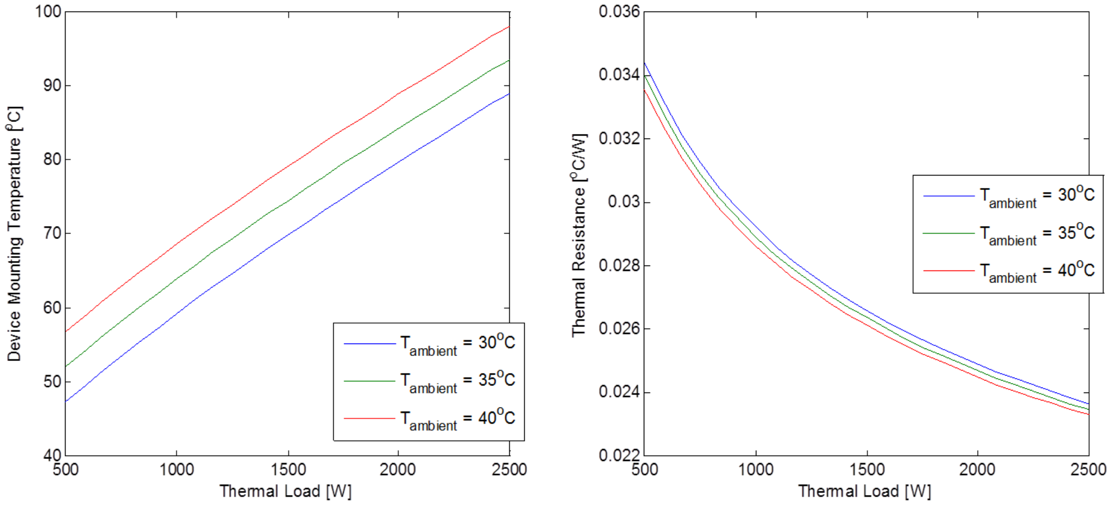

Figure 4.6 Predicted device mounting temperature and thermal resistance

4.6 Discussion

The analytical model presented in Chapter 3 solves numerically in less than 0.05 seconds on a modern, quad-core desktop PC. This short solution time enables the model to be used in numerical optimization to create a rapid design sizing tool. The model also allows for quick evaluation of the impact of specific parameters on system performance. Material properties may be modified to investigate the use of different materials in different parts of the thermosiphon. The model also allows comparison of different heat transfer fluids. The optimization was performed using Midel® 7131 fluid based on the following analysis. The fluid properties relevant to the model and thermosiphon performance are presented in Table 4.7 along with other factors of concern for real work implementation. A '+' indicates the fluid with the property values most beneficial to thermosiphon performance or implementation. The Midel® fluid has significantly greater coefficient of thermal expansion, significantly lower viscosity, and slightly greater density. ISO 22 mineral oil is equally conductive and has greater specific heat. From these, it is found that the mineral oil has higher thermal diffusivity while the Midel® has a higher Prandtl number. In pragmatic terms, Midel® offers advantages in all categories apart from cost.

Table 4.7 Comparison of potential heat transfer fluids

ISO 22 Mineral Oil	Metric	Midel 7131
	Expansion Coefficient	++
	Viscosity	++
=	Conductivity	=
	Density	+
+	Specific Heat	
+	Thermal Diffusivity	
	Prandtl	+
+	Cost	
	Global Warming Potential	+
	Ozone Depletion	+
	Toxicity	+
	Life	+

Considering the metrics in the comparative table offers clues to the relative advantages of each fluid. The model allows easy comparison of the performance of each fluid in a given thermosiphon. The model was run for each fluid for the dimensions of the demonstration thermosiphon presented in Chapter 3. The predicted device temperatures and system thermal resistances are plotted in Figure 4.7. The Midel® fluid is predicted to offer improved PTMS performance at all thermal loads.

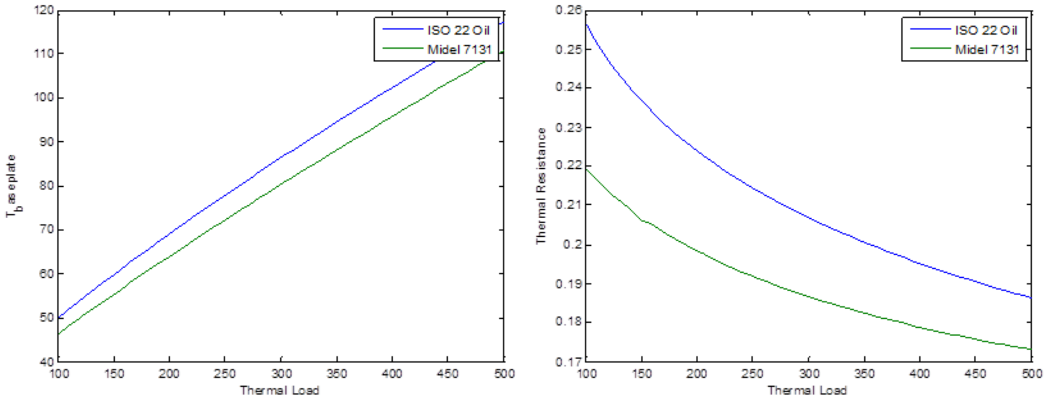

Figure 4.7 Comparison of predicted performance ce of ISO 22 mineral oil and Midel® 7131 in the demonstration thermosiphon

4.7 Conclusion

This chapter presents the application of a particle swarm optimization (PSO) to the thermosiphon model developed and validated in Chapter 3. The problem was defined by the 2.5kW thermal load, 40 C ambient conditions, 13” x 20” device mounting area, and 95 C target device mounting temperature. Midel® 7131 engineered heat transfer fluid was selected over ISO 22 mineral oil for use in the PTMS. Optimization parameter bounds were set based on material availability and manufacturing considerations. The PSO was run multiple times and agreement between trials indicated convergence to the global minimum. The upper bound of the N_{plates} parameter was modified to impose a desired constraint of twenty or fewer cold side plates. The PSO determined the best combination of geometries to produce a functional thermosiphon with twenty cold side plates. PSO solution time averaged 54.7 seconds on a quad core desktop PC running parallel processing. The building and testing of the PTMS is presented in Chapter 5.

CHAPTER 5

DESIGN TOOL VALIDATION

5.1 Introduction

The multi-physics model detailed in Chapter 3 is implemented in the particle swarm optimization (PSO) presented in Chapter 4 to create a powerful passive thermal management system (PTMS) multi-physics design optimization (MDO) suitable for rapid design sizing. The critical thermosiphon geometries selected by the PSO were incorporated into a thermosiphon design as discussed in Chapter 4. This design was fabricated and instrumented for various temperature measurements. Heaters were fabricated to simulate the distribution and magnitude of thermal load expected from the power electronics. An elevated ambient testing chamber was constructed to allow testing of the PTMS at elevated temperatures. Tests were run at target thermal load of 2500W in ambient conditions of 30 °C, 35 °C, and 40 °C. Fluid and surface temperatures were recorded and the steady state performance of the system is evaluated. At 2500 W thermal load and 40 °C ambient temperature, a maximum steady state device mounting temperature of 98.0 °C was recorded, below the limiting temperature of 100 °C. This corresponds to a baseplate thermal resistance of 0.0232 °C/W. The results are compared to those predicted by the model to evaluate the efficacy of the multi-physics design optimization design tool. Device mounting temperature data are within 1.1 °C of model prediction. System thermal resistance is within 2% of predicted. Examination of fluid temperatures measurements reveals disagreements as large as 29 °C between experiment and model. Evaluation of the model exposed an incorrect assumption with regard to flow regime inside the fluid loop. The model is updated with appropriate assumptions, reducing the maximum fluid temperature disagreement to 8 °C.

5.2 Approach

The PTMS rapid design sizing tool will be evaluated by testing a PTMS built to the geometries identified in Chapter 4. Thermosiphon performance is evaluated at a constant thermal load of 2500W and at ambient temperatures of 30 °C, 35 °C, and 40 °C. The thermosiphon is placed in the elevated ambient testing chamber, and a thermal load is introduced to the thermosiphon via electrical heaters. The thermosiphon is held at constant thermal load and ambient temperature until steady state is reached. The maximum average device mounting temperature is used to evaluate the system performance and baseplate thermal resistance.

5.3 Apparatus

Evaluation of the multi-physics design optimization (MDO) requires real world testing of the thermosiphon dimensions resulting from the optimization. The thermosiphon presented at the end of Chapter 4 was fabricated. A testing chamber was built to allow evaluation of thermosiphon performance at elevated ambient conditions. A digital PID controller and data acquisition (DAQ) system were implemented to control the testing chamber and record temperature data from the thermosiphon. The construction of the thermosiphon, design and commissioning of the elevated ambient testing chamber, and the details of the DAQ system are presented in the following sections.

5.3.1 Passive thermal management system

The MDO was implemented as detailed in Chapter 4 to design a 2.5kW passive thermal management system (PTMS) module. The critical geometries selected using the optimization are repeated in Table 4.6 for reference.

Table 5.1 Final design parameters from multiphysics design optimization

Variable	Parameter	units	Value
HS Channel Width	a_{HS}	[in]	0.256
HS Channel Height	b_{HS}	[in]	4.0
HS fin thickness	t_{HS}	[in]	0.125
CS channel width	a_{CS}	[in]	0.25
Ambient channel width	a_{amb}	[in]	0.75
Manifold diameter	$D_{manifold}$	[in]	3.0
Number ambient arrays	N_{plates}	#	20

These geometries are used as the basis of the thermosiphon design. Practical design details, such as provisions for assembly, filling, venting, draining, electrical integration, positioning and instrumentation are included in developing a complete final design. A solid model of the final design is illustrated in Figure 5.1.

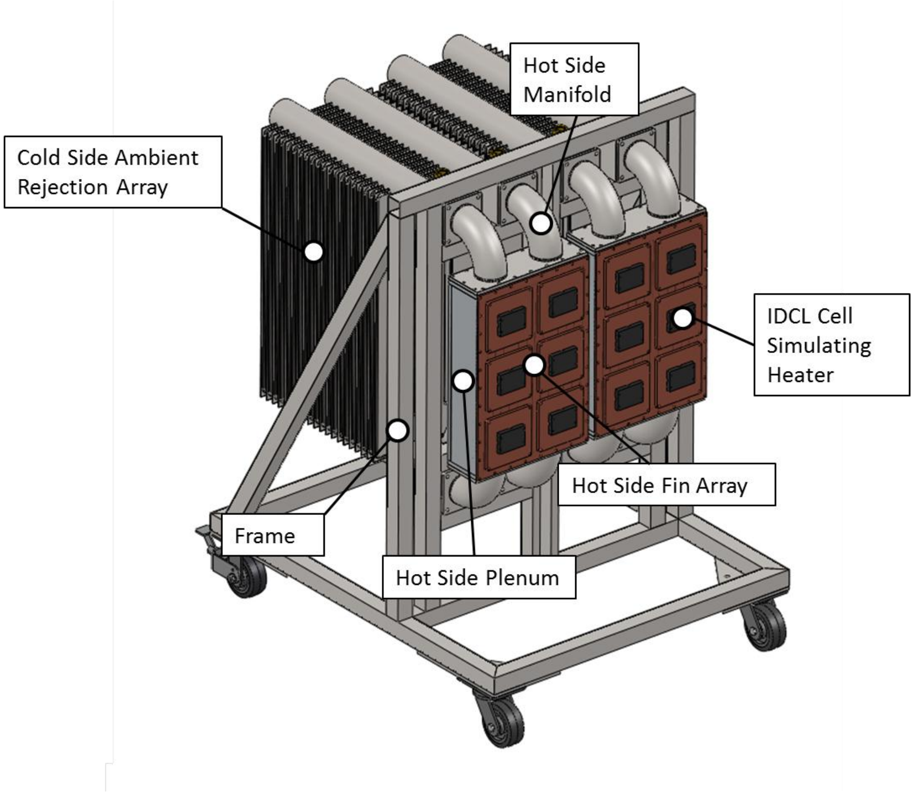

Figure 5.1 5 kW to 40 °C design consisting of two 2.5kW modules in parallel

This twelve (12) cell IDCL design depicted above is comprised of two identical 2.5kW thermal load modules. Each 2.5 kW module accommodates six (6) IDCL cells on individual copper device mounting plates. These mounting plates bolt directly to the single copper hot side fin array, allowing cells to be replaced individually. The hot and cold side subassemblies mount to either side of the frame bulkhead. The frame is designed to support the hot and cold sides individually, simplifying assembly and maintenance. The bulkhead also serves as the fluid coupling between the hot side and cold side manifolds and contains the necessary fluid fill and drain fittings. The frame was constructed from welded steel square tubing and powder coated black.

The cold side ambient rejection array was custom built. Schedule 40 3” steel pipe was used for the manifolds. The hollow plates were made from formed steel sheet with seam welds around the periphery. Slotted half pipes were welded to the twenty hollow plates from the inside, allowing full sealing and the desired plate spacing. These half pipes were then welded to the upper and lower manifolds to complete the ambient rejection array assembly. An external and internal view of the plate to manifold welding is depicted in Figure 5.2 below.

Figure 5.2 Cold side plate welding (a) external detail and (b) internal detail

The hot side fin array was manufactured by soldering copper plate fins into machined channels in a copper fin array baseplate. A 15”x20”x3/8” copper baseplate was machined with grooves for each 1/8” thick fin, as shown in Figure 5.3. The fins themselves were water-jet cut from 1/8” copper sheet. After machining operations were complete, the fins and baseplate were cleaned and prepared for soldering. Solder wire was placed in the machined fin grooves and the baseplate was heated on a larger propane burner.

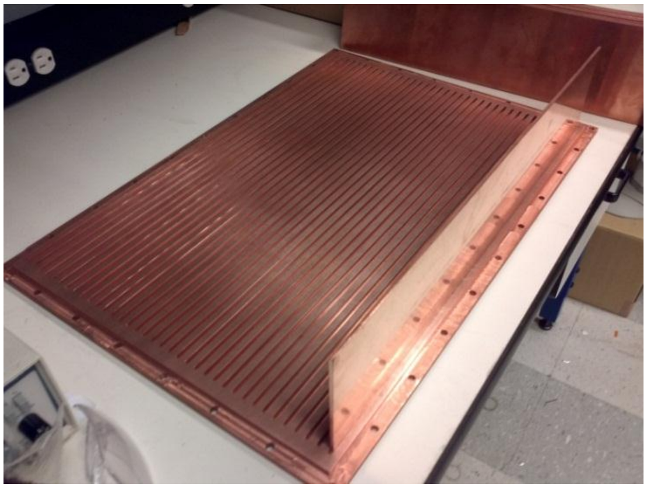

Figure 5.3 Machined fin grooves in hot side fin array baseplate

The fins were fit into the grooves and, when the solder reached melting temperature of 190 °C, were clamped into the grooves until fully seated. Excess solder wicked out of the joints, ensuring complete bonding. The mating flange of the hot side fin array was machined flat to ensure sealing with the plenum as shown in Figure 5.4.

Figure 5.4 Machining of hot side fin array mounting flange

The hot side plenum was fabricated from ½” aluminum plate. The various pieces were water-jet to size and weld fillets were machined into the joining surfaces. The assembly was TIG welded along all seams to be leak free. The hot side plenum is shown in Figure 5.5.

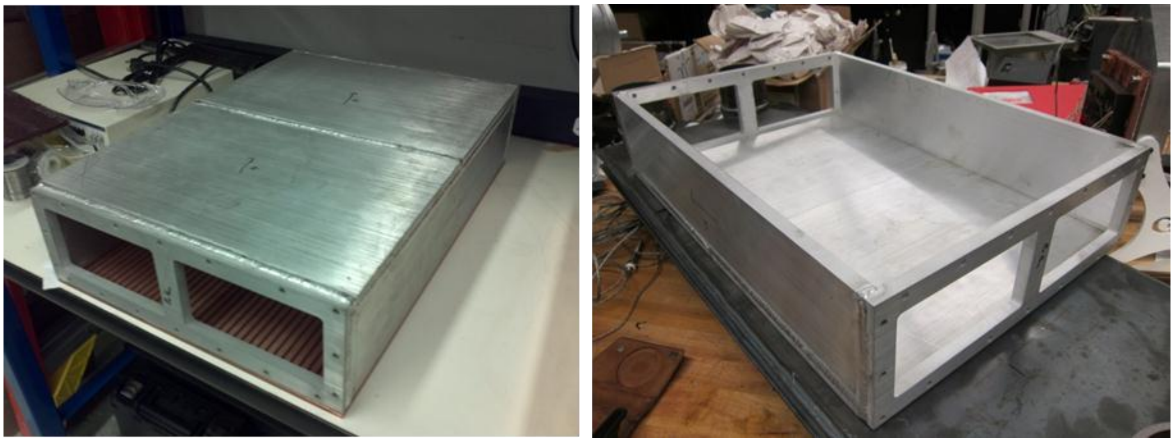

Figure 5.5 Hot side plenum

Commercially available 3” Schedule 40 steel pipe and weld-in fittings were used for all manifolds. Flanges were water-jet from 3/8” hot rolled steel plate. Fill and drain fittings were fabricated from soldered copper tubing and brass fittings.

Heater blocks were machined to simulate the spatial distribution and magnitude of the thermal load expected from the power electronics. Copper blocks were machined to match the device dimensions. Cartridge heaters were inserted into holes in the blocks and the heater blocks were potted in thermally insulating epoxy. The thickness of the epoxy ensured that 96% of the thermal load traveled through the exposed copper mounting surfaces. A heater simulating the 2x2 GeneSic array is pictured in Figure 5.6. The complete 2.5kW passive thermal management module with heaters is pictured in Figure 5.7.

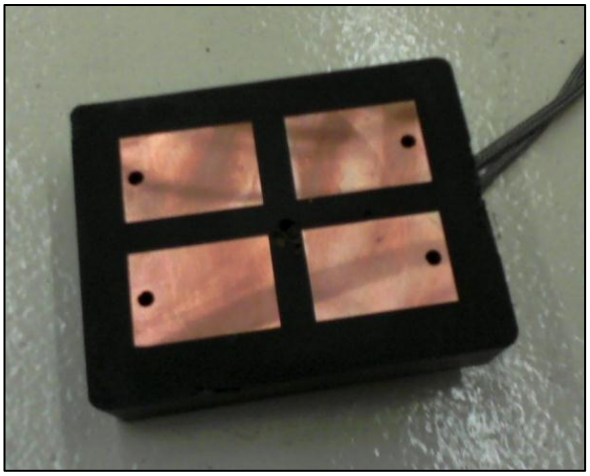

Figure 5.6 Heater block simulating thermal characteristics of four (4) GeneSic devices

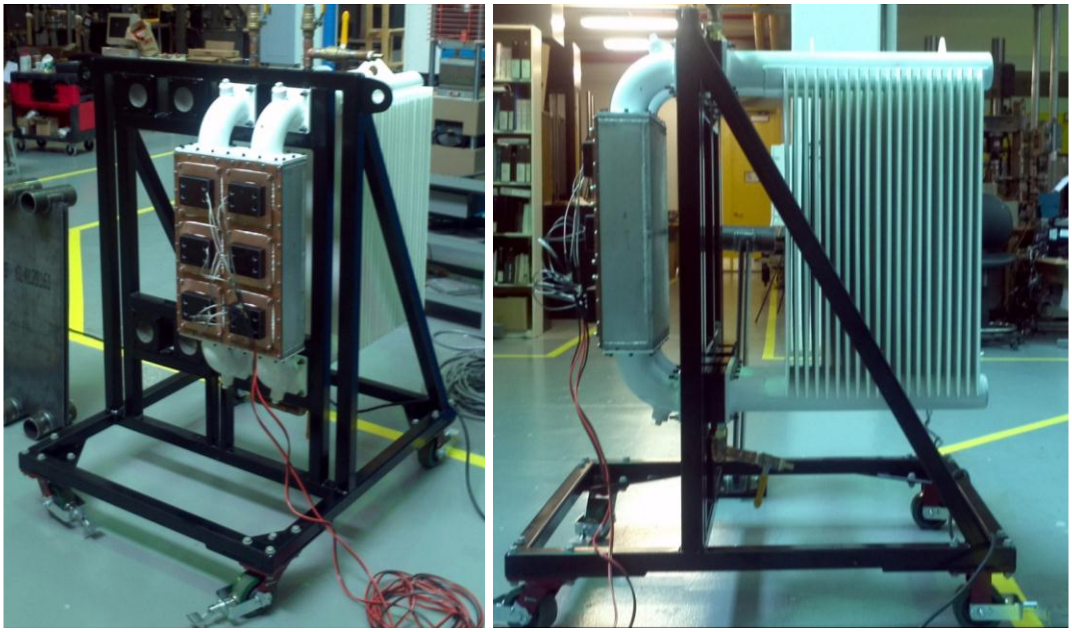

Figure 5.7 2.5kW Passive Thermal Management System (PTMS) Module

5.3.2 Elevated Ambient Testing Chamber

PTMS operation must be tested in ambient conditions up to 40 °C. An elevated ambient temperature chamber was designed to allow evaluation of thermal management system performance at temperatures between 30-40°C. Based on initial calculations, a heat pump (refrigeration cycle) controlled chamber would require similar volume and increased complexity compared to a mass-flow controlled chamber. The required mass flow rate of air was determined via the thermodynamic 1st law balance in Equation (5.1).

$$\dot{Q} = \dot{m} c_p \Delta T \tag{5.1}$$

For 5kW thermal load and 5° C change in air temperature (30°C chamber temperature – 25°C inlet air temperature), the mass flow rate of air, $\dot{m}$, must be roughly 1 kg/s. This represents a volumetric flow rate,$\dot{V}$, of 0.85 m^3/s.

To approximate ambient conditions, the ambient air velocity must be such that free convection dominates. The transition from free to forced convection occurs at a Reynolds^2 to Grashof ratio of roughly 1. To ensure minimal forced convection effects, the chamber will be designed to reduce this ratio to 0.1 as per Equations (5.2).

$$\frac{Re^2}{Gr} \leq 0.1 \ll 1 \tag{5.2}$$

$$Gr = \frac{g\beta\Delta T {L_{HX}}^3}{\nu^2} \tag{5.3}$$

$$Re = \frac{\rho v L_{chamber}}{\mu} \tag{5.4}$$

The above equations are solved to find the characteristic chamber length, $L_{chamber}$, necessary to satisfy the requirements of both the 1st law energy balance and free convection dominance. These calculations resulted in a minimum flow area of 15.3 m^2 , which is achievable by a 1.75 m (6 ft) square duct. This area dictates the minimum dimensions of the chamber. Based on the PTMS size and commercially available 8’ lengths of lumber, the chamber was designed to be an 8’ cube to facilitate fabrication, increase working volume, and add thermal load capacity. The chamber was designed to be easily disassembled for transportation or storage. A solid model of the elevated ambient testing chamber is illustrated in Figure 5.8.

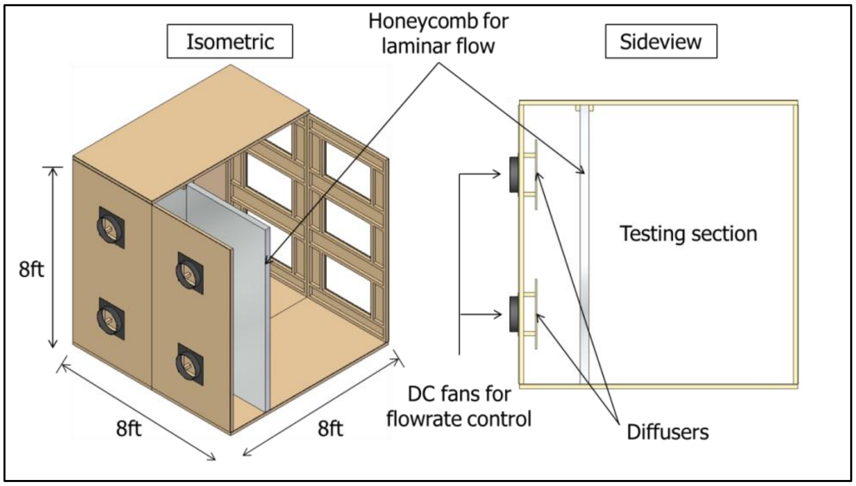

Figure 5.8 Elevated Ambient Testing Chamber Design

The chamber consists of ten individual panels (three wall panels, one door panel, two fan panels, two filter panels and two roof panel) to ease assembly and transportation. Each panel was constructed using a 2” by 2” frame supporting with a ¼”x4’x8’ sheet of plywood. Foam insulation board was glued to the inside of the panel to reduce the heat loss through the chamber walls. A plexi-glass door created the final wall of the chamber to allow viewing of and access to the test section. The above calculations assume that the airflow through the testing chamber is uniform throughout the flow cross section. The volumetric flow rate of 0.85 m^3/s is roughly equivalent to 1800 CFM. Four, 1250 CFM automotive radiator fans were selected to evenly distribute airflow in all quadrants and to allow a large range of possible flow rates.

A wall of honeycomb was place between the test section and the pusher fans to create laminar air flow into the test section. For the maximum anticipated flow rate of 0.85 m^3/s, the average flow velocity in the chamber would be 0.17 m/s. The honeycomb must have a hydraulic diameter and length such that fully developed laminar flow may develop while the air flows through the cells. The entry length for fully developed laminar flow as a function of hydraulic diameter at the anticipated flow velocity is plotted in Figure 5.9.

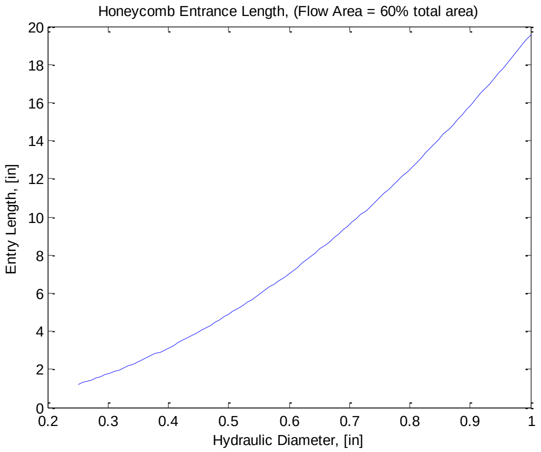

Figure 5.9 Fully developed laminar flow entry length

Commercially available 4” thick honeycomb panels with .25” width hexagonal cells were selected to ensure uniform laminar flow in the elevated ambient testing chamber.

Perforated diffuser panels were located immediately downstream of the fans to distribute the air flow across the entire honeycomb cross sectional area. Insulation board is fitted on the floor after the heat exchanger is placed within the chamber. The insulation is need because the concrete floor acts as a semi-infinite body heat sink and can contribute to temperature gradients in the chamber. Photographs of the complete testing chamber are illustrated in Figure 5.10.

Figure 5.10 Elevated ambient testing chamber

A digital proportional-derivative-integral (PID) controller was used to control fans to modulate the temperature within the testing chamber. Eight thermocouples placed at the eight corners of the testing volume were used to determine the average chamber temperature input for the control system. The PID controller considers the difference between the measured average chamber temperature and the user specified target temperature. Based on the proportional, derivative, and integral gains, an output voltage to the fan is determined. The four fans were wired in parallel to provide the same voltage to each fan. A list of the equipment used to operate the elevated ambient testing chamber is given in Table 5.2.

Table 5.2 Elevated ambient temperature chamber control equipment

Item	Quantity	Rating	Units
12” Electric Fan, 1250 CFM	4	0-14	Volts
800 Watt Power Supply	1	0-14	Volts
Space Heater	4	1.5	kW
NI® cDAQ-9174 System	1	-	-
T-Type Thermocouple	8	-	-
Laptop PC	1	-	-

The control system was created using LabView® software. The graphic user interface (GUI) for chamber temperature control can be seen in Figure 5.11.

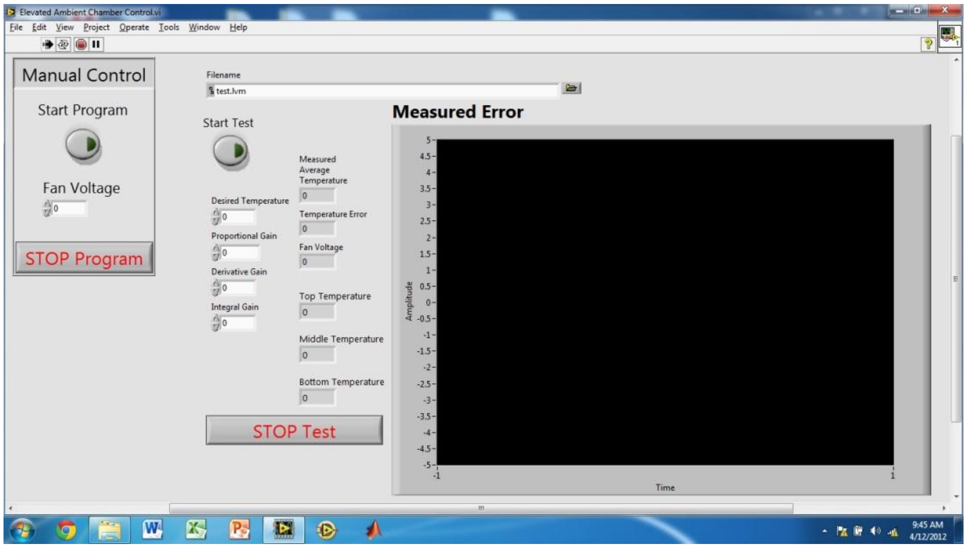

Fan Voltage: 0

Filename: test.lvm

Desired Temperature: 0

Proportional Gain: 0

Derivative Gain: 0

Integral Gain: 0

Measured Average Temperature: 0

Temperature Error: 0

Fan Voltage: 0

Top Temperature: 0

Middle Temperature: 0

Bottom Temperature: 0

Figure 5.11 Graphic User Interface for Testing Chamber Temperature Control

Preliminary testing results using space heaters at a nominal thermal input of 6 kW can be found in Figure 5.12. Data were collected over a period of twenty-six minutes and the desired chamber temperature was changed twice in the LabView® GUI during the test. The first ten minutes show performance for a desired temperature of 40 °C, followed by 5 minutes at 30 °C, and finally the remainder of the test at 25 °C desired temperature.

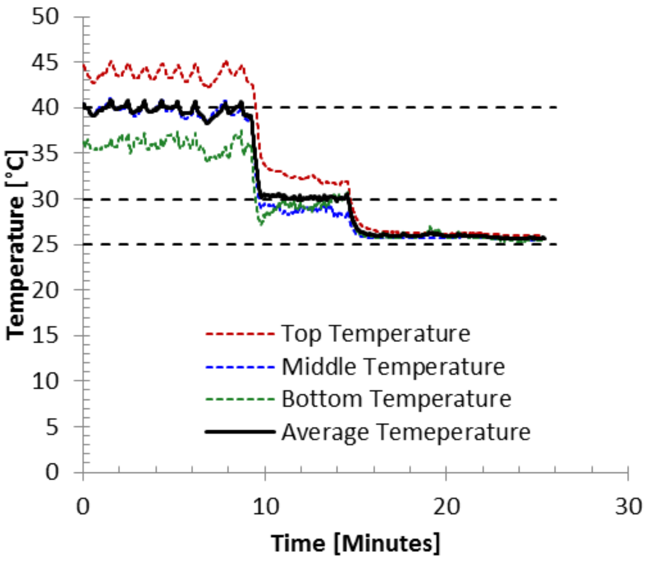

Figure 5.12 Average chamber temperatures during commissioning test

The roughly 10 °C temperature gradient between the upper and lower chamber temperatures at 40 °C is due to low flow rates allowing buoyancy effects to establish thermal gradients in the room. The thermal gradient decreases at lower chamber temperatures due to improved mixing associated with greater air flow rate through the chamber. The chamber's maximum temperature with no control is slightly above 40 °C. This makes system control at this set point more difficult because the relationship between air flow and fan voltage becomes non-linear as the fan motor dead zone voltage is approached. This is illustrated by examining the fan voltage in Figure 5.13.

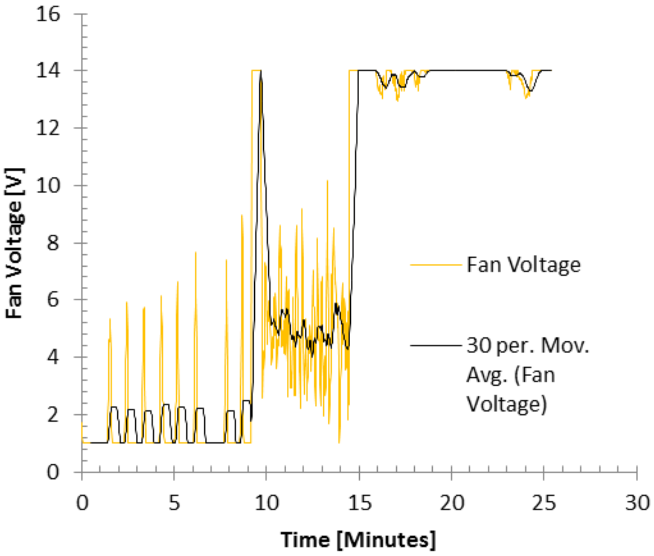

Figure 5.13 Fan voltage control

The data between zero and nominally ten minutes correlates to a desired temperature of 40 °C. The dead band voltage for the fans is 1 V. At this desired temperature, the fans cycle on and off to control the temperature. The large spike in voltage at ten minutes is due to the change in desired temperature from 40 to 30 °C. The voltage then tries to settle to a constant voltage (air flow rate) to maintain desired temperature. The shift at 15 minutes is the change from 30 °C to 25 °C. The minimum temperature in the chamber is limited to the temperature of the outside air being forced in by the fans. With the fans operating at the maximum voltage of 14V, the chamber temperature approached the external ambient temperature of approximately 25 °C.

5.3.3 Data collection

Thermal verification of the PTMS operation requires measuring air, surface, and fluid temperatures. Three forms of T-type thermocouples were used to take these measurements. Ambient air temperatures were measured using exposed bead T-type thermocouples. These thermocouples were located in planes equally above and below the

PTMS such that the average measured chamber temperature would be at the mid-plane of the PTMS. Fluid temperatures were measured using T-type probes inserted into thermowells in the PTMS manifolds. Surface temperature measurements, such as the device mounting temperatures, were measured using self-adhesive T-type surface thermocouples. The arrangement of the thermocouples in the chamber is illustrated in Figure 5.14 below. The device, fluid, and chamber positions represent two thermocouples, one on near devices, manifold, or chamber side, and the other on the far devices, manifold, or chamber side.

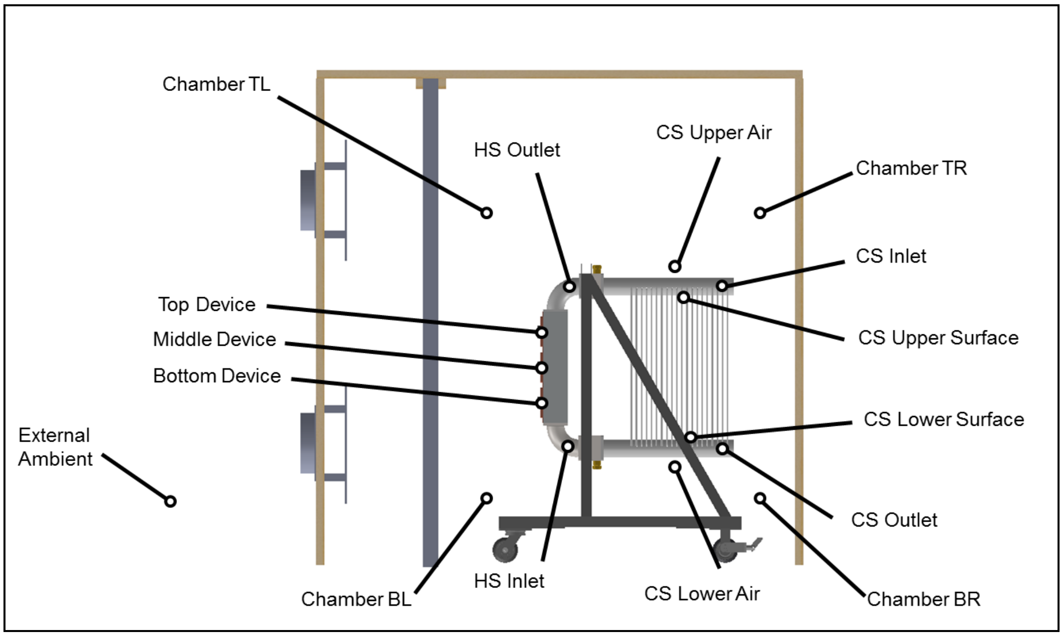

Figure 5.14 Elevated ambient testing chamber thermocouple placement

Thermocouples potentials were measured using two NI 9213 16 channel thermocouple DAQ modules with built in junction compensation. The channel assignments of the 27 thermocouples are listed in Table 5.3. Data logging was added to the LabView Chamber Control program, allowing PTMS testing via a single GUI.

Table 5.3 Thermocouple DAQ channel assignments

DAQ Module 1				DAQ Module 2			
	Channel	Name	Description	Channel	Name	Description	
	0	EA	External Ambient	0	TL	Top Left Device Plane	Device Mounting Temperatures
Chamber Temperatures	1	FTL	Chamber Far Top Left Corner	1	TR	Top Right Device Plane	
	2	FTR	Chamber Far Top Right Corner	2	ML	Middle Left Device Plane	
	3	FBL	Chamber Far Bottom Left Corner	3	MR	Middle Right Device Plane	
	4	FBR	Chamber Far Bottom Right Corner	4	BL	Bottom Left Device Plane	
	5	NTL	Chamber Near Top Left Corner	5	BR	Bottom Right Device Plane	
	6	NTR	Chamber Near Top Right Corner	6	N1	Near Loop Hot Side Inlet	Fluid Temperatures
	7	NBL	Chamber Near Bottom Left Corner	7	F1	Far Loop Hot Side Inlet	
	8	NBR	Chamber Near Bottom Right Corner	8	N2	Near Loop Hot Side Outlet	
	9			9	F2	Far Loop Hot Side Outlet	
Cold Side Temperatures	10	CSL	Cold Side Plate Lower Surface	10	N3	Near Loop Cold Side Inlet	
	11	CSU	Cold Side Plate Upper Surface	11	F3	Far Loop Cold Side Inlet	
	12	CS_in	Cold Side Air Inlet	12	N4	Near Loop Cold Side Outlet	
	13	CS_out	Cold Side Air Outlet	13	F4	Near Loop Cold Side Outlet	
	14			14			
	15			15			

Acronyms are used to identify the individual measurements. Chamber locations are specified by three letters indicating their location as viewed in Figure 5.14. In order, the letters indicated the location in the near or far side of the chamber, the location in the top or bottom plane, and the location on the left or right side of the chamber. Fluid temperature short hand indicates the location in either the far or near manifold and the number of the node in the same convention used in Chapter 3. Device temperatures are indicated by the firs letter to be top, middle, or bottom and by the second letter to be on either the left or right when viewed from normal to the hot side baseplate. Some of the measurement locations are illustrated in Figure 5.15.

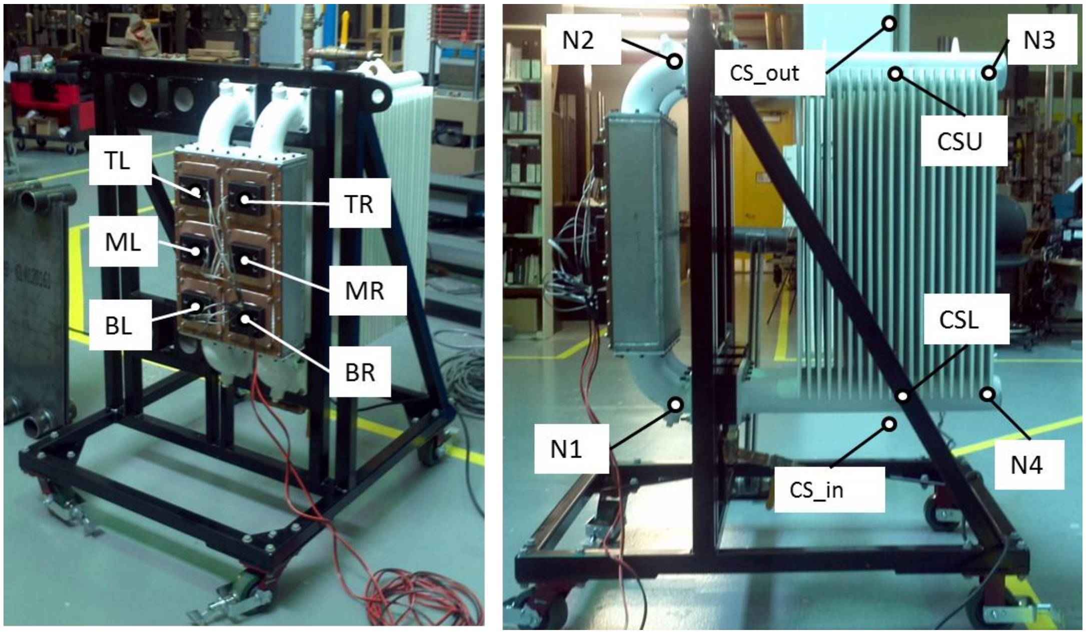

Figure 5.15 Temperature measurement locations

The make and model of relevant apparatus and their associated uncertainties are given in Table 5.5. These uncertainties are used in the analysis to determine the uncertainty of the experimental results.

Table 5.4 Apparatus and uncertainty

Apparatus	Model	Uncertainty
Surface Thermocouple	Omega T-type	1.0 °C
Exposed Bead Thermocouple	Omega T-type	1.0 °C
NPT Thermocouple Probe	Omega T-type	1.0 °C
Digital Voltmeter	Fluke Model 117	1.0% + 3 counts
Digital Ohmmeter	Fluke Model 117	0.9% + 2 counts
Digital Ammeter	Staco 3PN2210B-DAM	1.0% + 2 counts
Variac	Staco 3PN2210B	n/a
16 Ch. Thermocouple DAQ	NI 9213	n/a

5.4 Methodology

Five independent trials were conducted in the elevated ambient testing chamber. The thermosiphon was tested three times at the design target of 2.5kW and 40 °C. Additional tests were conducted at target thermal load and ambient temperatures of 35 °C and 30C. During each test, the chamber was initially at the same temperature as the surrounding room. The thermal load to the PTMS was turned on after data recording was initiated. Thermal load was calculated by multiplying the supply current, as measured by the variac ammeter, by the heater voltage, measured using the voltmeter. This method reduced the experimental uncertainty of the thermal load by eliminating the V^2 term in the Kline McClintock calculations. The chamber temperature was allowed to rise as the PTMS heated up. Upon reaching the chamber temperature set point, the PID controller operated the fans to maintain the average chamber temperature at the desired value. Tests were run for approximately 7 hours to ensure significant data capture at steady state, as determined from preliminary trials.

5.5 Experimental results

Temperature measurements were recorded at 1Hertz by the LabView® software and National Instruments® DAQ system. The following plots will display the data collected for the June 18, 2012 test of 2500 W thermal load and 40C ambient temperature. These data are characteristic of the data collected in all five trials. The air temperatures measured by the exposed bead thermocouples are plotted in Figure 5.16. The values in the plot legend reference the channel names in Table 5.3 The bottom most data set is the temperature of the air entering the chamber via the fans. The HVAC system of the building cycles on and off to control the building temperature and this can be seen in the plot. Some of this cyclic behavior propagates into the chamber temperatures and operation. The thermal gradient between the lower chamber measurements and the upper chamber measurements is also visible. The chamber temperature data indicate that the average ambient temperature in the chamber remained within 1 °C of the 40 °C desired temperature.

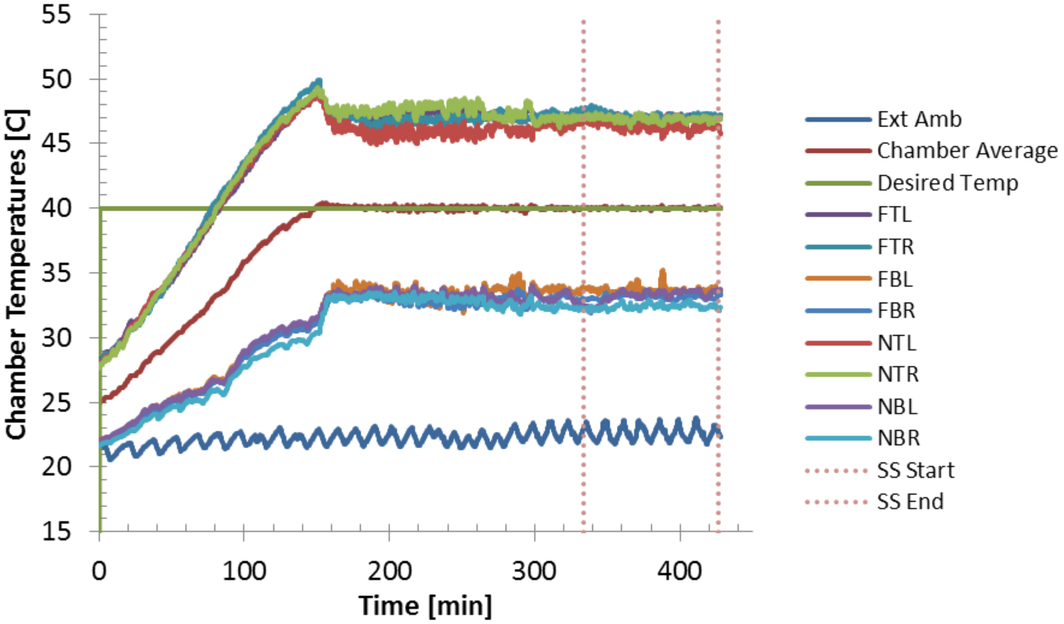

Figure 5.16 Testing Chamber temperatures, 40C desired temperature

The device mounting temperatures were measured using surface thermocouples located on the interface between the heaters and the device mounting plates. The temperatures measured behind each of the six heater blocks are plotted in Figure 5.17. The beginning and end of the steady state period are marked on the plot as well. The determination of steady state was accomplished by examining the rate of change of device temperatures over each data collection time step. A 50-point moving average was fit to the device mounting temperature change data, shown in Figure 5.18. Steady state was identified as the time during which the moving average oscillated about zero.

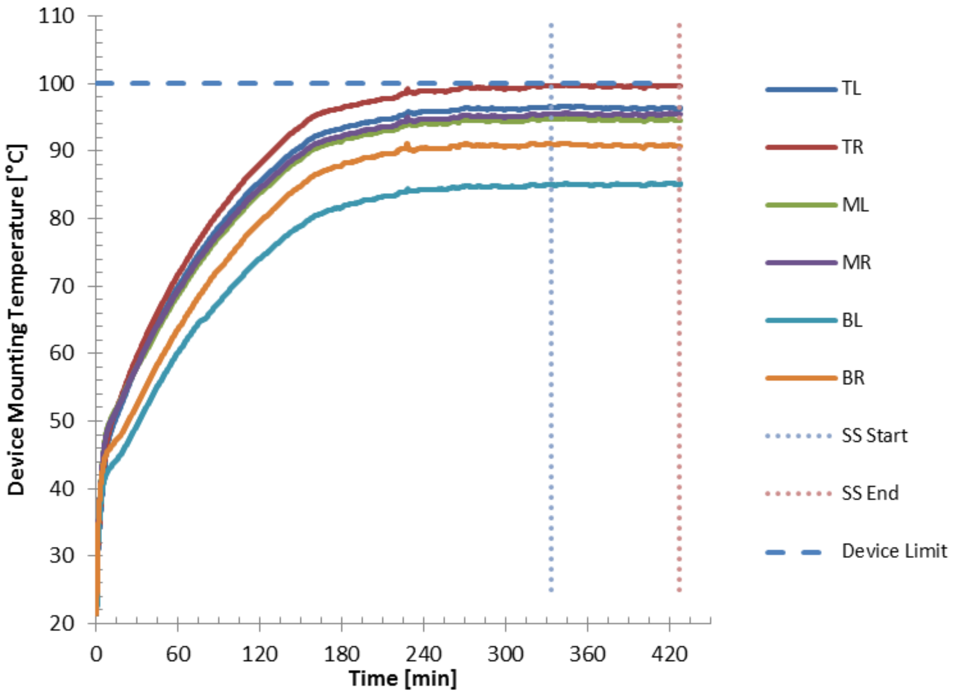

Figure 5.17 Device mounting temperatures for 2.5kW and 40C ambient

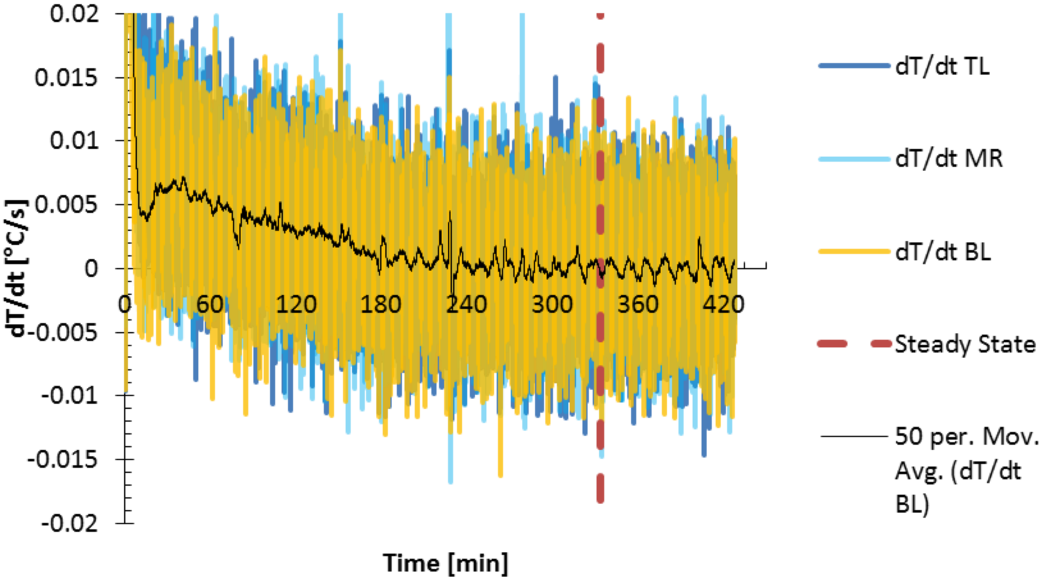

Figure 5.18 Determination of steady state via 50-pt moving average of device temperature change

Thermowells installed in the thermosiphon manifolds allowed the fluid temperature thermocouple probes to be inserted into the fluid. The thermowells were fitted into NPT bungs welded into both the near and far manifolds at the inlets and outlets of the hot side and cold side. In total, eight fluid temperature measurements were taken with one located at each node in both manifolds. The fluid temperatures recorded are plotted in Figure 5.19. Point 1 is located at the hot side inlet, 2 at the hot side outlet, 3 at the cold side inlet, and 4 at the cold side outlet.

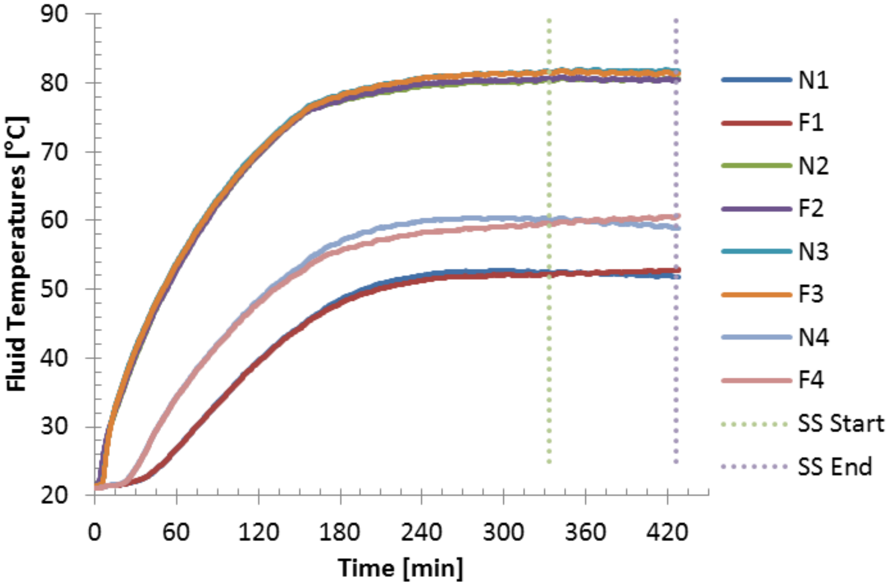

Figure 5.19 Fluid Temperatures during 2.5kW thermal load and 40C ambient

5.6 Analysis

The date collected during the thermosiphon trials are evaluated to validate system performance and allow verification of the multi-physics model predictions. Device mounting temperatures, fluid temperatures, and total system thermal resistance are compared.

5.6.1 Uncertainty analysis

Measurement uncertainty analysis was performed using Kline and McClintock's method for single sample experiments [69]. Thermal load to the system was determined using the built in ammeter on the variac, and a handheld voltmeter to measure the voltage drop across the heater circuit. The power measurements were taken during the steady state period. The calculated thermal loads, P, and associated uncertainties, σP, are compiled in Table 5.5.

Table 5.5 Thermal Load Uncertainty Anlaysis

Test	Date	P_{Target} [W]	T_{Target} [°C]	Voltage [V]	σV [V]	I [A]	σI [A]	P [W]	σP [W]
1	1-Jun	2500	30	112.0	1.42	22.3	0.523	2498	9.50
2	6-Jun	2500	40	113.2	1.43	22.4	0.524	2536	9.56
3	7-Jun	2500	35	113.3	1.43	22.4	0.524	2538	9.56
4	13-Jun	2500	40	113.3	1.43	22.35	0.524	2532	9.56
5	18-Jun	2500	40	112.6	1.43	22.2	0.522	2500	9.51

The results of the five trials are given in Table 5.6. The thermal loads are as calculated in Table 5.5, and the maximum device temperatures are the steady state average of the top device (TL and TR) measurements during the steady state period. The thermal resistance is calculated by subtracting the ambient temperature from the maximum device temperature and dividing by the thermal load as in Equation (5.5).

$$R_{thermal} = \frac{T_{Device} - T_{Ambient}}{P_{thermal}} \tag{5.5}$$

Table 5.6 Steady state thermal load, maximum device temperataure, and sytem thermal resistance and associated uncertainties

Trial Number	Ambient Temperature [°C]	Thermal Load [W]	σP [W]	Max Device Temp [°C]	σT_{device} [°C]	Thermal Resistance [°C/W]	$\sigma R_{thermal}$ [°C/W]
1	30.0	2498	9.50	87.8	1.0	.02312	0.000573
2	40.0	2536	9.56	98.4	1.0	.02304	0.000564
3	35.0	2538	9.56	93.5	1.0	.02304	0.000564
4	40.0	2532	9.56	98.5	1.0	.02310	0.000565
5	40.0	2500	9.51	98.0	1.0	.02322	0.000573

The maximum steady state device temperatures and uncertainties of the five trials are plotted in Figure 5.20. All tests maintained device mounting temperatures below the 100 °C limit. At 2500 W thermal load and 40 °C ambient temperature a maximum steady state device mounting temperature of 98.0 °C was recorded, corresponding to a baseplate thermal resistance of .0232 °C/W.

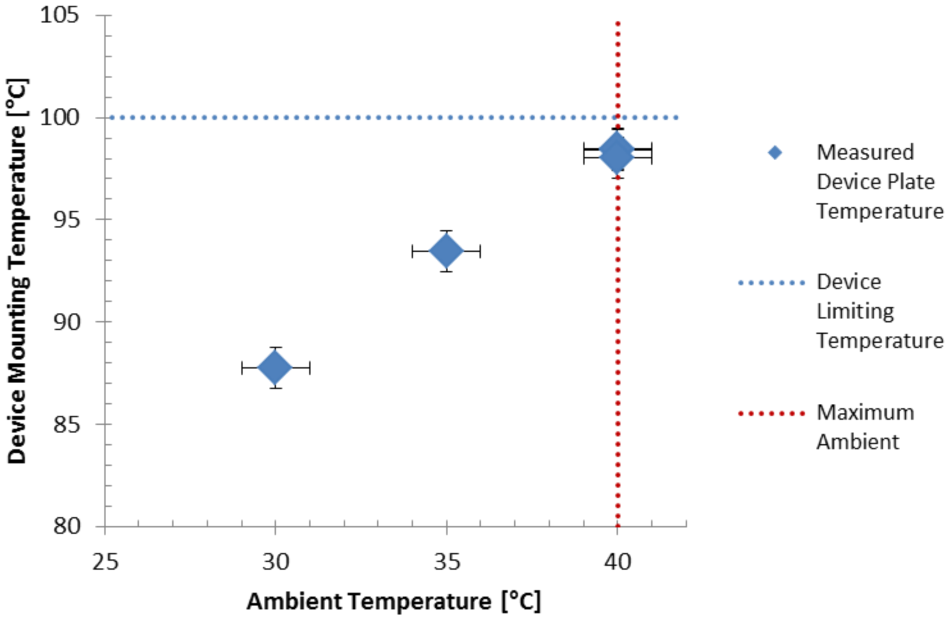

Figure 5.20 Steady state temperature measurements and uncertainties

The maximum steady state device mounting temperatures are plotted in Figure 5.21 along with a curve of the model prediction. These steady state values were calculated from the average of several thousand temperature measurements taken over the steady state periods. The measurement uncertainties of the thermocouples are used to indicate the expected range of actual ambient and device temperature.

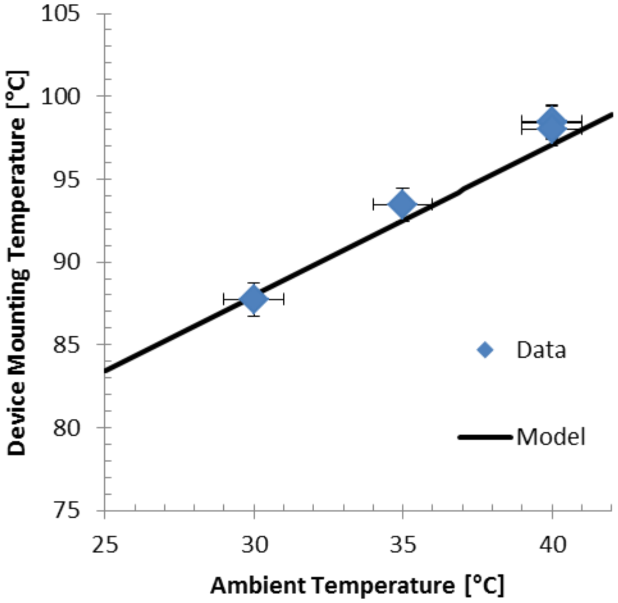

Figure 5.21 Device Mounting temperature data comparison with model

The PTMS thermal resistances calculated previously are plotted in Figure 5.22 along with the model prediction. The thermal resistance uncertainty is obtained from single point measurement uncertainty of the thermal load, presented in Table 5.5, and the thermocouple uncertainty, given in Table 5.4. The thermal resistance model prediction fell within the uncertainty of all data points, though the data do not appear to follow the downward trend with respect to increasing ambient temperature.

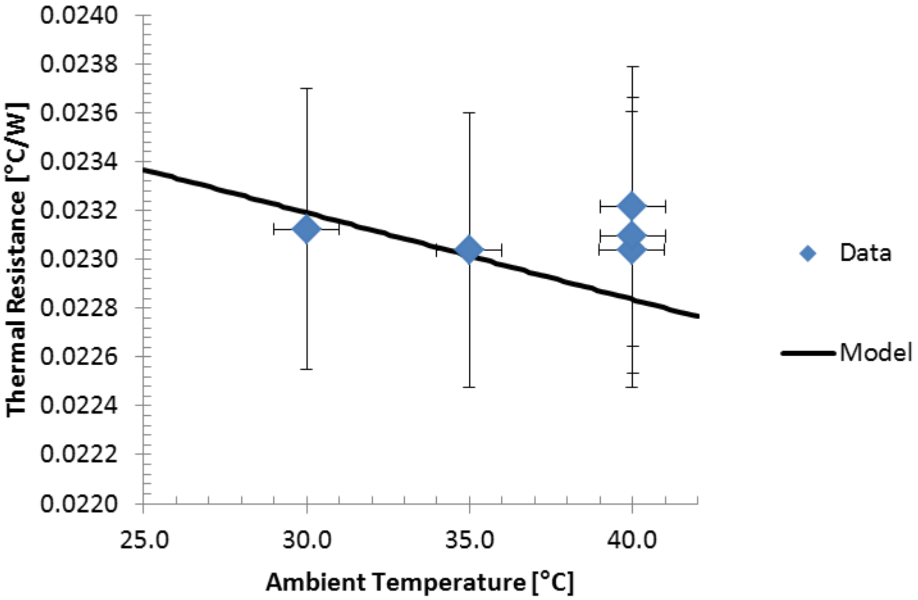

Figure 5.22 PTMS thermal resistance comparison with model

The steady state measurements and model predictions are compared in Table 5.7. The temperature predictions are within 1.1 °C of experimental values. The predicted thermal resistance is within 2% of experimental.

Table 5.7 Comparison of experimental and predicted device temperature and PTMS thermal resistance

Test	Date	$P_{thermal}$ [W]	$T_{ambient}$ [C]	T_{upper} [C]	T_{model} [C]	Delta [C]	R_{therm} [C/W]	R_{model} [C/W]	%
1	1-Jun	2498	30	87.8	87.8	0.088	0.0231	0.0232	0.15
2	6-Jun	2536	40	98.4	97.4	-1.006	0.0230	0.0227	1.28
3	7-Jun	2538	35	93.5	93.1	-0.360	0.0230	0.0229	0.62
4	13-Jun	2532	40	98.5	97.6	-0.933	0.0231	0.0227	1.60
5	18-Jun	2500	40	98.0	97.0	-1.059	0.0232	0.0228	1.82

5.6.2 Cold Side Performance Analysis

Exposed bead thermocouples located immediately above and below the cold side ambient rejection array allow measurement of the air temperature as it enters and exits the vertical channels. The model assumes an isoflux condition because the temperature of the sinking heat transfer fluid internal to the plates is decreasing top to bottom while the temperature of the rising air between the plates is increasing bottom to top. Surface thermocouples placed at the ends of the cold side plates allow comparison of the temperature differential between the surface and air at the entry and exit. A plot of these four measurements is shown in Figure 5.23.

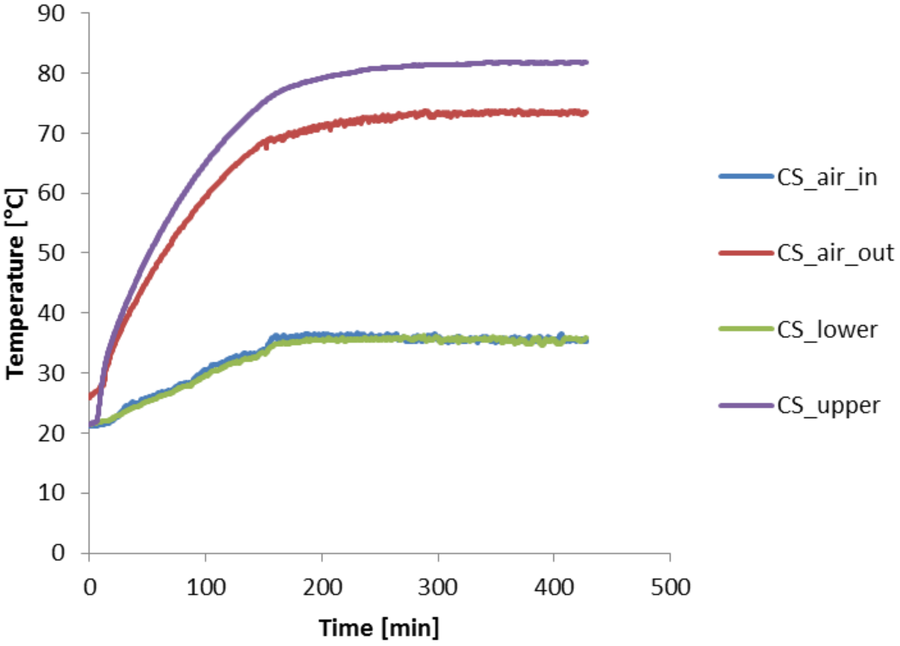

Figure 5.23 Cold side surface and air temperatures

The plot shows that the temperature rise in the air is approximately 35 °C while the surface temperature drop in the cold side is approximately 45 °C. A linear interpolation of these measurements, plotted in Figure 5.24, shows a temperature gradient between surface and air more consistent with an isoflux condition than an isothermal condition. This validates the isoflux assumption used in predicting heat transfer coefficients internal to the ambient rejection array plate gaps.

A log mean temperature difference (LMTD) approach requires modeling of the airflow through plates such that the cold side rejection array can be modeled as a counter-flow heat exchanger. The vertical parallel isoflux plate correlation is used to simplify the system of equations.

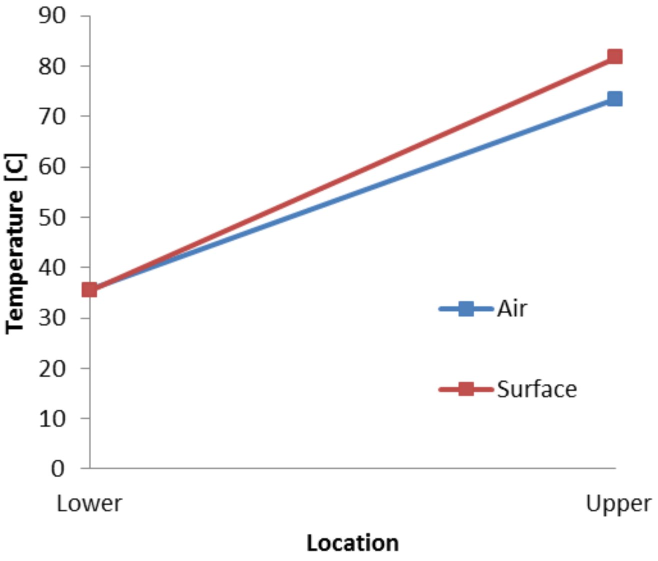

Figure 5.24 Isoflux behavior of cold side

The effective overall heat transfer coefficient, *U*, of the ambient rejection surfaces may be estimated using the measured surface temperatures, surface areas, and heat input, as in Equation (5.6).

$$Q = UA\Delta T \tag{5.6}$$

The temperature difference between the rejection array and ambient, ΔT, is taken to be the difference between the average cold side surface temperature and average chamber temperature. The estimated overall heat transfer coefficient for each trial is listed in Table 5.8. These values are consistent with model predictions and expectations for free convection.

Table 5.8 Overall ambient heat transfer coefficient

Trial	Q_{in} [W]	$Q_{HS,loss}$ [W]	Q_{reject} [W]	A_{reject} [m^2]	$T_{CS,in}$ [°C]	$T_{CS,out}$ [°C]	T_{CS} [°C]	T_{amb} [°C]	ΔT [°C]	$U_{predicted}$ [W/m^2°C]
1	2498	74.3	2423.7	12.25	70.8	48.5	59.7	30	29.65	6.67
2	2536	75.3	2460.7	12.25	81.2	58.9	70.1	40	30.05	6.68
3	2538	75.3	2462.7	12.25	76.6	53.4	65.0	35	30	6.70
4	2532	75.2	2456.8	12.25	81.6	59.4	70.5	40	30.5	6.58
5	2500	74.3	2425.7	12.25	81.5	59.8	70.7	40	30.65	6.46

5.7 Fluid temperature investigation

Overall system performance closely followed that predicted by the model. Device mounting temperatures predictions were within approximately 1°C and the thermal resistance of the system was predicted within 2%. This parity between the model and experiment is unusual in the study of heat transfer and warrants further investigation. This section will investigate the fluid temperatures in the thermosiphon loop.

The fluid temperatures predicted and measured at the four nodes are presented in Table 5.9 for comparison. The average temperatures in each section of the thermosiphon, as determined by the mean of the inlet and outlet temperatures are also included.

Table 5.9 Comparison of experimental fluid temperatures with model predictions

	T_{Device} [°C]	T_1 [°C]	T_{HS} [°C]	T_2 [°C]	T_{UM} [°C]	T_3 [°C]	T_{CS} [°C]	T_4 [°C]	T_{LM} [°C]	m [kg/s]
Data	98	52	66	80	80.5	81	70	59	56	.045
Model	95	81	83.5	86	86	86	83.5	81	81	.24
Delta	3	29	17.5	6	5.5	5	13.5	22	25	.195

Large fluid temperature discrepancies ranging from 5 to 29 degrees are revealed. The mass flow rate of the experimental PTMS can be estimated via a first law energy balance on the hot side using the known thermal load, temperature rise, and fluid specific heat. The model predicts a circulation rate 430% greater than estimated for the real system.

The agreement of the device mounting temperatures may be attributed to the use of average temperatures and convection coefficients in the model. The model predicts a higher average cold side (CS) temperature, which would lead to greater performance. However, this effect is offset by the higher hot side (HS) temperature, resulting in diminished hot side performance. The first law energy balance and coupled nature of the system mitigate the effects of improper flow rate prediction. If the flow rate is over-predicted, the fluid temperature must be greater and the cold side will have a lower thermal resistance. In this fashion, the predicted total thermal resistance of the PTMS may be a realistic value despite using a flawed circulation rate prediction.

5.7.1 Low Reynolds flow model

The experimental data indicate a severe over-prediction of heat transfer fluid flow rate. This is evidenced by comparing the 28°C experimental fluid temperature rise through the hot side to the 5 °C temperature rise predicted by the model. A re-evaluation of the fluid dynamic flow balance is performed to address the disagreement between model and experiment.

Initial model development was done without prior examination of real world thermosiphon operation. Conventional textbook pipe flow loss correlations were used to describe the major and minor losses in the flow loop. From the predicted flow rate of 0.045 kg/s, average predicted Reynolds numbers are approximately 2 for the hot side flow channels and 50 for the upper manifold. Pipe flow correlations assume Re>>1 such that inertial effects dominate, as evidenced by the Reynolds number equation (5.7).

$$\mathrm{Re} = \frac{\rho V D}{\mu} = \frac{inertial}{viscous} \tag{5.7}$$

At low Reynolds numbers, the viscous effects ignored in conventional internal flow correlations dominate. Both major and minor losses must now be considered especially for the low Reynolds flow regime. Viscous boundary layer development in the entry region of each section must also be considered, as the thermal boundary layer development was considered in calculating average Nusselt numbers in Chapter 3.

A review of literature on low-Reynolds flow losses identified correlations for predicting pressure loss through the various sections of the thermosiphon. Losses in the circular manifold sections were calculated using correlations from Langhaar [72] for steady flow in a straight tube, including entry region effects. The resulting correlation for the straight circular sections is given in Equation (5.8)

$$\Delta P_{loss} = \frac{32 \mu V L}{D^2} + \frac{2.28 \rho V^2}{2} \tag{5.8}$$

The hot side and cold side channels were considered as rectangular channels as in Han's paper on hydrodynamic entrance lengths for laminar flow in rectangular ducts [73]. Polynomial curves were fit to tabular data in the paper to allow prediction of the hydrodynamic entrance length via Equations (5.9) and (5.10).

$$\Phi = -0.0946\left(\frac{a}{b}\right)^2 + 0.01595\left(\frac{a}{b}\right) + 0.0093 \tag{5.9}$$

$$L_{entry} = \Phi D_H \,\mathrm{Re} \tag{5.10}$$

Two additional constants were determined from Han's tabular data to determine the pressure drop across a given length, L, of rectangular channel. The C term in Equation

(5.11) is a traditional loss coefficient. The value *K*, given in Equation (5.12), is a correction term used in Equation (5.13) to account for the hydrodynamic entrance length.

$$C = 57.197\left(\frac{a}{b}\right)^2 - 93.856\left(\frac{a}{b}\right) + 94.466 \tag{5.11}$$

$$K = -1.50\left(\frac{a}{b}\right)^2 + 2.679\left(\frac{a}{b}\right) + 1.839 \tag{5.12}$$

$$\Delta P_{loss} = \frac{\rho V^2}{2}\left(\frac{C}{\mathrm{Re}}\frac{L}{D_H} + K\right) \tag{5.13}$$

The so-called minor losses occurring at changes in flow cross section are expected to be significant in the low Reynolds regime. Kays performed a study in 1950 on the pressure loss in abrupt changes in cross section at low Reynolds numbers [74]. The work examined flow into and out of single and multiple tube systems of circular, square, and rectangular channels. This arrangement is analogous to the flow expansion from the lower manifolds into the plenum cavity, and the contraction from the cavity into the hot side channels created by the fin array. It also captures the opposite transitions from the channels to the plenum and then into the upper manifolds. Kays graphically presents loss coefficients as a function of the area ratio across the flow transition for a range of Reynolds numbers. The thermosiphon model will incorporate polynomial curve fits to data taken from the laminar plots for the appropriate expansions and contractions. The area ratio, σ, is calculated using Equation (5.14).

$$\sigma = \frac{A_{small}}{A_{large}} \tag{5.14}$$

The loss coefficient, *K*, for the expansion from lower manifold into plenum is given Equation (5.15). The contraction from the plenum into the rectangular hot side flow channels is given by Equation (5.16). The expansion from the top of the hot side channels into the upper plenum is calculated using Equation (5.17), and the contraction from the plenum into the upper manifolds is given by Equation (5.18).

$$K_{\exp,round} = 1.04\sigma^2 - 2.71\sigma + 1 \tag{5.15}$$

$$K_{cont,rect} = -0.383\sigma^2 - 0.024\sigma + 1.20 \tag{5.16}$$

$$K_{\exp,rect} = 0.988\sigma^2 - 2.77\sigma + 1 \tag{5.17}$$

$$K_{cont,round} = -0.409\sigma + 1.08 \tag{5.18}$$

The loss coefficients are included in Equation (5.19) to determine the predicted pressure loss for each transition.

$$\Delta P_{loss} = K_{loss}\rho\frac{V^2}{2} \tag{5.19}$$

The fluid dynamic changes were implemented in the model, and the model was run for the existing geometries, 2.5kW thermal load, and 40 C ambient. The experimental temperatures and flow rate are presented in Table 5.10 in the center column. The predictions of the original model and the deviation from experiment are given in the left columns. The updated model predictions and differences are in the right columns.

Table 5.10 Model predictions for 2.5kW thermal load and 40C ambient temperature

Measurement	Original Model		Testing Data	Updated Model	
	Delta	Prediction		Prediction	Delta
T_{Device} [°C]	3	95	98	93	5
T_1 [°C]	29	81	52	60	8
T_{HS} [°C]	17.5	83.5	66	71	5
T_2 [°C]	6	86	80	82	2
T_{UM} [°C]	5.5	86	80.5	82	1.5
T_3 [°C]	5	86	81	81	0
T_{CS} [°C]	13.5	83.5	70	71	1
T_4 [°C]	22	81	59	61	2
T_{LM} [°C]	25	81	56	61	5
$\dot{m}$ [kg/s]	0.195	0.24	0.045	0.055	0.01

5.8 Discussion

In the original model, fluid temperature deviations up to 29 °C, and a mass flow rate error of over 430% are seen. The updated model reduces the fluid temperature deviations to 8 °C, and the mass flow rate error to 22%. The fluid temperature predictions are improved significantly with the updated model, but the device mounting temperature differs from the data by a slightly larger amount. The experimental data show a temperature drop of 18 °C from the device mounting plate to the hot side outlet temperature (T2). The model predicts a drop of 11 °C, indicating that the thermal resistances between the device and the fluid may need modification. The conduction losses in the copper spreader plate and fin array are well described. The contact resistance of the interface between the spreader plate and fin array is not well characterized. The thermal paste used in these interfaces is rated for a contact resistance of 7e-6 °C/W-m^2 for a compressive force of 100 kN/m^2. While this force is applied by correctly torqueing the mounting bolts, the deflection of the device plate cannot be prevented. Uncertainties in the surface finish and flatness of the mating surfaces and the presence of any oxide layers further prevent exact prediction of the contact resistance. For its current usage, a safety margin of 5-10 °C should be used in designing thermal management systems.

A sensitivity study was performed on the updated model. It was expected that the coupled nature of the system would change with the new dominance of viscous effects on the fluid circulation. It was found that the hot side internal convection coefficient had a small impact on system thermal resistance and an indiscernible impact on mass flow rate. Cold side internal convection coefficient had negligible impact on system thermal resistance and small impact on fluid circulation rate. Variations in flow losses resulted in significant changes in system thermal resistance and fluid mass flow rate. The cold side outlet temperature, T_4, is also evaluated. It is seen to correlate with the mass flow rate as they remain constant or change together at the variation of other parameters. These results are presented in Table 5.11.

Table 5.11 Updated model sensitivity study

Δ h_{HS}	**-10%**	**-5%**	**-2%**	**Model**	**+2%**	**+5%**	**+10%**
T_{device} [°C]	93.4	93.0	92.8	**92.6**	92.5	92.3	92.0
T_4 [°C]	61.2	61.2	61.2	61.2	61.2	61.3	61.3
$\dot{m}$ [kg/s]	.0561	.0561	.0561	.0561	.0561	.0561	.0561
$R_{Baseplate}$ [°C/W]	.0214	.0212	.2011	**.0211**	.0210	.0209	.0208
Δ $R_{baseplate}$ [%]	1.4	.47	-	**-**	-.47	-.95	-1.4
Δ h_{CS}	**-10%**	**-5%**	**-2%**	**Model**	**+2%**	**+5%**	**+10%**
T_{device} [°C]	92.8	92.7	92.7	**92.6**	92.6	92.6	92.5
T_4 [°C]	61.54	61.4	61.3	**61.2**	61.2	61.1	61.0
$\dot{m}$ [kg/s]	.0564	.0563	.0562	**.0561**	.0561	.0560	.0559
$R_{Baseplate}$ [°C/W]	.0211	.0211	.0211	**.0211**	.0210	.0210	.0210
Δ $R_{baseplate}$ [%]	-	-	-	**-**	-.47	-.47	-.47
Δ P_{loss}	**-10%**	**-5%**	**-2%**	**Model**	**+2%**	**+5%**	**+10%**
T_{device} [°C]	92.0	92.3	92.5	**92.6**	92.8	92.9	93.2
T_4 [°C]	61.6	61.4	61.3	**61.2**	61.2	61.0	60.9
$\dot{m}$ [kg/s]	.0588	.0574	.0566	**.0561**	.0556	.0549	.0538
$R_{Baseplate}$ [°C/W]	.0208	.0209	.0210	**.0211**	.0211	.0212	.0213
Δ $R_{baseplate}$ [%]	1.4	.95	.47	**-**	-	-.47	-.95

The sensitivity study shows that the hot side convection coefficient and pressure loss predictions have the largest impact on system performance while the pressure loss has the greatest impact on cold side outlet fluid temperature. This exercise also illustrates the way in which one part of the model can affect predicted fluid temperatures significantly while having minimal effect on total system performance prediction. Combining this behavior with the required overall energy balance requirement, the initial model provided good bulk system performance predictions even while poorly predicting the fluid circulation rate. The corrected model provides improved accuracy on prediction of the fluid temperatures with a minor reduction in surface temperature prediction accuracy.

5.8.1 Extended Cold Side Length

The ratio of hot side heated length to cold side cooled length also presents issues for the original model. The original model assumes that the fluid density changes through the manifolds are negligible and that the density changes across the hot and cold sides are equal. In reality, the density change of the fluid occurs over short vertical length in the hot side, and then over longer horizontal manifolds and vertical rejection array lengths. Two additional nodes were added to the fluid model and the Bernoulli streamline equation was used to account for density changes and gravitational potentials simultaneously. The vertical lengths of manifold on the thermosiphon hot side should be insulated to minimize fluid density increases that would be detrimental to the natural circulation. These lengths will be assumed adiabatic in the model. The flow losses calculated above are included in the node to node Bernoulli analysis. The new thermosiphon schematic is depicted in Figure 5.25, including the adiabatic assumption for the vertical manifold lengths above and below the hot side.

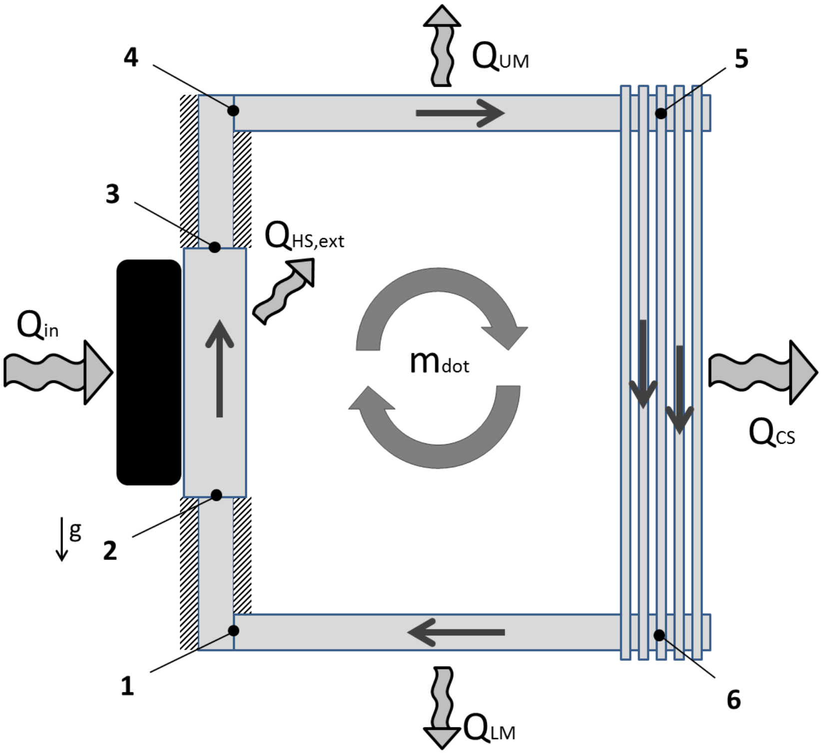

Figure 5.25 Updated 6 node thermosiphon schematic

The basic Bernoulli streamline equation is given in Equation (5.20). Integrating between two points, and including losses due to non-conservative forces results in Equation (5.21).

$$\int \frac{dp}{\rho} + \frac{V^2}{2} + gz = \text{constant} \tag{5.20}$$

$$P_1 + \frac{\rho_1 V_1^2}{2} + \rho_1 g z_1 = P_2 + \frac{\rho_2 V_2^2}{2} + \rho_2 g z_2 + \Delta P_{loss} \tag{5.21}$$

Rearranging Equation (5.21) to isolate the pressure change between points 1 and 2 give Equation (5.22). This equation is applied across each section using the fluid properties and heights at the nodes bounding the section.

$$\Delta P_{1-2}=\left(\frac{\rho_1 V_1^2}{2}-\frac{\rho_2 V_2^2}{2}\right)+\left(\rho_1 g z_1-\rho_2 g z_2\right)-\Delta P_{loss} \tag{5.22}$$

5.9 Conclusion

A passive thermal management system (PTMS) was designed and built to the dimensions selected by the multi-physics design optimization (MDO) presented in Chapter 4. The PTMS was tested at the rated thermal load of 2.5kW and ambient conditions of 30 °C, 35 °C, and 40 °C in the elevated ambient testing chamber. The system was allowed to reach steady state operation, and steady state device, fluid, surface, and chamber temperatures were recorded. The maximum device mounting temperature was 98 °C, below the device limit of 100°C. The PTMS is suitable for cooling of the IDCL PCAT power electronics.

Initial evaluation of the data showed device temperature predictions are within 1.1 °C of experimental values and predicted thermal resistance within 2% of experimental values across all 5 trials. Further analysis revealed significant fluid temperature discrepancies ranging from 5 to 29 °C. The mass flow rate of the experimental PTMS was estimated via a first law energy balance to be significantly smaller than predicted by the model. It was found that the fluid flow in the experimental thermosiphon is at low Reynolds numbers well below the valid range of conventional pipe flow correlations used in the original model. An updated model is developed to address fluid dynamic behavior in the low Reynolds regime. The updated model reduces flow rate disagreement between the model and the data from 500% to 20% and maximum fluid temperature disagreement from 29 °C to 8 °C.

The successful implementation of an analytical multi-physics thermosiphon model into a rapid design sizing optimization is shown. The validation study shows agreement between the aggregate performance of the PTMS and the prediction of the multi-physics model. Scrutiny of the fluid temperature profiles reveals an incorrect assumption in the fluid dynamic model. The presence of low Reynolds regime flow is identified and the model is updated to predict pressure losses in the fluid loop accordingly. The updated model agrees with the experimental data and can be used in the optimal design of thermosiphon passive thermal management systems.

CHAPTER 6

CONCLUSIONS

6.1 Summary and conclusions

This work addressed the need for an advanced passive thermal management system for cooling of high power electronics to be used in grid level power routing. The solid state devices used the power convertor augmented transformer (PCAT) design are critically limited thermally and present unique thermal management challenges. These discrete heat sources require a system capable of maintaining mounting temperatures at or below 100 °C in ambient conditions up to 40 °C while offering reliability consistent with grid level 30 year MTBF. This specific topology is nominally rated at 5 kW thermal load distributed across 48 discrete devices. An area enhanced single-phase closed-loop thermosiphon design concept was developed to address these distinct challenges. Design selection required the ability to predict the performance of a thermosiphon design. An analytical model was developed, utilizing existing heat transfer and fluid dynamic correlations. The model was designed to be parametric, enabling individual geometries to be changed independently. The thermosiphon was divided into four constant cross section segments and the appropriate correlations were applied to each. A set of unknowns and corresponding set of governing equations were identified from first law energy balance, Bernoulli streamline analysis, and heat transfer thermal circuit analysis. A 300W bench top demonstration thermosiphon was built and tested at several thermal loads to evaluate the efficacy of the multi-physics model. The data showed device mounting temperature prediction within 3.7 °C and thermal resistance prediction within 8%, which is acceptable in heat transfer applications. The model solved in less than 0.05 seconds, suitable for iterative use in numerical optimization.

Creation of a rapid design sizing tool required implementing the multi-physics thermosiphon model inside a numerical optimization routine. A particle swarm optimization (PSO) was chosen for its suitability to large-scale non-linear solution space applications. The critical geometries identified in the model development were either specified by external constraints, or selected for inclusion in the optimization and bounded by pragmatic limits. The design constraints of thermal load, baseplate dimensions, and ambient temperature were used to define the problem. An objective function was used to penalize solutions for deviation from the target steady state device mounting temperature. An additional penalty was incurred linearly with increasing system volume. The PSO was found to converge consistently in all five trials, and solved in an average time of 55 seconds.

The geometries resulting from this rapid design optimization were developed into a 2.5kW passive thermal management system (PTMS) module design. The module was built, instrumented, and tested at elevated ambient temperatures in an elevated ambient testing chamber designed and built for this experiment. Steady state data were collected for three trials at 2.5kW thermal load and 40 °C ambient. A fourth trial was conducted at 35 °C ambient and a fifth at 30 °C ambient. The overall system performance agreed exceptionally with the model predictions. Device mounting temperature data were within 1.1 °C of model prediction and system thermal resistances were within 2% of predicted. Examination of fluid temperatures measurements revealed disagreements as large as 29 °C between experiment and model. Evaluation of the model exposed an incorrect assumption with regard to flow regime inside the fluid loop. The model is updated with appropriate low Reynolds flow correlations, reducing the maximum fluid temperature disagreement to 8 °C.

Pursuant to work summarized here and presented in the previous chapters, the following conclusions can be made:

- An analytical multi-physics single-phase closed-loop thermosiphon model was created. This model predicted 300W demonstration thermosiphon device mounting temperature within 3.7 °C and thermal resistance within 8%.
- The analytical multi-physics single-phase closed-loop thermosiphon model was used in a particle swarm optimization to select the critical geometries for a 2.5kW thermosiphon design.
- The analytical multi-physics single-phase closed-loop thermosiphon model predicted 2.5kW IDCL thermosiphon device mounting temperature within 1.1 °C and system thermal resistance within 2%.
- The presence of low Reynolds number flow in the 2.5kW thermosiphon resulted in fluid temperature disagreements as large as 29 °C between experiment and model.
- The model was updated to account for low Reynolds flow behavior and the maximum fluid temperature disagreement was reduced to 8 °C.

6.2 Contributions

Pursuant to the work presented in the previous chapters, the following contributions were made:

- A unique thermosiphon design with internal area enhancements was created to address the need for high reliability passive thermal management of power electronics.
- A parametric, analytical, multi-physics model of a single-phase closed-loop thermosiphon was developed. This model was improved to better capture low Reynolds number flow based on experimental data.
- A rapid passive thermal management design sizing tool was created by performing a particle swarm optimization using the multi-physics model.
- The following papers have been published or are under review:

1. Benjamin Loeffler, J. Rhett Mayor, S. Andrew Semidey, "Multiphysics Thermosiphon Model for Passive Thermal Management of Direct AC/AC Convertor Cells," ASME 6th International Conference on Energy Sustainability, 2012.
2. Benjamin Loeffler, J. Rhett Mayor, S. Andrew Semidey, "Particle swarm optimization of a passive thermal management system" submitted for inclusion in IEEE International Electric Machines and Drives Conference, IEMDC '13, May 12-15, 2013 Chicago, IL.
3. Benjamin Loeffler, J. Rhett Mayor, S. Andrew Semidey, "An improved thermosiphon model accounting for low Reynolds flow regimes" submitted for inclusion in ASME 2013 Summer Heat Transfer Conference, 7th International Conference on Energy Sustainability, July 14-19 2013 Minneapolis, MN.
4. Benjamin Loeffler, J. Rhett Mayor, S. Andrew Semidey," Thermosiphon for Passive Thermal Management of Direct AC/AC Converter Cells: Part I" ASME

Journal of Thermal Science and Engineering Applications. Paper Number TSEA-12-1189.

5. Benjamin Loeffler, J. Rhett Mayor, S. Andrew Semidey," Thermosiphon for Passive Thermal Management of Direct AC/AC Converter Cells: Part II" in preparation for submission to ASME Journal of Thermal Science and Engineering Applications.

6.3 Recommendations and future work

Several possible extensions of this work were identified during the course of this study. These paths are presented here as recommendations for future work.

- Low Reynolds flow model particle swarm optimization

The low Reynolds flow correlations identified in Chapter 5 were included in the model and verified against data from the 2.5kW thermosiphon. This updated low Reynolds flow model should be implemented in the PSO to enable the optimal design of thermosiphon for any application. The new design should be built and validated against the model. Furthermore, the presence of mixed convection in the internal flows should be further investigated. Grasshof to Reynolds comparison indicates mixed or even natural convection while all data strongly indicated fully developed laminar behavior.

- Hot side convection area enhancement

The design sensitivity study reported in Chapter 4 indicates a correlation between hot side performance and cold side area requirements. A lower thermal resistance path from the devices to the fluid allows the thermosiphon to operate with greater fluid temperatures while maintaining acceptable device temperatures. Elevated fluid temperatures increase the temperature gradient between the cold side rejection area and the ambient air, reducing the surface area needed to reach the needed heat rejection. Area enhancement in the form of meso-features on the hot side fin surfaces may allow significant reductions in total system volume. The increased cost of high performance hot side arrays should be compared to the cost savings in lower volume cold side arrays.

- Cold side performance enhancement

Passive cooling systems are always limited by their ability to transfer heat to ambient air. Area enhancement of the cold side surfaces should be explored and the impact of the enhancement approaches on the manufacturability and cost should be quantified. Methods for increasing heat transfer coefficient such as the use of baffling and chimneys should be explored. The geometries of these enhancements should be included in the model and optimization for use in design optimization. The cost-to-performance relationship should be captured in a revised objective function for the optimization algorithm.

[1] "State Electricity Profiles 2010," *U.S. Energy Information Administration,* January 2012 2012.

[2] U. S. E. I. Administration, "Table 5.6.B. Average Retail Price of Electricity to Ultimate Customers by End-Use Sector," *Electric Power Monthly,* 2012.

[3] F. Kreikebaum, D. Das, Y. Yang, F. Lambert, and D. Divan, "Smart Wires - A Distributed, Low-Cost Solution for Controlling Power Flows and Monitoring Transmission Lines."

[4] D. Das, D. M. Divan, and R. G. Harley, "Power flow control in networks using controllable network transformers," *Power Electronics, IEEE Transactions on,* vol. 25, pp. 1753-1760, 2010.

[5] H. Johal and D. Divan, "From Power Line to Pipeline-Creating an Efficient and Sustainable Market Structure," 2008, pp. 1-7.

[6] D. Divan and H. Johal, "A smarter grid for improving system reliability and asset utilization," 2006, pp. 1-7.

[7] D. Divan, J. Sastry, A. Prasai, and H. Johal, "Thin AC converters—A new approach for making existing grid assets smart and controllable," 2008, pp. 1695-1701.

[8] F. Blaabjerg, A. Consoli, J. A. Ferreira, and J. D. van Wyk, "The future of electronic power processing and conversion," *Industry Applications, IEEE Transactions on,* vol. 41, pp. 3-8, 2005.

[9] D. Divan and H. Johal, "Distributed FACTS—a new concept for realizing grid power flow control," *Power Electronics, IEEE Transactions on,* vol. 22, pp. 2253-2260, 2007.

[10] D. Divan and J. Sastry, "Control of multilevel direct AC converters," in *Energy Conversion Congress and Exposition, 2009. ECCE 2009. IEEE,* 2009, pp. 3077-3084.

[11] "IGBT/SiC Diode Co-pack," *GeneSic Semiconductor,* vol. GA100XCP12-227, January 2011 2011.

[12] R. Beeckman, "NEMA Magnet Wire Thermal Class Ratings: How to Use Them, and How They are Derived," *Essex Group, Inc.*

[13] Timken, "Timken Engineering Manual."

[14] R. G. Budynas and J. K. Nisbett, *Shigley's Mechanical Engineering Design* vol. 8: McGraw-Hill, 2008.

[15] T. Fisher and K. Torrance, "Free convection limits for pin-fin cooling," *Journal of heat transfer,* vol. 120, p. 633, 1998.

[16] K. Gschneidner and V. Pecharsky, "Thirty years of near room temperature magnetic cooling: Where we are today and future prospects," *International journal of refrigeration,* vol. 31, pp. 945-961, 2008.

[17] F. P. Incropera, T. L. Bergman, A. S. Lavine, and D. P. DeWitt, *Fundamentals of heat and mass transfer*: Wiley, 2007.

[18] J. W. Vandersande and J. P. Fleurial, "Thermal management of power electronics using thermoelectric coolers," 1996, pp. 252-255.

[19] R. David, in *CRC Handbook of Thermoelectrics*, ed: CRC Press, 1995.

[20] R. Venkatasubramanian, E. Siivola, T. Colpitts, and B. O'quinn, "Thin-® lm thermoelectric devices with high room-temperature® figures of merit," *Materials for Sustainable Energy: A Collection of Peer-Reviewed Research and Review Articles from Nature Publishing Group*, p. 120, 2010.

[21] D. Kim and C. Infante Ferreira, "Solar refrigeration options–a state-of-the-art review," *International journal of refrigeration*, vol. 31, pp. 3-15, 2008.

[22] W. G. Anderson, J. H. Rosenfeld, D. Angirasa, and Y. Mi, "Evaluation of heat pipe working fluids in the temperature range 450 to 700 K," 2004, p. 20.

[23] W. G. Anderson, P. M. Dussinger, and D. Sarraf, "High Temperature Water Heat Pipe Life Tests," 2006, p. 100.

[24] D. Japikse, "Advances in Thermosyphon Technology," *Advances in Heat Transfer*, vol. 9, pp. 1-111, 1973.

[25] "IEEE Guide for Loading Mineral-Oil-Immersed Transformers," *IEEE Standards*, 1996.

[26] "Oil Filled Transformer," *powertransformersblog.com*, vol. Kva and Mva Oil Filled Power Transformers and Differential Relay Protection.

[27] F. E. L. D.C. Hamilton, L.D. Palmer, "The Nature of the Flow of Ordinary Fluids in a Thermal Convection Harp," ed: Oak Ridge National Laboratory, 1954.

[28] J. Kunes, "Characteristics of Thermosiphon Flow in a Model Transformer Oil Circuit," *Power Apparatus and Systems, Part III. Transactions of the American Institute of Electrical Engineers*, vol. 77, pp. 973-976, 1958.

[29] D. Japikse, "Heat transfer in open and closed thermosyphons," *Purdue University*, vol. Ph.D. Thesis
1969.

[30] D. Japikse, P. Jallouk, and E. Winter, "Single-phase transport processes in the closed thermosyphon," *International Journal of Heat and Mass Transfer*, vol. 14, pp. 869-887, 1971.

[31] D. Japikse and E. Winter, "HEAT TRANSFER AND FLUID FLOW IN THE CLOSED THERMOSYPHON," Purdue Univ., West Lafayette, Ind.1970.

[32] D. Japikse and E. Winter, "Single-phase transport processes in the open thermosyphon," *International Journal of Heat and Mass Transfer,* vol. 14, pp. 427-441, 1971.

[33] J. E. Hart, "A new analysis of the closed loop thermosyphon," *International Journal of Heat and Mass Transfer,* vol. 27, pp. 125-136, 1984.

[34] M. Bernier and B. Baliga, "A 1-D/2-D model and experimental results for a closed-loop thermosyphon with vertical heat transfer sections," *International Journal of Heat and Mass Transfer,* vol. 35, pp. 2969-2982, 1992.

[35] M. Polentini, S. Ramadhyani, and F. Incropera, "Single-phase thermosyphon cooling of an array of discrete heat sources in a rectangular cavity," *International Journal of Heat and Mass Transfer,* vol. 36, pp. 3983-3996, 1993.

[36] R. T. Dobson and J. C. Ruppersberg, "Flow and heat transfer in a closed loop thermosyphon. Part I - theoretical simulation," *Journal of Energy in Southern Africa,* vol. 18, August 2007 2007.

[37] J. Ruppersberg and R. Dobson, "Flow and heat transfer in a closed loop thermosyphon Part II–experimental simulation," *Journal of Energy in Southern Africa,* vol. 18, p. 41, 2007.

[38] P. Welander, "On the oscillatory instability of a differentially heated fluid loop," *J. Fluid Mech,* vol. 29, pp. 17-30, 1967.

[39] E. Burroughs, E. Coutsias, and L. Romero, "A reduced-order partial differential equation model for the flow in a thermosyphon," *Journal of Fluid Mechanics,* vol. 543, pp. 203-237, 2005.

[40] P. Vijayan, "Experimental observations on the general trends of the steady state and stability behaviour of single-phase natural circulation loops," *Nuclear engineering and design,* vol. 215, pp. 139-152, 2002.

[41] I. Ishihara, T. Fukui, and R. Matsumoto, "Natural convection in a vertical rectangular enclosure with symmetrically localized heating and cooling zones* 1," *International journal of heat and fluid flow,* vol. 23, pp. 366-372, 2002.

[42] M. Maiani, W. de Kruijf, and W. Ambrosini, "An analytical model for the determination of stability boundaries in a natural circulation single-phase thermosyphon loop," *International journal of heat and fluid flow,* vol. 24, pp. 853-863, 2003.

[43] G. Muscato and M. Xibilia, "Modeling and control of a natural circulation loop," *Journal of Process Control,* vol. 13, pp. 239-251, 2003.

[44] R. M. Del Vecchio, *Transformer design principles: with applications to core-form power transformers*: CRC, 2001.

[45] L. W. Pierce, "Predicting liquid filled transformer loading capability," *Industry Applications, IEEE Transactions on,* vol. 30, pp. 170-178, 1994.

[46] K. Eckholz, W. Knorr, M. Schäfer, K. Feser, and E. Cardillo, "New developments in transformer cooling calculations," 2004, pp. 12-09.

[47] G. Swift, T. S. Molinski, and W. Lehn, "A fundamental approach to transformer thermal modeling. I. Theory and equivalent circuit," *Power Delivery, IEEE Transactions on,* vol. 16, pp. 171-175, 2001.

[48] A. Oliver, "Estimation of transformer winding temperatures and coolant flows using a general network method," *Generation, Transmission and Distribution [see also IEE Proceedings-Generation, Transmission and Distribution], IEE Proceedings,* vol. 127, pp. 395-405, 1980.

[49] G. Swift, T. S. Molinski, R. Bray, and R. Menzies, "A fundamental approach to transformer thermal modeling. II. Field verification," *Power Delivery, IEEE Transactions on,* vol. 16, pp. 176-180, 2001.

[50] J. Smolka and A. J. Nowak, "Experimental validation of the coupled fluid flow, heat transfer and electromagnetic numerical model of the medium-power dry-type electrical transformer," *International journal of thermal sciences,* vol. 47, pp. 1393-1410, 2008.

[51] M. A. Tsili, E. I. Amoiralis, A. G. Kladas, and A. T. Souflaris, "Coupled 3D Fluid Flow-Thermal FEM Model for Power Transformer Temperature Analysis," 2009.

[52] R. Warzoha and A. S. Fleischer, "Thermal Management of a 15 kV/100 kVA Intelligent Universal Transformer," *ASME Journal of Thermal Science and Engineering Applications,* vol. 3, March 2011 2011.

[53] W. J. BAILEY, "Solar Heater," ed: Google Patents, 1910.

[54] B. Norton and S. Probert, "Natural-circulation solar-energy stimulated systems for heating water," *Applied Energy,* vol. 11, pp. 167-196, 1982.

[55] D. Close, "The performance of solar water heaters with natural circulation," *Solar energy,* vol. 6, pp. 33-40, 1962.

[56] K. Ong, "A finite-difference method to evaluate the thermal performance of a solar water heater," *Solar energy,* vol. 16, pp. 137-147, 1974.

[57] K. S. Ong, "An improved computer program for the thermal performance of a solar water heater," *Solar energy,* vol. 18, pp. 183-191, 1976.

[58] G. Morrison and D. Ranatunga, "Thermosyphon circulation in solar collectors," *Solar energy,* vol. 24, pp. 191-198, 1980.

[59] L. Wenxian and L. Enrong, "Parametric Studies of Thermosyphon Solar Water Systems with Electric Heaters," *Energy,* vol. 17, pp. 397-403, 1992.

[60] E. I. Amoiralis, M. A. Tsili, A. G. Kladas, and A. T. Souflaris, "Geometry optimization of power transformer cooling system based on coupled 3D FEM thermal-CFD analysis," 2010, pp. 1-1.

[61] J. Gastelurrutia, J. C. Ramos, A. Rivas, G. S. Larraona, J. Izagirre, and L. d. Río, "Zonal thermal model of distribution transformer cooling," *Applied thermal engineering,* vol. 31, pp. 4024-4035, 2011.

[62] J. Kennedy and R. Eberhart, "Particle swarm optimization," 1995, pp. 1942-1948 vol. 4.

[63] Y. del Valle, G. K. Venayagamoorthy, S. Mohagheghi, J. C. Hernandez, and R. G. Harley, "Particle swarm optimization: basic concepts, variants and applications in power systems," *Evolutionary Computation, IEEE Transactions on,* vol. 12, pp. 171-195, 2008.

[64] S. A. Semidey and J. R. Mayor, "Parametric Fin Array Optimization for Radial Flux Machines Considering Time Varying Loads," 2011.

[65] S. A. Semidey, Y. Duan, J. R. Mayor, and R. G. Harley, "Optimal electromagnetic-thermo-mechanical integrated design for surface mount permanent magnet machines considering load profiles," 2010, pp. 3646-3653.

[66] W. M. Rohsenow, J. P. Hartnett, Y. I. Cho, and K. . *Handbook of heat transfer* vol. 3: McGraw-Hill New York, 1998.

[67] A. Bar-Cohen and W. Rohsenow, "Thermally optimum spacing of vertical, natural convection cooled, parallel plates," *Journal of heat transfer,* vol. 106, p. 116, 1984.

[68] B. R. Munson, D. F. Young, and T. H. Okiishi, *Fundamentals of fluid mechanics* vol. 3: Wiley York, NY,, USA, 1998.

[69] S. J. Kline and F. McClintock, "Describing uncertainties in single-sample experiments," *Mechanical engineering,* vol. 75, pp. 3-8, 1953.

[70] S. Kakaç, R. K. Shah, and W. Aung, *Handbook of single-phase convective heat transfer*: Wiley New York et al., 1987.

[71] B. Birge, "Particle Swarm Optimization Toolbox," *MatlabCentral File Exchange,* 2005.

[72] H. L. Langhaar, "Steady flow in the transition length of a straight tube," *J. appl. Mech,* vol. 9, pp. 55-58, 1942.

[73] L. Han, "Hydrodynamic entrance lengths for incompressible laminar flow in rectangular ducts," *Journal of Applied Mechanics,* vol. 27, p. 403, 1960.

[74] W. Kays, *Loss coefficients for abrupt changes in flow cross section with low Reynolds number flow in single and multiple tube systems*, 1950.

APPENDIX A

PARAMETRIC MULTIPHYSICS THERMOSIPHON MODEL ALGORITHM

This Appendix displays the Matlab code implementation of the multiphysics thermosiphon model algorithm.

- `Main Code Block (modified from [71])`

```
%% Main Script
% This Script defines the problem and constants and performs Particle Swarm
% Optimization

clear
clc
close all

%% Global Conditions and Variables
% Material Properties
k_Al=167; %[W/m-K]
k_Cu=400; %[W/m-K]
k_steel=61; %[W/m-K]

%Radiation Constants
epsilon_HS=.03; %polished Aluminum
absorb_HS=.09;
epsilon_CS=.9; %Aluminum Oxide White Paint
absorb_CS=.09;

sigma=5.67e-8; %Boltzmann

g=9.81; %[m/s^2]


%% Problem Definition

% Operating Conditions
Q_in=2500; %[W]
T_amb=40; %[C]
T_sur=40; %[C]
W_Cell=6;
L_Cell=6;
Cell_Rows=3;
Cell_Columns=2;
Cell_Spacing=1; %Gap between Device mounting plates

% Fluid Selection
i_fluid=3; %FLUIDS={'ISO22' 'Novec7500' 'Midel'}

% Hot Side
Plenum_Wall=.5;  %Thickness of Plenum Wall Material
HS_Transit=.5;  % Vertical Distance between end of HS fins and plenum walls
W_mount=(Cell_Columns*W_Cell)+((Cell_Columns-1)*Cell_Spacing);
L_mount=(Cell_Rows*L_Cell)+((Cell_Rows-1)*Cell_Spacing);
W_HS=W_mount+(2*HS_wall);%
L_HS=L_mount+(2*(HS_transit+HS_wall));%
k_HSfin=k_Cu;  %Fin Material
k_HSwall=k_Al;  %Plenum Material

% Cold Side
CS_Plate=.060;  %Thickness of Cold Side Sheetmetal
```

```
    CS_Seal=.25;  %Bead/Seamweld width around perimeter of CS plates
    k_CSwall=k_steel;  %Plate material

    % Manifolds
    Man_wall=.25; %Manifold pipe wall thickness
    N_Man=2; %Number of manifolds
    k_manifold=k_steel;  %Manifold material

    %% Define Guesses for System of Equations solver
    T1guess=50;
    T2guess=85;
    T3guess=80;
    T4guess=55;
    m_dotguess=.05;
    Q_UMguess=.02*Q_in;
    Q_CSguess=.95*Q_in;
    Q_LMguess=.02*Q_in;

    %% Passthru Variables Vector

    vConstants=[Q_in T_amb T_sur W_cell L_cell Cell_Rows Cell_Columns i_fluid Cell_Spacing
Plenum_Wall HS_Transit W_mount L_mount W_HS L_HS k_HSfin k_HSwall CS_Plate CS_Seal
k_CSwall Man_wall N_Man k_manifold epsilon_HS absorb_HS epsilon_CS absorb_CS T1guess
T2guess T3guess T4guess m_dotguess Q_UMguess Q_CSguess Q_LMguess]


    %% Optimization Variable Bounds

    % Variable 1: HS fin spacing
    a_HS_min=.01;
    a_HS_max=1;

    % Variable 2: HS fin height
    b_HS_min=.5;
    b_HS_max=4;

    % Variable 3: HS fin thickness
    t_HS_min=.01;
    t_HS_max=.5;

    % Variable 4: Manifold Diameter
    D_min=.01;
    D_max=.5;

    % Variable 5: CS internal spacing (oil gap)
    a_CS_min=.25;
    a_CS_max=1;

    % Variable 6: CS Plate Spacing (air gap)
    a_amb_min=.01;
    a_amb_max=1;

    % Variable 7: CS Plate Width
    W_CS_min=12;
    W_CS_max=48;

    % Variable 8: CS Plate Length
    L_CS_min=36;
    L_CS_max=72;

    % Variable 9: Number of Plates in CS Array
    N_HX_min=1;
    N_HX_max=20;

    %% Particle Swarm Optimization
    tic
    rand('state',sum(100*clock));
    functname = 'LF_PSO_Central';
    Dvar = 9;      % number of changing variables
```

```
    VR=[a_HS_min,a_HS_max; %a_HS (channel width)
        b_HS_min,b_HS_max;    %b_HS (channel depth/height)
        t_HS_min,t_HS_max ;   %t_HS (fin thickness)
        D_min,D_max;  %D (Manifold Diameter)
        a_CS_min,a_CS_max ;    %a_CS (CS internal channel width)
        a_amb_min,a_amb_max ;   %a_amb (CS plate air gap)
        W_CS_min,W_CS_max;
        L_CS_min,L_CS_max;
        N_HX_min,N_HX_max];     %N_HX (Number of CS plates)


    %VarRange - matrix of ranges for each input variable, of form:
    %        [ ]
    minmax = 0;          % 1 is max , 0 is min
    mv = [.05 2 .05 .5 .05 .25 6 6 3];     % Max particle velocity, either a scalar or a
vector of length Dvar
    % plotfcn='goplotpso';

    % sets up default pso params

    df      = 0;  % Epochs between updating display, default = 100. if 0, no display
    me      = 1200;   % Maximum number of iterations (epochs) to train
    ps      = 18;   % Population size
    ac1     = 1;    % Acceleration const 1 (local best influence)
    ac2     = 1;    % Acceleration const 1 (global best influence)
    iw1     = .5;  % Initial inertia weight
    iw2     = 2;  % Final inertia weight
    iwe     = 400; % Epoch when inertial weight at final value
    ergrd   = 1e-2;% Minimum global error gradient, if abs(Gbest(i+1)-Gbest(i)) < gradient
over certain length of epochs, terminate run
    ergrdep = 250;  % Epochs before error gradient criterion terminates run
    errgoal = NaN;  % Error goal, if NaN then unconstrained min or max
    trelea  = 1;    % Type flag (which kind of PSO to use); 0 = Common PSO w/intertia; 1,2
= Trelea types 1,2; 3 = Clerc's Constricted PSO, Type 1"

    % set plotting flag
    % plotflg=0;

    % preallocate variables for speed up
     tr = ones(1,me)*NaN;

    % set the velocity limits of the variables
    % velmaskmin = -mv*ones(ps,Dvar);                % min vel all same
    % velmaskmax = mv*ones(ps,Dvar);                 % max vel all same
    velmaskmin = repmat(forcerow(-mv),ps,1);   % min vel different
    velmaskmax = repmat(forcerow( mv),ps,1);   % max vel different

    posmaskmin  = repmat(VR(1:Dvar,1)',ps,1);  % min pos, psXD matrix
    posmaskmax  = repmat(VR(1:Dvar,2)',ps,1);  % max pos
    posmaskmeth = 3; % 3=bounce method (see comments below inside epoch loop)

    % PLOTTING
     message = sprintf('PSO: %%g/%g iterations, GBest = %%20.20g.\n',me);

    %% INITIALIZE

    % initialize population of particles and their velocities at time zero,
    %  format of pos = (particle#, dimension)
    %  construct random population positions bounded by VR
    pos(1:ps,1:Dvar) = normmat(rand([ps,Dvar]),VR',1);

    % construct initial random velocities between -mv,mv
     vel(1:ps,1:Dvar) = normmat(rand([ps,Dvar]),[forcecol(-mv),forcecol(mv)]',1);

    % initial pbest positions vals
     pbest = pos;

    % VECTORIZE THIS, or at least vectorize cost funct call
    vConditions=repmat(Conditions,ps,1);
    out = feval(functname,[pos vConstants]);  % returns column of cost values (1 for each
particle)
```

```
    %---------------------------

     pbestval=out;   % initially, pbest is same as pos

    [gbestval,idx1] = max(pbestval);    % this picks gbestval when we want to maximize the function

     % preallocate a variable to keep track of gbest for all iters
     bestpos   = zeros(me,Dvar+1)*NaN;
     gbest     = pbest(idx1,:);  % this is gbest position

     bestpos(1,1:Dvar) = gbest;

    % this part used for implementing Carlisle and Dozier's APSO idea
    % slightly modified, this tracks the global best as the sentry whereas
    % their's chooses a different point to act as sentry
    % see "Tracking Changing Extremea with Adaptive Particle Swarm Optimizer",
    % part of the WAC 2002 Proceedings, June 9-13, http://wacong.com
     sentryval = gbestval;
     sentry    = gbest;

    %% ITERATING THE LOOP

    rstflg = 0; % for dynamic environment checking

     cnt    = 0; % counter used for updating display according to df in the options
     cnt2   = 0; % counter used for the stopping subroutine based on error convergence
     iwt(1) = iw1;
    %  figure
    %  hold on
    %  axis([4 10 10 40 -10 10])
    for i=1:me  % start epoch loop (iterations)

         out        = feval(functname,[[pos vConditions];[gbest Conditions]]);
         outbestval = out(end,:);
         out        = out(1:end-1,:);
    %     scatter3(pos(:,1),pos(:,2),out)

       % pause
         tr(i+1)          = gbestval; % keep track of global best val
         te               = i; % returns epoch number to calling program when done
         bestpos(i,1:Dvar+1) = [gbest,gbestval];

         %assignin('base','bestpos',bestpos(i,1:Dvar+1));
    %    %------------------------------------------------------------------------
    %    % this section does the plots during iterations
    %     if plotflg==1
    %       if (rem(i,df) == 0 ) | (i==me) | (i==1)
    %          fprintf(message,i,gbestval);
    %          cnt = cnt+1; % count how many times we display (useful for movies)
    %
    %          eval(plotfcn); % defined at top of script
    %
    %       end  % end update display every df if statement
    %     end % end plotflg if statement

        % check for an error space that changes wrt time/iter
        % threshold value that determines dynamic environment
        % sees if the value of gbest changes more than some threshold value
        % for the same location
        chkdyn = 1;
        rstflg = 0; % for dynamic environment checking

        if chkdyn==1
         threshld = 0.05;  % percent current best is allowed to change, .05 = 5% etc
         letiter  = 5; % # of iterations before checking environment, leave at least 3 so PSO has time to converge
         outorng  = abs( 1- (outbestval/gbestval) ) >= threshld;
         samepos  = (max( sentry == gbest ));

         if (outorng && samepos) && rem(i,letiter)==0
```

```
         rstflg=1;
       % disp('New Environment: reset pbest, gbest, and vel');
       %% reset pbest and pbestval if warranted
%        outpbestval = feval( functname,[pbest] );
%        Poutorng    = abs( 1-(outpbestval./pbestval) ) > threshld;
%        pbestval    = pbestval.*~Poutorng + outpbestval.*Poutorng;
%        pbest       = pbest.*repmat(~Poutorng,1,Dvar) + pos.*repmat(Poutorng,1,Dvar);

        pbest     = pos; % reset personal bests to current positions
        pbestval  = out;
        vel       = vel*10; % agitate particles a little (or a lot)

       % recalculate best vals
        if minmax == 1
           [gbestval,idx1] = max(pbestval);
        elseif minmax==0
           [gbestval,idx1] = min(pbestval);
        end

        gbest  = pbest(idx1,:);

        % used with trainpso, for neural net training
        % assign gbest to net at each iteration, these interim assignments
        % are for plotting mostly
        if strcmp(functname,'pso_neteval')
           net=setx(net,gbest);
        end
     end  % end if outorng

     sentryval = gbestval;
     sentry    = gbest;

    end % end if chkdyn

    % find particles where we have new pbest, depending on minmax choice
    % then find gbest and gbestval
     %[size(out),size(pbestval)]
    if rstflg == 0
     if minmax == 0
        [tempi]            = find(pbestval>=out); % new min pbestvals
        pbestval(tempi,1)  = out(tempi);   % update pbestvals
        pbest(tempi,:)     = pos(tempi,:); % update pbest positions

        [iterbestval,idx1] = min(pbestval);

        if gbestval >= iterbestval
            gbestval = iterbestval;
            gbest    = pbest(idx1,:);
            % used with trainpso, for neural net training
            % assign gbest to net at each iteration, these interim assignments
            % are for plotting mostly
             if strcmp(functname,'pso_neteval')
                net=setx(net,gbest);
             end
        end
     elseif minmax == 1
        [tempi,dum]        = find(pbestval<=out); % new max pbestvals
        pbestval(tempi,1)  = out(tempi,1); % update pbestvals
        pbest(tempi,:)     = pos(tempi,:); % update pbest positions

        [iterbestval,idx1] = max(pbestval);
        if gbestval <= iterbestval
            gbestval = iterbestval;
            gbest    = pbest(idx1,:);
            % used with trainpso, for neural net training
            % assign gbest to net at each iteration, these interim assignments
            % are for plotting mostly
             if strcmp(functname,'pso_neteval')
                net=setx(net,gbest);
             end
        end
```

```
     end
    end


 %   % build a simple predictor 10th order, for gbest trajectory
 %   if i>500
 %    for dimcnt=1:Dvar
 %      pred_coef  = polyfit(i-250:i,(bestpos(i-250:i,dimcnt))',20);
 %     % pred_coef  = polyfit(200:i,(bestpos(200:i,dimcnt))',20);
 %      gbest_pred(i,dimcnt) = polyval(pred_coef,i+1);
 %    end
 %    else
%       gbest_pred(i,:) = zeros(size(gbest));
%    end

   %gbest_pred(i,:)=gbest;
   %assignin('base','gbest_pred',gbest_pred);

 %   % convert to non-inertial frame
 %    gbestoffset = gbest - gbest_pred(i,:);
 %    gbest = gbest - gbestoffset;
 %    pos   = pos + repmat(gbestoffset,ps,1);
 %    pbest = pbest + repmat(gbestoffset,ps,1);

     %PSOPSOPSOPSOPSOPSOPSOPSOPSOPSOPSOPSOPSOPSOPSOPSOPSOPSOPSOPSOPSOPSOPSOPSOPSOPSO

      % get new velocities, positions (this is the heart of the PSO algorithm)
      % each epoch get new set of random numbers
       rannum1 = rand([ps,Dvar]); % for Trelea and Clerc types
       rannum2 = rand([ps,Dvar]);
       if     trelea == 2
        % from Trelea's paper, parameter set 2
         vel = 0.729.*vel...                              % prev vel
               +1.494.*rannum1.*(pbest-pos)...            % independent
               +1.494.*rannum2.*(repmat(gbest,ps,1)-pos); % social
       elseif trelea == 1
        % from Trelea's paper, parameter set 1
         vel = 0.600.*vel...                              % prev vel
               +1.700.*rannum1.*(pbest-pos)...            % independent
               +1.700.*rannum2.*(repmat(gbest,ps,1)-pos); % social
       elseif trelea ==3
        % Clerc's Type 1" PSO
         vel = chi*(vel...                                % prev vel
               +ac1.*rannum1.*(pbest-pos)...              % independent
               +ac2.*rannum2.*(repmat(gbest,ps,1)-pos)) ; % social
       else
        % common PSO algo with inertia wt
        % get inertia weight, just a linear funct w.r.t. epoch parameter iwe
         if i<=iwe
            iwt(i) = ((iw2-iw1)/(iwe-1))*(i-1)+iw1;
         else
            iwt(i) = iw2;
         end
        % random number including acceleration constants
         ac11 = rannum1.*ac1;    % for common PSO w/inertia
         ac22 = rannum2.*ac2;

         vel = iwt(i).*vel...                             % prev vel
               +ac11.*(pbest-pos)...                      % independent
               +ac22.*(repmat(gbest,ps,1)-pos);           % social
       end

       % limit velocities here using masking
        vel = ( (vel <= velmaskmin).*velmaskmin ) + ( (vel > velmaskmin).*vel );
        vel = ( (vel >= velmaskmax).*velmaskmax ) + ( (vel < velmaskmax).*vel );

       % update new position (PSO algo)
        pos = pos + vel;

       % position masking, limits positions to desired search space
       % method: 0) no position limiting, 1) saturation at limit,
```

```
       %         2) wraparound at limit , 3) bounce off limit
        minposmask_throwaway = pos <= posmaskmin;  % these are psXD matrices
        minposmask_keep      = pos >  posmaskmin;
        maxposmask_throwaway = pos >= posmaskmax;
        maxposmask_keep      = pos <  posmaskmax;

        if     posmaskmeth == 1
         % this is the saturation method
          pos = ( minposmask_throwaway.*posmaskmin ) + ( minposmask_keep.*pos );
          pos = ( maxposmask_throwaway.*posmaskmax ) + ( maxposmask_keep.*pos );
        elseif posmaskmeth == 2
         % this is the wraparound method
          pos = ( minposmask_throwaway.*posmaskmax ) + ( minposmask_keep.*pos );
          pos = ( maxposmask_throwaway.*posmaskmin ) + ( maxposmask_keep.*pos );
        elseif posmaskmeth == 3
         % this is the bounce method, particles bounce off the boundaries with -vel
          pos = ( minposmask_throwaway.*posmaskmin ) + ( minposmask_keep.*pos );
          pos = ( maxposmask_throwaway.*posmaskmax ) + ( maxposmask_keep.*pos );

          vel = (vel.*minposmask_keep) + (-vel.*minposmask_throwaway);
          vel = (vel.*maxposmask_keep) + (-vel.*maxposmask_throwaway);
        else
         % no change, this is the original Eberhart, Kennedy method,
         % it lets the particles grow beyond bounds if psoparams (P)
         % especially Vmax, aren't set correctly, see the literature
        end

     %PSOPSOPSOPSOPSOPSOPSOPSOPSOPSOPSOPSOPSOPSOPSOPSOPSOPSOPSOPSOPSOPSOPSOPSOPSOPSOPSO
% check for stopping criterion based on speed of convergence to desired
   % error
    tmp1 = abs(tr(i) - gbestval);
    if tmp1 > ergrd
       cnt2 = 0;
    elseif tmp1 <= ergrd
       cnt2 = cnt2+1;
       if cnt2 >= ergrdep
%           if plotflg == 1
%            fprintf(message,i,gbestval);
%            disp(' ');
%            disp(['--> Solution likely, GBest hasn''t changed by at least ',...
%                num2str(ergrd),' for ',...
%                    num2str(cnt2),' epochs.']);
%            eval(plotfcn);
%           end
         break
       end
    end

   % this stops if using constrained optimization and goal is reached
    if ~isnan(errgoal)
     if ((gbestval<=errgoal) && (minmax==0)) || ((gbestval>=errgoal) && (minmax==1))

%           if plotflg == 1
%               fprintf(message,i,gbestval);
%               disp(' ');
%               disp(['--> Error Goal reached, successful termination!']);
%
%               eval(plotfcn);
%           end
         break
     end
    end  % end ~isnan if

    %    % convert back to inertial frame
    %     pos = pos - repmat(gbestoffset,ps,1);
    %     pbest = pbest - repmat(gbestoffset,ps,1);
    %     gbest = gbest + gbestoffset;
    if rem(i,10) == 0
        display(i)
    end
end  % end epoch loop
```

```
%% Output

% OUT=[gbest';gbestval];
tr=[1:te];                  % Gbest at every iteration, traces flight of swarm
te=[tr(find(~isnan(tr)))];  % Epochs to train, returned as a vector 1:endepoch

dimensions=gbest;
```

- **Central Code Block**

```
function Output = LF_PSO_Central(Input)

Output=zeros(length(Input(:,1)),1);

parfor i=1:length(Input(:,1))

    values=Input(i,:);

    %     a_HS=values(1);
    %     b_HS=values(2);
    %     t_HS=values(3);
    D=values(4);
    a_CS=values(5);
    a_amb=values(6);
    W_CS=values(7);
    L_CS=values(8);
    N_HX=values(9);
    Q_in=values(10);
    %     T_amb=values(11);
    %     T_sur=values(12);
    %     W_cell=values(13);
    %     L_cell=values(14);
    %     Cell_Rows=values(15);
    %     Cell_Columns=values(16);
    %     i_fluid=values(17);
    %     Cell_Spacing=values(18);
    %     Plenum_Wall=values(19);
    %     HS_Transit=values(20);
    %     W_mount=values(21);
    %     L_mount=values(22);
    W_HS=values(23);
    L_HS=values(24);
    %     k_HSfin=values(25);
    %     k_HSwall=values(26);
    %     CS_Plate=values(27);
    %     CS_Seal=values(28);
    %     k_CSwall=values(29);
    %     Man_wall=values(30);
    %     N_Man=values(31);
    %     k_manifold=values(32);
    %     epsilon_HS=values(33);
    %     absorb_HS=values(34);
    %     epsilon_CS=values(35);
    %     absorb_CS=values(36);
    T1guess=values(37);
    T2guess=values(38);
    T3guess=values(39);
    T4guess=values(40);
    m_dotguess=values(41);
    Q_UMguess=values(42);
    Q_CSguess=values(43);
    Q_LMguess=values(44);


    b_CS=(W_CS)-(2*CS_seal);
    b_amb=W_CS;

    X_dim=(2*b_HS)+N_HX*(a_CS+a_amb+2*CS_plate);   %Into page

    L_x_Man=X_dim;  %Total Horizontal Length

    Z_dim=L_CS+D;   %Vertical
    L_z_Man=(Z_dim-L_HS);

    Y_dim=max([W_CS,W_HS]);    %Horizontal

    Volume=X_dim*Y_dim*Z_dim;   %Bounding Volume

    ModelParams=[values b_CS b_amb L_x_Man L_z_Man] ;
```

```
        %% Define Guesses for System of Equations solver
        x0=[T1guess T2guess T3guess T4guess m_dotguess Q_UMguess Q_CSguess Q_LMguess];

        x=LF_PSO_Solver(ModelParams,x0);

        % T1=x(1);
        % T2=x(2);
        % T3=x(3);
        % T4=x(4);
        % m_dot=x(5);
        % Q_UM=x(6);
        % Q_CS=x(7);
        % Q_LM=x(8);

        [Tmax_base H R P Q FLUX MixedCheck SumPressure SumQ V N_0 RE ENTRY AREA NU GR
MIXED Remainders]=LF_PSO_Model(ModelParams,x);


Output(i)=PTMS_Penalty(T_DeviceLimit,Tmax_base,Volume,SumPressure,SumQ,N_HX,X_dim);

    end
```

- **Solver Code Block**

```
    function [x,fval] =  LF_PSO_Solver(params,x0)

    x = fsolve(@nestedfun,x0,optimset('Display','off'));
    % x = lsqnonlin(@nestedfun,x0,[41 41 41 41 .0001 1 1 1],[200 200 200 200 5 500 2500 
500],optimset('Display','off'));

    % Nested function that computes the objective function

        function [f] = nestedfun(x)

            [Tmax_base H R P Q FLUX SumPressure SumQ V N_0 RE ENTRY AREA NU GR MIXED 
Remainders]=LF_PSO_Model(params,x);
            f=Remainders;

        end
    end
```

- Model Code Block

```
    function [Tmax_base H R P Q FLUX SumPressure SumQ V N_0 RE ENTRY AREA NU GR MIXED
Remainders]= LF_PSO_Model(ModelParams,x)

    FLUIDS={'ISO22' 'Novec7500' 'Midel'};
    sigma=5.67e-8; %Boltzmann
    g=9.81; %[m/s^2]

    %% Unknowns
    %         T1=x(1)+273; T2=x(2)+273; T3=x(3)+273; T4=x(4)+273; m_dot=x(5);
    %         Q_UM=x(6); Q_CS=x(7); Q_LM=x(8);

    T1=real(x(1))+273;  %LM to Adiabatic Header
    T2=T1; %Adiabatic Header to HS_inlet
    T3=real(x(2))+273;  %HS_outlet to Adiabatic Header
    T4=T3;  %Adiabatic Header to UM
    T5=real(x(3))+273;  %UM to CS
    T6=real(x(4))+273;  %CS to LM
    m_dot=real(x(5));
    Q_UM=real(x(6));
    Q_CS=real(x(7));
    Q_LM=real(x(8));

    %% Conditions and Constants [Kelvin, meters]
    %params=[Q_in T_amb T_sur W_cell L_cell Cell_Rows Cell_Columns i_fluid
    %Cell_Spacing HS_Base Plenum_Wall HS_Transit W_mount L_mount W_HS L_HS k_HSfin
    %k_HSwall CS_Plate CS_Seal k_CSwall Man_wall N_Man k_manifold epsilon_HS
    %absorb_HS epsilon_CS absorb_CS T1guess T2guess T3guess T4guess m_dotguess
    %Q_UMguess Q_CSguess Q_LMguess b_CS b_amb L_x_Man L_z_Man]

    a_HS=ModelParams(1)*.0254;
    b_HS=ModelParams(2)*.0254;
    t_HS=ModelParams(3)*.0254;
    D=ModelParams(4)*.0254;
    a_CS=ModelParams(5)*.0254;
    a_amb=ModelParams(6)*.0254;
    W_CS=ModelParams(7)*.0254;
    L_CS=ModelParams(8)*.0254;
    N_HX=ModelParams(9);
    Q_in=ModelParams(10);
    T_amb=ModelParams(11)+273;
    T_sur=ModelParams(12)+273;
    W_cell=ModelParams(13)*.0254;
    L_cell=ModelParams(14)*.0254;
    Cell_Rows=ModelParams(15);
    Cell_Columns=ModelParams(16);
    i_fluid=char(FLUIDS(ModelParams(17)));
    Cell_Spacing=ModelParams(18)*.0254;
    HS_Base=ModelParams(19)*.0254;
    Plenum_Wall=ModelParams(20)*.0254;
    HS_Transit=ModelParams(21)*.0254;
    W_Finned=ModelParams(22)*.0254;  %HS finned Dimensions
    L_Finned=ModelParams(23)*.0254;
    W_HS=ModelParams(24)*.0254;     %HS Outer Dimensions
    L_HS=ModelParams(25)*.0254;
    k_HSfin=ModelParams(26);
    k_HSwall=ModelParams(27);
    CS_Wall=ModelParams(28)*.0254;
    CS_Seal=ModelParams(29)*.0254;
    k_CSwall=ModelParams(30);
    Man_Wall=ModelParams(31)*.0254;
    N_Man=ModelParams(32);
    k_manifold=ModelParams(33);
    epsilon_HS=ModelParams(34);
    absorb_HS=ModelParams(35);
    epsilon_CS=ModelParams(36);
    absorb_CS=ModelParams(37);
    % T1guess=ModelParams(38);
    % T2guess=ModelParams(39);
    % T3guess=ModelParams(40);
```

```
    % T4guess=ModelParams(41);
    % m_dotguess=ModelParams(42);
    % Q_UMguess=ModelParams(43);
    % Q_CSguess=ModelParams(44);
    % Q_LMguess=ModelParams(45);
    b_CS=ModelParams(46)*.0254;
    b_amb=ModelParams(47)*.0254;
    L_x_Man=ModelParams(48)*.0254;
    L_z_Man=ModelParams(49)*.0254; % (L_total - L_Plenum)/2

    %% Dimensions [meters]

    %Hot Side Areas
    DeviceArea=W_Finned*L_Finned; % Base Finned Area
    DevicePlateArea=(Cell_Rows*L_cell)*(Cell_Columns*W_cell);
    n_HS=floor((W_Finned+t_HS)/(a_HS+t_HS)); % # Hot Side Channels
    FlowArea_HS=n_HS*a_HS*b_HS %Total Flow Area
    FlowArea_Plenum=b_HS*W_Finned;
    D_H_HS=(2*a_HS*b_HS)/(a_HS+b_HS);   %Hydraulic Diameter Rectangle
    HTArea_HS=(n_HS-1)*L_Finned*(b_HS+a_HS+b_HS);    % Fin Array Heat Transfer Area
    Area_Finned=L_Finned*W_Finned;
    %Fin efficiency
    Lc_HS=b_HS; %Tips not exposed
    Af_HS=2*L_Finned*Lc_HS; % Single Fin Area (excluding base and tip)
    At_HS=((n_HS-1)*Af_HS)+(n_HS*L_Finned*a_HS); %Total Fin Area + Total Base Area

    %Cold Side Dimensions
    n_CS=2*N_HX;    %Total number of internal plate surfaces
    HTArea_CS=n_CS*((b_CS*L_CS)-(2*N_Man*(.5*pi*(D/2)^2)));    % Total internal HT area (-
Cutouts for manifolds)
    FlowArea_CS=N_HX*a_CS*b_CS %Total Internal Flow Area
    D_H_CS=(2*a_CS*b_CS)/(a_CS+b_CS);   %Hydraulic Diameter Rectangle
    FlowArea_Port=N_HX*N_Man*D*a_CS;

    %Ambient Rejection Dimensions
    n_amb=n_CS-2;   %Number of internal rejection surfaces
    RejArea_amb=n_amb*((W_CS*L_CS)-(2*N_Man*(.5*pi*((D/2)+Man_Wall)^2)));   %Total
internal rejection area
    Depth_HX=N_HX*(a_CS+a_amb+(2*CS_Wall));
    RadArea_amb=2*((L_CS*W_CS)+(Depth_HX*L_CS)+(Depth_HX*W_CS)); %Bounding Rectangle
surface area
    D_H_amb=(2*a_amb*b_amb)/(a_amb+b_amb);
    FlowArea_amb=N_HX*a_amb*b_amb

    %Manifold Dimensions
    FlowArea_Man=N_Man*pi*.25*D^2 %Total Internal Manifold Flow Area
    HTArea_Man=N_Man*pi*D*L_x_Man;  %Internal HT Area of Upper or Lower Manifold Section
    CS_Port_Area=(N_Man*N_HX)*(a_CS*D); %Flow Area of ports into or out of plate array
    D_H_Port=(2*a_CS*D)/(a_CS+D);
    HTArea_ExtMan=N_Man*pi*(D+2*Man_Wall)*L_x_Man;  %External HT Area of Upper or Lower
Manifold Section

    H1=0;
    H2=L_z_Man;
    H3=L_CS-L_z_Man;
    H4=L_CS;
    H5=H4;
    H6=H1;

    %% Avg Temps to Evaluate Fluid Properties
    T_bar_HS=(T2+T3)/2;
    T_bar_UM=(T4+T5)/2;
    T_bar_CS=(T5+T6)/2;
    T_bar_LM=(T1+T6)/2;

    %% HT Fluid Properties (fluid property function [K])

    HSprop=feval(i_fluid,T_bar_HS);
    beta_HS=HSprop(1);
    nu_HS=HSprop(2);
    k_HS=HSprop(3);
```

```
    rho_HS=HSprop(4);
    cp_HS=HSprop(5);
    alpha_HS=HSprop(6);
    mu_HS=HSprop(7);
    Pr_HS=HSprop(8);

    CSprop=feval(i_fluid,T_bar_CS);
    beta_CS=CSprop(1);
    nu_CS=CSprop(2);
    k_CS=CSprop(3);
    rho_CS=CSprop(4);
    cp_CS=CSprop(5);
    alpha_CS=CSprop(6);
    mu_CS=CSprop(7);
    Pr_CS=CSprop(8);

    LMprop=feval(i_fluid,T_bar_LM);
    beta_LM=LMprop(1);
    nu_LM=LMprop(2);
    k_LM=LMprop(3);
    rho_LM=LMprop(4);
    cp_LM=LMprop(5);
    alpha_LM=LMprop(6);
    mu_LM=LMprop(7);
    Pr_LM=LMprop(8);

    UMprop=feval(i_fluid,T_bar_UM);
    beta_UM=UMprop(1);
    nu_UM=UMprop(2);
    k_UM=UMprop(3);
    rho_UM=UMprop(4);
    cp_UM=UMprop(5);
    alpha_UM=UMprop(6);
    mu_UM=UMprop(7);
    Pr_UM=UMprop(8);

    Temp12prop=feval(i_fluid,T1);
    rho_1=Temp12prop(4);
    rho_2=rho_1;

    Temp34prop=feval(i_fluid,T3);
    rho_3=Temp34prop(4);
    rho_4=rho_3;

    Temp5prop=feval(i_fluid,T5);
    rho_5=Temp5prop(4);
    mu_5=Temp5prop(7);

    Temp6prop=feval(i_fluid,T6);
    rho_6=Temp6prop(4);
    mu_6=Temp6prop(7);

    %% Air 300K from Incropera (FUNCTION NEEDED?)
    T_air=T_amb;
    rho_air=1.1614;
    k_air=26.3e-3;
    mu_air=184.6e-7;
    cp_air=1007;
    Pr_air=.707;
    beta_air=1/T_air;
    alpha_air=k_air/(rho_air*cp_air);
    nu_air=Pr_air*alpha_air;

    %% Fluid Dynamics [Laminar or Creep Flow with entry region] and Heat Transfer
[Internal Flows, Rohsenhow Parallel Plates]


    %% Average velocities for loss calcs
    V_HS=m_dot/(rho_HS*FlowArea_HS);
    V_UM=m_dot/(rho_UM*FlowArea_Man);
    V_CS=m_dot/(rho_CS*FlowArea_CS);
```

```
    V_LM=m_dot/(rho_LM*FlowArea_Man);
    V_CS_UPort=m_dot/(rho_5*CS_Port_Area);
    V_CS_LPort=m_dot/(rho_6*CS_Port_Area);


    %% Reynolds Numbers
    Re_HS=(rho_HS*V_HS*D_H_HS)/mu_HS;
    Re_UM=(rho_UM*V_UM*D)/mu_UM;
    Re_CS=(rho_CS*V_CS*D_H_CS)/mu_CS;
    Re_LM=(rho_LM*V_LM*D)/mu_LM;
    Re_UPort=(rho_5*V_CS_UPort*D_H_Port)/mu_5;
    Re_LPort=(rho_6*V_CS_LPort*D_H_Port)/mu_6;

    %% Fully developed Laminar Loss Coefficients
    C_HS=57.197*(a_HS/b_HS)^2-93.856*(a_HS/b_HS)+94.466; %Fit to table 2 from L.S. Han
Rect Ducts paper
    C_CS=57.197*(a_CS/b_CS)^2-93.856*(a_CS/b_CS)+94.466;
    C_Man=64;

    %% Square Sections Pressure Drop
    PHI_HS=-.0946*(a_HS/b_HS)^2+.01595*(a_HS/b_HS)+.0093;
    K_HS=-1.5005*(a_HS/b_HS)^2+2.6791*(a_HS/b_HS)+1.8391;
    L_e_HS=PHI_HS*D_H_HS*Re_HS;
    DeltaP_Loss_HS=((rho_HS*V_HS^2)/2)*(((C_HS/Re_HS)*(L_Finned/D_H_HS))+K_HS);

    PHI_CS=-.0946*(a_CS/b_CS)^2+.01595*(a_CS/b_CS)+.0093;
    K_CS=-1.5005*(a_CS/b_CS)^2+2.6791*(a_CS/b_CS)+1.8391;
    L_e_CS=PHI_CS*D_H_CS*Re_CS;
    DeltaP_Loss_CS=((rho_CS*V_CS^2)/2)*(((C_CS/Re_CS)*(L_CS/D_H_CS))+K_CS);


    %% Circlear Sections Pressure Drop
    DeltaP_Loss_UM=((8*mu_UM*V_UM*L_x_Man)/((D/2)^2))+((2.28*rho_UM*V_UM^2)/2);
%Langhaar Straight Tube paper
    DeltaP_Loss_LM=((8*mu_LM*V_LM*L_x_Man)/((D/2)^2))+((2.28*rho_LM*V_LM^2)/2);
%Langhaar Straight Tube paper
    DeltaP_Loss_LV=((8*mu_LM*V_LM*L_z_Man)/((D/2)^2))+((2.28*rho_LM*V_LM^2)/2);
%Langhaar Straight Tube paper, vertical length
    DeltaP_Loss_UV=((8*mu_UM*V_UM*L_z_Man)/((D/2)^2))+((2.28*rho_UM*V_UM^2)/2);
%Langhaar Straight Tube paper, vertical length

    %% Transitions Pressure Drop
    P_trim=1;
    K_Loss_1exp=(1.0431*(FlowArea_Man/FlowArea_Plenum)^2-
2.7113*(FlowArea_Man/FlowArea_Plenum)+1); % Expansion Round manifolds into plenum
    K_Loss_1cont=(-.3829*(FlowArea_HS/FlowArea_Plenum)^2-
.024*(FlowArea_HS/FlowArea_Plenum)+1.1964); %Contraction Plenum into Square fin Channels
    K_Loss_2exp=(.9883*(FlowArea_HS/FlowArea_Plenum)^2-
2.774*(FlowArea_HS/FlowArea_Plenum)+1); %Expansion Square Fin Channels to Plenum
    K_Loss_2cont=(-.4091*(FlowArea_Man/FlowArea_Plenum)+1.081); %Contraction Plenum into
Round Manifolds
    K_Loss_3cont=(1.0431*(CS_Port_Area/(D*(N_HX*(a_CS+(2*CS_Wall)+a_amb))))^2-
2.7113*(CS_Port_Area/(D*(N_HX*(a_CS+(2*CS_Wall)+a_amb))))+1);   %Contraction Round
Manifold into Square Port
    K_Loss_3exp=(.9883*(CS_Port_Area/FlowArea_CS)^2-2.774*(CS_Port_Area/FlowArea_CS)+1);
%Expansion Square Port into inf Plate
    K_Loss_4cont=(-.3829*(CS_Port_Area/FlowArea_CS)^2-
.024*(CS_Port_Area/FlowArea_CS)+1.1964);
    K_Loss_4exp=(.9883*(CS_Port_Area/(D*(N_HX*(a_CS+(2*CS_Wall)+a_amb))))^2-
2.774*(CS_Port_Area/(D*(N_HX*(a_CS+(2*CS_Wall)+a_amb))))+1);

    DeltaP12=-((rho_2*g*H2)-(rho_1*g*H1))-(P_trim*(DeltaP_Loss_LV));
    DeltaP_HSentry=-(K_Loss_1exp*rho_2*(V_LM^2)/2)-(K_Loss_1cont*rho_2*(V_HS^2)/2);
    DeltaP_HSmajor=-DeltaP_Loss_HS;
    DeltaP_HSexit=-(K_Loss_2exp*rho_3*(V_HS^2)/2)-(K_Loss_2cont*rho_3*(V_UM^2)/2);
    DeltaP_HSbern=-((rho_3*g*H3)-(rho_2*g*H2))-((rho_3*(V_UM^2)/2)-(rho_2*(V_LM^2)/2));
    DeltaP23=(P_trim*(DeltaP_HSentry+DeltaP_HSmajor+DeltaP_HSexit))+DeltaP_HSbern;
    DeltaP34=-((rho_4*g*H4)-(rho_3*g*H3))-(P_trim*(DeltaP_Loss_UV));
    DeltaP45=(P_trim*(-DeltaP_Loss_UM));
    DeltaP_CSentry=-(K_Loss_3cont*rho_5*(V_CS_UPort^2)/2)-
(K_Loss_3exp*rho_5*(V_CS_UPort^2)/2);
```

```
    DeltaP_CSmajor=-DeltaP_Loss_CS;
    DeltaP_CSexit=-(K_Loss_4cont*rho_6*(V_CS_LPort^2)/2)-
(K_Loss_4exp*rho_6*(V_CS_LPort^2)/2);
    DeltaP_CSbern=-((rho_6*g*H6)-(rho_5*g*H5))-((rho_6*(V_LM^2)/2)-(rho_5*(V_UM^2)/2));
    DeltaP56=(P_trim*(DeltaP_CSentry+DeltaP_CSmajor+DeltaP_CSexit))+DeltaP_CSbern;
    DeltaP61=(P_trim*(-DeltaP_Loss_LM));

    SectionPVector=[DeltaP12 DeltaP_HSentry DeltaP_HSmajor DeltaP_HSexit DeltaP_HSbern
DeltaP23 DeltaP34 DeltaP45 DeltaP_CSentry DeltaP_CSmajor DeltaP_CSexit DeltaP_CSbern
DeltaP56 DeltaP61];

    % P4=101000
    % P5=P4+DeltaP45
    % P6=P5+DeltaP56
    % P1=P6+DeltaP61
    % P2=P1+DeltaP12
    % P3=P2+DeltaP23
    % P4check=P3+DeltaP34


    %% Hot Side Fluids and Heat Transfer
    Nu_HS_FD=1.721*log(b_HS/a_HS)+3.1394; %laminar, Incropera
    Nu_HS=Nu_HS_FD+((.0668*(D_H_HS/L_Finned)*Re_HS*Pr_HS)/(1+.04*((D_H_HS/L_Finned)*Re_HS*
Pr_HS)^(2/3)));
    h_HS_int=((Nu_HS*k_HS)/D_H_HS);
    %Fin Efficiency
    m_HS=sqrt((2*h_HS_int)/(k_HSfin*t_HS));
    nf_HS=tanh(m_HS*Lc_HS)/(m_HS*Lc_HS);
    n0_HS=1-((((n_HS-1)*Af_HS)/At_HS)*(1-nf_HS));
    %Thermal Resistance
    R_HS_conv=1/(n0_HS*h_HS_int*At_HS);  %Internal Convection
    R_HS_cond=HS_Base/(k_HSfin*Area_Finned);
    SolderArea=(n_HS-1)*L_Finned*((.25+.25+.125)*.0254);
    R_HS_FinSolder=2*.14e-4/SolderArea;  %Incropera p.103
    R_HS_DevContact=.07e-4/DevicePlateArea;     %Incropera p.103
    R_HS=R_HS_conv+R_HS_cond+R_HS_DevContact+R_HS_FinSolder;
    T_HS=T_bar_HS+(Q_in*R_HS_conv);  %Plenum Temperature
    Tmax_base=T3+(Q_in*(R_HS));  %Maximum Device Mounting Temperature

    %HS Device Losses
    DeviceArea=(W_cell*L_cell)*(Cell_Rows*Cell_Columns);
    %k_epoxy=.177, l_epoxy=.015
    R_D_cond=.015/(.177*DeviceArea);
    h_Device=5+3; %conv +rad
    R_D_conv=1/(h_Device*DeviceArea);
    Q_DeviceLoss=(Tmax_base-T_amb)/(R_D_cond+R_D_conv);

    %HS Plenum loss (Q_loss as unknown and addtional eqn?)
    A_HS_ext=L_HS*(W_HS+2*b_HS);
    Ra_HS_ext=(g*beta_air*(T_bar_HS-T_amb)*L_HS^3)/(nu_air*alpha_air);
    Nu_HS_ext=.68+((.67*Ra_HS_ext^.25)/((1+(.492/Pr_air)^(9/16))^(4/9))); %Flat Plate
    h_HS_ext=(k_air*Nu_HS_ext)/L_HS;
    h_HS_rad=sigma*epsilon_HS*(((T_bar_HS)^2+(T_sur)^2)*(T_bar_HS+T_sur));
    Q_HS_loss=((h_HS_ext+h_HS_rad)*A_HS_ext*(T_bar_HS-T_amb))+Q_DeviceLoss
    Flux_loss=Q_HS_loss/A_HS_ext;

    %% Upper Manifold Fluids and Heat Transfer
    %Internal - Internal Flow with Entry Region, Incropera
    Nu_UM=4.36+((.0668*(D/L_x_Man)*Re_UM*Pr_UM)/(1+.04*((D/L_x_Man)*Re_UM*Pr_UM)^(2/3)));
    h_UM_int=(Nu_UM*k_UM)/D;
    R_UM_int=1/(h_UM_int*HTArea_Man);
    R_UM_cond=Man_Wall/(k_manifold*HTArea_Man);
    T_UM=T_bar_UM-(Q_UM*(R_UM_int+R_UM_cond));
    %External - Isothermal horizontal cylinder, Incropera
    Ra_D_UM=(g*beta_air*(T_UM-T_air)*(D+2*Man_Wall)^3)/(nu_air*alpha_air);
    Nus_bar_UM=(.6+((.387*(Ra_D_UM^(1/6)))/((1+(.559/Pr_air)^(9/16))^(8/27))))^2;
    h_UM_ext=(k_air*Nus_bar_UM)/(D+2*Man_Wall);
    %Radiation
    h_UM_rad=sigma*epsilon_CS*((T_UM^2+T_sur^2)*(T_UM+T_sur));
    %Thermal Resistance
```

```
    R_UM_ext=1/((h_UM_ext+h_UM_rad)*HTArea_ExtMan);%((1/(h_UM_ext*HTArea_ExtMan))+(1/(h_UM
_rad*HTArea_ExtMan)))^-1
    R_UM=R_UM_int+R_UM_cond+R_UM_ext;

    %% Cold Side Fluids and Heat Transfer
    Nu_CS_FD=8.235;%1.721*log(b_CS/a_CS)+3.1394 %laminar, Incropera(REPLACE WITH PARALLEL
PLATES STUFF11111)
    Nu_CS=Nu_CS_FD+((.0668*(D_H_CS/L_CS)*Re_CS*Pr_CS)/(1+.04*((D_H_CS/L_CS)*Re_CS*Pr_CS)^(
2/3)));
    h_CS_int=((Nu_CS*k_CS)/D_H_CS);
    %Thermal Resistance
    R_CS_int=1/(h_CS_int*HTArea_CS);
    R_CS_cond=CS_Wall/(k_CSwall*HTArea_CS);
    T_CS=T_bar_CS-(Q_CS*(R_CS_int+R_CS_cond));

    %% Lower Manifold Fluids and Heat Transfer
    Nu_LM=4.36+((.0668*(D/L_x_Man)*Re_LM*Pr_LM)/(1+.04*((D/L_x_Man)*Re_LM*Pr_LM)^(2/3)));
    h_LM_int=(Nu_LM*k_LM)/D;
    R_LM_int=1/(h_LM_int*HTArea_Man);
    R_LM_cond=Man_Wall/(k_manifold*HTArea_Man);
    T_LM=T_bar_LM-(Q_LM*(R_LM_int+R_LM_cond));
    %External
    Ra_D_LM=(g*beta_air*(T_LM-T_air)*(D+2*Man_Wall)^3)/(nu_air*alpha_air);
    Nus_bar_LM=(.6+((.387*(Ra_D_LM^(1/6)))/((1+(.559/Pr_air)^(9/16))^(8/27))))^2;
    h_LM_ext=(k_air*Nus_bar_LM)/(D+2*Man_Wall);
    %Radiation
    h_LM_rad=sigma*epsilon_CS*((T_LM^2+T_sur^2)*(T_LM+T_sur));
    %Thermal Resistance
    R_LM_ext=1/((h_LM_ext+h_LM_rad)*HTArea_ExtMan);%((1/(h_LM_ext*HTArea_ExtMan))+(1/(h_LM
_rad*HTArea_ExtMan)))^-1;
    R_LM=R_LM_int+R_LM_cond+R_LM_ext;        %add conduction later

    %% Ambient Fluids and Heat Transfer
    m_dot_air=Q_CS/(cp_air*(T5-T_amb));    %assume air warms to UM temp
    V_air=m_dot_air/(rho_air*FlowArea_amb);
    Re_air=rho_air*V_air*D_H_amb/mu_air;
    %Internal to fins: Rohsenow Isoflux Correlation
    Flux_amb=Q_CS/RejArea_amb;

    Ra_amb=(rho_air^2*g*beta_air*cp_air*Flux_amb*(a_amb^5))/(mu_air*L_CS*k_air^2);
    Nu_amb_channel=((48/Ra_amb)+(2.51/(Ra_amb^.4)))^-.5;  %Rohsenow Isoflux eqn.
    Nu_amb=Nu_amb_channel+((.0668*(D_H_amb/L_CS)*Re_air*Pr_air)/(1+.04*((D_H_amb/L_CS)*Re_
air*Pr_air)^(2/3)));
    h_amb=(k_air*Nu_amb/a_amb); %Internal to plate gaps
    %Vert Plate (Exposed end plates)
    Ra_plate=(g*beta_air*(T_CS-T_amb)*L_CS^3)/(nu_air*alpha_air);
    Nu_plate=.68+((.67*Ra_plate^.25)/((1+(.492/Pr_air)^(9/16))^(4/9)));
    h_plate=(k_air*Nu_plate)/L_CS;
    Area_plate=2*N_HX*((a_CS*L_CS))+2*(W_CS*L_CS); %tips + sides of HX
    %Radiation
    h_amb_rad=sigma*epsilon_CS*(((T_CS)^2+(T_sur)^2)*(T_CS+T_sur));
    %Thermal Resistances
    R_amb_conv=1/(h_amb*RejArea_amb);
    R_amb_plate=1/(h_plate*Area_plate);
    R_amb_rad=1/(h_amb_rad*RadArea_amb);
    R_CS_amb=((1/R_amb_conv) + (1/R_amb_rad)+(1/R_amb_plate))^-1;
    R_CS=R_CS_int+R_CS_cond+R_CS_amb;

    T_bar_CS-273;
    T_CS-273;
    RejectionA=(RejArea_amb+2*HTArea_Man);
    U_Rejection=(Q_in-Q_HS_loss)/((RejArea_amb+2*HTArea_Man)*(T_CS-T_amb));
    %% Mixed Convection Check
    GR_HS=(g*beta_HS*abs(T_HS-T_bar_HS)*a_HS^3)/(nu_HS^2);
    GR_UM=(g*beta_UM*abs(T_UM-T_bar_UM)*D^3)/(nu_UM^2);
    GR_CS=(g*beta_CS*abs(T_CS-T_bar_CS)*a_CS^3)/(nu_CS^2);
    GR_LM=(g*beta_LM*abs(T_LM-T_bar_LM)*D^3)/(nu_LM^2);
    GR_Amb=(g*beta_air*abs(T_CS-T_amb)*a_amb^3)/(nu_air^2);

    %% Compile important metrics
```

```
    H=[h_HS_int h_HS_ext h_HS_rad h_UM_int h_UM_ext h_UM_rad h_CS_int h_amb h_amb_rad
h_LM_int h_LM_ext h_LM_rad];
    R=[R_HS R_HS_conv R_HS_cond R_CS R_CS_int R_CS_amb R_UM R_LM];
    P=[DeltaP12 DeltaP23 DeltaP34 DeltaP45 DeltaP56 DeltaP61];
    Q=[Q_in Q_HS_loss Q_UM Q_CS Q_LM];
    FLUX=[1];%[Flux_HS Flux_loss Flux_UM Flux_CS Flux_amb Flux_LM];
    N_0=[n0_HS];
    RE=[Re_HS Re_UM Re_CS Re_LM Re_air];
    ENTRY=[1];%[Entry_HS Entry_UM Entry_CS Entry_LM Entry_air];
    AREA=[HTArea_HS A_HS_ext HTArea_CS HTArea_Man RejArea_amb RadArea_amb];
    V=[V_HS V_UM V_CS V_LM V_air];
    NU=[Nu_HS Nu_HS_ext Nu_UM Nu_CS Nu_LM Nu_amb];
    PR=[Pr_HS Pr_UM Pr_CS Pr_LM];
    SumPressure=DeltaP12+DeltaP23+DeltaP34+DeltaP45+DeltaP56+DeltaP61;
    GR=[GR_HS GR_UM GR_CS GR_LM GR_Amb];
    MIXED=[GR_HS/(Re_HS^2) GR_UM/(Re_UM^2) GR_CS/(Re_CS^2) GR_LM/(Re_LM^2)
GR_Amb/(Re_air^2)];
    % SumPressure=DeltaP_HS_buoy+ DeltaP_CS_buoy + P_trim*(DeltaP_HS_loss + DeltaP_UM_loss
+ DeltaP_CS_loss + DeltaP_LM_loss);
    % SumQ=Q_HS-(Q_HS_loss +Q_UM +Q_CS +Q_LM);
    SumQ=Q_in-(Q_HS_loss+Q_UM +Q_CS +Q_LM);

    %% System of Equations

    HS_therm = m_dot*cp_HS*(T3-T2)-(Q_in-Q_HS_loss);
    UM_therm = m_dot*cp_UM*(T4-T5)-Q_UM;
    CS_therm = m_dot*cp_CS*(T5-T6)-Q_CS;
    LM_therm = m_dot*cp_LM*(T6-T1)-Q_LM;
    P_balance =  DeltaP12+DeltaP23+DeltaP34+DeltaP45+DeltaP56+DeltaP61;%DeltaP_HS_buoy +
DeltaP_CS_buoy + P_trim*(DeltaP_HS_loss + DeltaP_UM_loss +  DeltaP_CS_loss +
DeltaP_LM_loss);
    UM_heat = Q_UM-(T_bar_UM-T_amb)/R_UM;
    CS_heat = Q_CS-(T_bar_CS-T_amb)/R_CS;
    LM_heat = Q_LM-(T_bar_LM-T_amb)/R_LM;

    Remainders=[HS_therm UM_therm CS_therm LM_therm P_balance UM_heat CS_heat LM_heat];

    % %% Old Equation Sets
    % EntryFactor=L_Man/(D*Re_UM)  %% Morrison Solar Paper, circ pipes
    % LossMult=1+(.038/(EntryFactor^.96))
    % ManLoss=LossMult*(((64/Re_UM)*L_Man*V_UM^2)/(2*g*D))
```

- Midel Fluid Properties

```
    % Temperature in Kelvin
    function [properties]=Midel(T)


    nu=9.628e-2*exp(-2.599e-2*T);%[m^2/s]
    k=-7.204e-7*T^2+3.71e-4*T+9.751e-2;%[W/m-K]
    rho=-.7337*T+1185.3; %[kg/m^3]
    cp=2.17*T+1249.6; %[J/kg-K]
    beta=6.584e-7*T+5.607e-4;%[1/K]

    alpha=k/(rho*cp);%[m^2/s]
    mu=rho*nu;%[N-s/m]
    Pr=nu/alpha;%[dim]

    properties=[beta nu k rho cp alpha mu Pr];
```

- Example Parameters from Updated 2.5kW model.

	Unit	HS	UM	CS	LM	Amb Air
h_in	W/m^2K	96.28753	25.53777	94.5353	25.63397	
h_out	W/m^2K	3.61067	4.943829	5.162924	4.121224	
h_rad	W/m^2K	0.242083	7.104473	7.181436	6.690962	
R_therm	C/W	0.004208	0.23042	0.014292	0.247088	
DeltaP	Pa	-7378.11	-0.37386	7379.082	-0.6029	
Q	W	-2425.64	179.3947	2161.794	84.45592	
Flow Area	m^2	0.0244	0.0091	0.0468	0.0091	0.1355
V	m/s	0.002462	0.006651	0.001286	0.006545	0.336499
Re	-	2.405805	52.58116	1.270186	30.39548	719.2631
Internal HTArea	m^2	3.835037	0.326451	11.60934	0.479143	11.29597
Nu	-	8.415519	14.0484	8.436522	13.84603	3.490372
Gr		133.3302	545255.6	24.41964	86755.86	20157.03
Mixed		23.03603	197.215	15.13576	93.90329	0.038963